

AD-A141 090

OPTICAL ADAPTIVE FILTER FREQUENCY DOMAIN IMPLEMENTATION

1/3

(U) AIR FORCE INST OF TECH WRIGHT-PATTERSON AFB OH

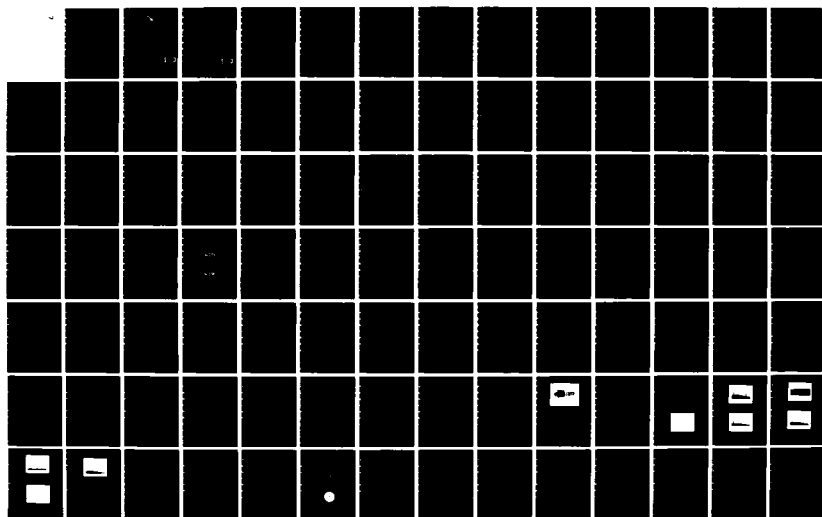
SCHOOL OF ENGINEERING J L NEWMAN DEC 83

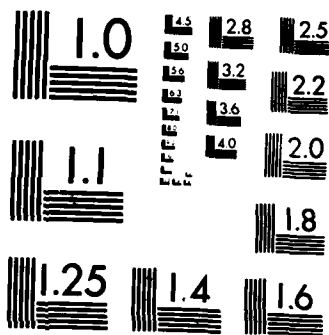
UNCLASSIFIED

AFIT/GE/EE/83D-51

F/G 20/6

NL





MICROCOPY RESOLUTION TEST CHART
NATIONAL BUREAU OF STANDARDS-1963-A

AD-A141 090

①



OPTICAL ADAPTIVE FILTER:
 FREQUENCY DOMAIN IMPLEMENTATION

THESIS

AFIT/GE/EE/83D-51

Jeffrey L. Newman
 1st Lt USAF

DTIC FILE COPY

DTIC
 ELECTE
 MAY 15 1984

S B

DEPARTMENT OF THE AIR FORCE
 AIR UNIVERSITY

AIR FORCE INSTITUTE OF TECHNOLOGY

Wright-Patterson Air Force Base, Ohio

DISTRIBUTION STATEMENT A
 Approved for public release
 Distribution Unlimited

84 05 14 118

AFIT/GE/EE/83D-51

OPTICAL ADAPTIVE FILTER:
FREQUENCY DOMAIN IMPLEMENTATION

THESIS

AFIT/GE/EE/83D-51

Jeffrey L. Newman
1st Lt USAF

S DTIC
ELECTE **D**
MAY 15 1984
B

Approved for public release; distribution unlimited

Preface

With the increasing demand for broadband adaptive linear prediction in real time, digital signal processing techniques are no longer adequate. Therefore, optical signal processing techniques are required. Optical implementations provide broadband parallel processing in the time that it takes an optical beam to travel through the system. In this thesis, two interferometric optical architectures were built to test the feasibility of implementing an optical adaptive filter in the frequency domain. This topic was selected because it has applications in many areas of current interest and it explores a new frontier in an emerging technology.

First and foremost, I give thanks to my Lord and Saviour, Jesus Christ (the true Light), for His guidance throughout this thesis. Next, I thank my wife Connie for her assistance and moral support.

In addition, I thank Dr. Anonymous for his theoretical and technical assistance as well as his encouragement throughout the entire thesis. Moreover, I thank Mrs. Anonymous for her generous hospitality.

Furthermore, I thank Dr. Vic Syed for his theoretical and technical assistance as my advisor. Also, I thank Dr. Matt Kabrisky and Maj. Ken Castor for their expert advice.

Finally, without the administrative support of Miriam and Allen Burkett, this thesis would be merely ideas scribbled on paper. Thanks Miriam and Allen for your rapid response and a very admirable final product.

Table of Contents

	<u>Page</u>
Preface-----	ii
List of Figures-----	vi
List of Photographs-----	ix
List of Tables-----	xi
List of Symbols-----	xiii
Abstract-----	xvi
I. Introduction-----	1
Thesis Organization-----	1
II. Overview-----	4
Statement of the Problem-----	4
Background-----	5
State-of-the-Art-----	6
Proposal-----	7
III. Theoretical Development-----	8
Introduction-----	8
Fundamentals of Adaptive Linear Prediction-----	8
Adaptive Transversal Filter-----	9
Calculation of Optimum Adaptive Weights with CCLs-----	10
Fundamentals of Optical Signal Processing-----	17
Fourier Optics-----	18
Fourier Transforming Principles-----	18
Imaging Principles-----	23
Acousto-Optics-----	17
OAF-----	35
OAFFI-----	40
Summary-----	45

Table of Contents (Cont'd)

	<u>Page</u>
IV. Optical Architectures Leading To OAFFI-----	47
Introduction-----	47
Optical Spectrum Analyzer-----	47
Theory-----	47
Observations-----	50
Optical Excisor Version I-----	51
Theory-----	51
Observations-----	55
Optical Excisor Version II-----	57
Theory-----	57
Observations-----	60
Liquid Crystal Light Valve Test-----	66
Theory-----	66
Observations-----	69
OAFFI(MZI)-----	72
Theory-----	72
Observations-----	82
Conclusions-----	86
OAFFI(CPI)-----	88
Theory-----	88
Observations-----	98
Conclusions-----	108
Summary-----	109
V. Determining OAFFI(CPI) Characteristics-----	111
Introduction-----	111
Error Signal Versus Frequency-----	114
Error Signal Versus LCLV Angle-----	114
Time Delay Versus Frequency-----	124
Error Analysis-----	133
Observations-----	136
Time Delay Versus LCLV Angle-----	137
Time Delay Versus Transducer Distance-----	143
Minimum Time Delay Observed-----	148
Radio Frequency Interference-----	149
Data Analysis-----	156
Minimum Time Delay-----	156
Time Aperture-----	158
Bandwidth Range-----	158
Time-Bandwidth Product-----	158
Frequency Resolution-----	159
Cancellation Ratio-----	159
Signal-to-Noise Ratio Effect-----	160

Table of Contents (Cont'd)

	<u>Page</u>
VI. Summary, Conclusions and Recommendations-----	162
Summary-----	162
Conclusions-----	163
Recommendations-----	165
Bibliography-----	168
Appendix A: IntraAction Bragg Cell-----	171
Appendix B: Hughes Liquid Crystal Light Valve-----	176
Appendix C: OAFFI(CPIA) Analysis-----	179
Vita-----	182

Accession For	
NTIS GR&I	<input checked="" type="checkbox"/>
DTIC TAB	<input type="checkbox"/>
Unannounced	<input type="checkbox"/>
Justification	<input type="checkbox"/>
By	
Distribution/	
Avail. and/or Codes	
Dist. Statement	
Dist	Special
A-1	



List of Figures

<u>Figure</u>		<u>Page</u>
1	Adaptive Linear Predictor Implemented with a Weighted Tapped-Delay Line-----	4
2	Adaptive Linear Predictor Implemented with Correlation Cancellation Loops-----	5
3	Adaptive Transversal Filter Using an Adaptive Linear Combiner and a Tapped-Delay Line-----	9
4	An Analog LMS Adaptive Filter-----	16
5	The Nth Correlation Cancellation Loop-----	17
6	Fourier Transforming Configurations-----	19
7	Single Lens with Object Placed in Front of the Lens-----	20
8	Optical Fourier Transform System-----	22
9	Geometry for Image Formation-----	23
10	Two-Lens System In One-Dimension-----	26
11	Bragg Regime Light Diffraction-----	28
12	Bragg Cell as an AO Delay Line-----	29
13	Ratio of Diffracted Intensity to Incident Intensity Vs. Input Electrical Amplitude-----	31
14	Bragg Diffraction-----	33
15	Deflection of Light Beams by Increasing Sound Frequency-----	33
16	Demodulation of the Light Spectrum-----	34
17	Modulation of Input Light Intensity by an Electrooptic Modulator and a Bragg Cell-----	36
18	Optical Adaptive Filter Block Diagram-----	37
19	Schematic of the Optical Portion of the Optical Adaptive Filter-----	38

List of Figures (Cont'd)

<u>Figure</u>		<u>Page</u>
20	Optical Adaptive Filter: Frequency Domain Implementation-----	42
21	Optical Spectrum Analyzer-----	48
22	Optical Spectrum Analyzer Output-----	50
23	Optical Excisor Version I-----	52
24	Optical Excisor Version II-----	58
25	LCLV Photo Response Characteristics-----	67
26	Liquid Crystal Light Valve Test-----	68
27	Maximized Intensity of $ X(\omega) ^2$ by Polarizer POL-----	70
28	Maximized Intensity of LCLV "Ambient State" by Polarizer POL-----	70
29	OAFFI Implemented with Mach-Zehnder Interferometer-----	73
30	Comparison of Microscope Objectives (40X vs. 10X)-----	77
31	Output Spectrum of OAFFI(MZI)-----	81
32	OAFFI Implemented with Common Path Interferometer-----	89
33	Electrical Circuit for OAFFI(CPI) Not Shown in Fig. 32-----	95
34	Simplified Feedback Model for Fig. 33-----	96
35	Graph of Error Signal Versus Input Frequency for Two Separate Trials-----	117
36	Graph of Error Signal Versus LCLV Angle for Three Frequencies-----	123
37	Phase Difference Versus Frequency for C-L with 70 MHZ Filter-----	127
38	Computer Program in Basic Language to Compute Average and Standard Deviation of N Numbers-----	132
39	Graph of τ_{ave} Versus LCLV Angle, O-L with 70 MHZ Filter-----	142

List of Figures (Cont'd)

<u>Figure</u>		<u>Page</u>
40	Graph of τ_{ave} Versus Transducer Distance d , O-L with 70 MHZ Filter-----	147
41	RFI Versus Frequency, O-L with 70 MHZ Filter-----	153
42	VSWR Nomograph-----	155
43	Conceptual Architecture for OAFFI(CPIA)-----	167

List of Photographs

<u>Photo</u>		<u>Page</u>
1	Photomultiplier Tube (931A) Used as a Photo Detector in Optical Excisor Version II and Succeeding Architectures-----	60
2	70 MHZ Optical Signal w/o Filter-----	62
3	Spectrum of 70 MHZ Optical Signal (Photo 2)-----	63
4	Spectrum of 70 MHZ RFI w/o Filter-----	63
5	70 MHZ Optical Signal w/o Filter. Extra Beam Splitter (BS3) Added to Reference Path. All Cylindrical Lenses Removed-----	64
6	Spectrum of 70 MHZ Optical Signal (Photo 5). Extra Beam Splitter (BS3) Added to Reference Path. All Cylindrical Lenses Removed-----	64
7	Spectrum of 70 MHZ RFI w/o Filter. Extra Beam Splitter (BS3) Added to Reference Path. All Cylindrical Lenses Removed-----	65
8	70 MHZ Optical Signal w/o Filter. Extra Beam Splitter BS3 and Cylindrical Lens CL3 Added to Reference Path-----	65
9	Spectrum of 70 MHZ Signal (Photo 8). Extra Beam Splitter BS3 and Cylindrical Lens CL3 Added to Reference Path-----	66
10	70 MHZ Optical Signal w/o Filter-----	84
11	Spectrum of PMT Output for Photo 10-----	85
12	Spectrum of PMT Output w/o Filter and with Optical Signal Blocked from BC2 Path of MZI-----	85
13	Spectrum of PMT Output w/o Filter and with Optical Signal Blocked from LCLV-----	86
14	Avalanche Photo-Diode Used in OAFFI(CPI)-----	94
15	Optical/Electrical Hardware Used to Implement OAFFI(CPI)-----	98
16	Better View of RM3 Region for Photo 15-----	99

List of Photographs (Cont'd)

<u>Photo</u>		<u>Page</u>
17	Supporting Equipment for OAFFI(CPI)-----	100
18	Supporting Equipment for OAFFI(CPI), Continued from Photo 17-----	101
19	70 MHZ Optical Signal with Filter-----	102
20	Spectrum of APD Output for Photo 19-----	103
21	Spectrum of APD Output with Filter and with Optical Signal Blocked from APD-----	104
22	Spectrum of APD Output with Filter and New Amps-----	105
23	Spectrum of $e(t)$ with Filter for Reference Level: $e(t) = x(t) - 0$ -----	106
24	70 MHZ Signal $x(t)$ and $\hat{x}(t)$ for $e(t) = -5\text{dB}$ as Seen in Photo 25-----	106
25	Spectrum of $e(t)$ with Filter and Input of Photo 24 for $e(t) = x(t) - \hat{x}(t) = -5\text{dB}$ from Referenc. Level of Photo 23-----	107
26	Spectrum of $e(t)$ with Filter and Positive Feedback Causing Oscillations (Unstable Response)-----	108
27	Two 70 MHZ Optical Signals to be Added in Phase-----	112
28	Result of Adding the Two Signals in Photo 27-----	112
29	Two 70 MHZ Optical Signals to be Added 180 Degrees Out of Phase-----	113
30	Result of Adding the Two Signals in Photo 29-----	113
31	Phase Difference Calculation Between $x(t)$ and $\hat{x}(t)$ to Determine $\Delta\tau$ -----	125
32	70 MHZ Signals $\hat{x}(t)$ and $x(t)$ for C-L w/o 70 MHZ Filter-----	128
33	Spectrum of $e(t)$ w/o Filter and Positive Feedback Causing Oscillations (Unstable Response)-----	129

List of Tables

<u>Table</u>		<u>Page</u>
I	Abbreviations Used in Fig. 29-----	75
II	Distances Between Devices in Fig. 29-----	76
III	Abbreviations Used in Fig. 32-----	90
IV	Distances Between Devices in Fig. 32-----	91
V	Error Signal Versus Input Frequency for $e(t) = -5\text{dB}$ at 70 MHZ-----	115
VI	Error Signal Versus Input Frequency for $e(t) = -5\text{dB}$ at 76 MHZ-----	116
VII	Error Signal Versus LCLV Angle for Input Frequency of 65 MHZ-----	119
VIII	Error Signal Versus LCLV Angle for Input Frequency of 70 MHZ-----	120
IX	Error Signal Versus LCLV Angle for Input Frequency of 75 MHZ-----	122
X	Phase Difference Versus Frequency for C-L with 70 MHZ Filter-----	126
XI	Time Delay Versus Frequency for O-L with 70 MHZ Filter-----	131
XII	Time Delay Versus Frequency for O-L w/o 70 MHZ Filter-----	134
XIII	Time Delay Versus LCLV Angle for O-L with 70 MHZ Filter-----	138
XIV	Time Delay Versus Transducer Distance d for O-L with 70 MHZ Filter-----	144
XV	Minimum Value Test for τ_{ave} with O-L and 70 MHZ Filter-----	150
XVI	RFI Measured as a Function of Frequency, O-L with 70 MHZ Filter-----	152
XVII	SNRs Measured for Normal Bragg Cell 50 Ohm Load-----	157

List of Tables (Cont'd)

<u>Table</u>		<u>Page</u>
XVIII	SNRs Measured for Additional 50 Ohms Added in Series to Each Bragg Cell-----	157
XIX	OAFFI(CPI) Characteristics-----	161

List of Symbols

ALP	Adaptive Linear Prediction/Predictor
AO	Acousto-Optics
APD	Avalanche Photo-Diode
Arg-ion	Argon-ion
AVSD	Average and Standard Deviation
BC	Bragg Cell
BP	Bandpass
BS	Beam Splitter
BW	Bandwidth
CB	Cardboard (white index card)
CCL	Correlation Cancellation Loop
CF	Center Frequency
CL	Cylindrical Lens
C-L	Closed-Loop
CPI	Common Path Interferometer
dB	Decibels
Div.	Division(s)
FIR	Finite Impulse Response
FT	Fourier Transform
GHZ	Gigahertz (1×10^9)
He-Ne	Helium-Neon
Hor.	Horizontal
HWP	Half-Wave Plate ($\lambda/2$)
KHZ	Kilohertz (1×10^3)

List of Symbols (Cont'd)

LCLV	Liquid Crystal Light Valve
LHS	Left Hand Side
LMS	Least Mean-Square
MHZ	Megahertz (1×10^6)
MMSE	Minimum Mean Square Error
MO	Microscope Objective
msecs	milliseconds (1×10^{-3})
mv	millivolt (1×10^{-3})
MZI	Mach-Zehnder Interferometer
nsecs	nanoseconds (1×10^{-9})
OAF	Optical Adaptive Filter (time domain)
OAFFI	Optical Adaptive Filter: Frequency Domain Implementation
OSP	Optical Signal Processing
O-L	Open-Loop
PA	Power Amplifier
PAG	Phase Adjusting Glass
PD	Photo-Detector
PDA	Photo-Diode Array
PMT	Photomultiplier Tube
P-P	Peak-to-Peak
RF	Radio Frequency
RFI	Radio Frequency Interference
RHS	Right Hand Side
RM	Fully Reflective Mirror
rms	root mean square

List of Symbols (Cont'd)

SD	Standard Deviation
SL	Spherical Lens
SNR	Signal-to-Noise Ratio
SQRT	Square Root
T	period of signal/transpose of a vector/sampling interval
TS	Two-Way Splitter
VA	Variable Attenuator
VAC	Volts Alternating Current
Vert.	Vertical
VSWR	Voltage Standing Wave Ratio
w	with
w/o	without
μ	micron (1×10^{-6} meters)
μ secs	microseconds (1×10^{-6})

Abstract

This report presents the results of a feasibility test on an optical adaptive filter, implemented in the frequency domain. The OAFFI is the follow-on to the optical adaptive filter (OAF), which was implemented in the time domain. The theory of OAFFI is based on adaptive linear prediction using correlation cancellation loops and optical signal processing (OSP) using Fourier optics (lenses) and acousto-optics (Bragg cells).

A few optical architectures, which form the fundamental building blocks of OAFFI, were built and examined prior to the OAFFI architectures. These fundamental architectures included an Optical Spectrum Analyzer, Optical Excisor (two versions) and a Liquid Crystal Light Valve. The Optical Excisor used heterodyning principles which in an OSP sense usually involves an interferometric architecture.

The OAFFI was implemented in two-versions: Mach-Zehnder interferometer (MZI) and common path interferometer (CPI). OAFFI(MZI) exhibited phase stability problems in the optical output. To overcome these phase stability problems, the common path interferometer version of OAFFI was built. OAFFI(CPI) overcame the phase stability problems of OAFFI(MZI). However, stability problems resulting from positive feedback at various frequencies were observed in OAFFI(CPI). Nevertheless, OAFFI(CPI) also demonstrated some positive results that should stimulate further investigations. ←

I. Introduction

A broadband adaptive linear predictor (ALP) continually forms an estimate of the instantaneous value of an input signal. This is accomplished by using a weighted tapped-delay line, in a closed-loop configuration, whose weights are controlled by an error signal. The error signal is the difference between the input signal value and the estimated value. When an ALP is implemented by using optical signal processing (OSP) techniques, not only are larger bandwidths possible, but also parallel processing of delayed versions of the input signal is accomplished in near real-time.

This thesis presents the results of an investigation which tested the feasibility of an optical adaptive filter implemented in the frequency domain. The optical adaptive filter: frequency domain implementation (OAFFI) is the follow-on to the OAF (Optical Adaptive Filter), which was implemented in the time domain (Ref. 22). Because the OAF exhibited a marginal performance, resulting from a lack of proper equipment and inherent architectural problems, the OAFFI was suggested as a frequency domain equivalent, which hopefully would surpass the performance of the OAF.

Thesis Organization

This thesis begins, in Chapter II, with a statement-of-the-problem, which is then followed by pertinent background information on OAFFI. Next, a discussion on state-of-the-art optical adaptive filters will be given prior to the thesis proposal.

In Chapter III, the fundamentals of adaptive linear prediction will be discussed, followed by a derivation of the correlation cancellation loop (CCL) method for calculating adaptive tap-weights. Then, a discussion on the fundamentals of OSP will include Fourier optics and acousto-optics (AO). Furthermore, the applications of ALP and OSP are addressed in the theoretical development of OAF and OAFFI, which concludes the chapter.

Chapter IV describes a few optical architectures that form the fundamental building blocks of OAFFI. After the fundamental architectures are discussed, the first version of OAFFI, which implements a Mach-Zehnder interferometer (MZI), is introduced. As a result of phase stability problems exhibited by the optical output of OAFFI(MZI), a second version, which implements a common path interferometer (CPI), was investigated. The OAFFI(CPI) overcame the phase stability problems encountered in OAFFI(MZI). The relevant properties and characteristics of the OAFFI(CPI) are described in Chapter V.

Finally, in Chapter VI, a summary of the thesis is presented, which is followed by the conclusions on the OAFFI(CPI) investigation. Recommendations for future research on the OAFFI, which include the existing architecture as well as an alternative architecture, conclude the chapter.

The main body of the thesis is followed by Appendices A, B and C. Appendix A describes the characteristics of the Bragg cell that was used throughout the thesis. In Appendix B, the operation of the LCLV is described in detail. Finally, Appendix C presents a mathematical

analysis of a proposed alternative OAFFI architecture mentioned in the
"Recommendations" section of Chapter VI.

II. Overview

Statement of the Problem

A broadband adaptive linear predictor (ALP) is a proposed solution to various wideband signal processing requirements; e.g. broadband digital filters, adaptive beam steering antennas, sidelobe rejection antennas, echo equalization and causal broadband signal prediction. The ALP continually estimates the instantaneous value of an input signal by using a weighted tapped-delay line as illustrated in Fig. 1. When using the minimum mean-square error (MMSE) criterion to select the weights w_0 , w_1 ,

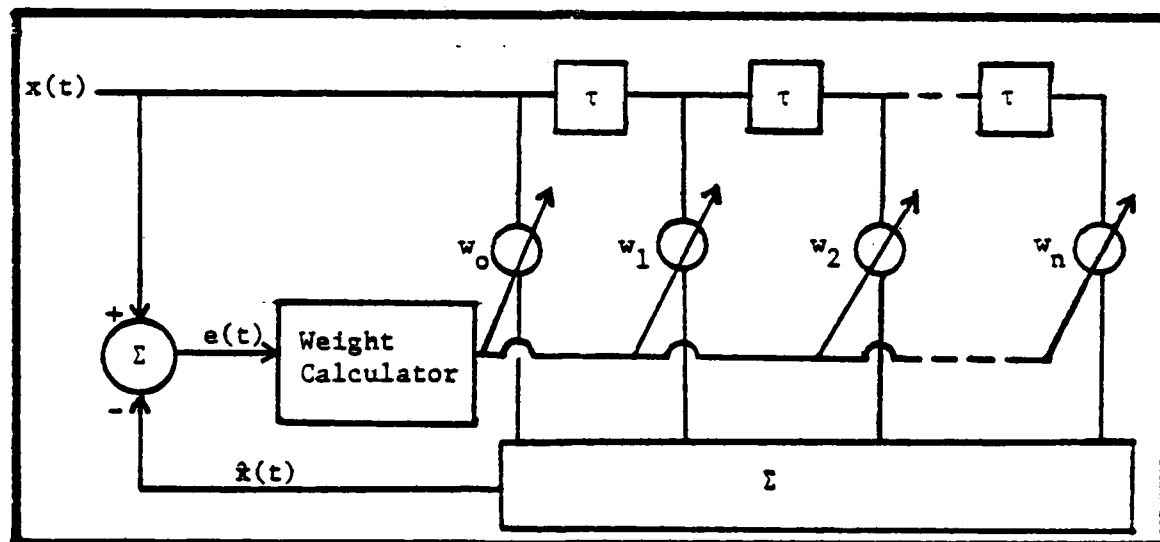


Fig. 1. Adaptive Linear Predictor Implemented with a Weighted Tapped-Delay Line

... w_n , the correlation cancellation loop (CCL) of Fig. 2 results. Although CCLs are implemented routinely (with digital and analog hardware) to solve problems in speech processing, channel equalizations, adaptive antenna arrays, etc.; their basic limitation is a maximum

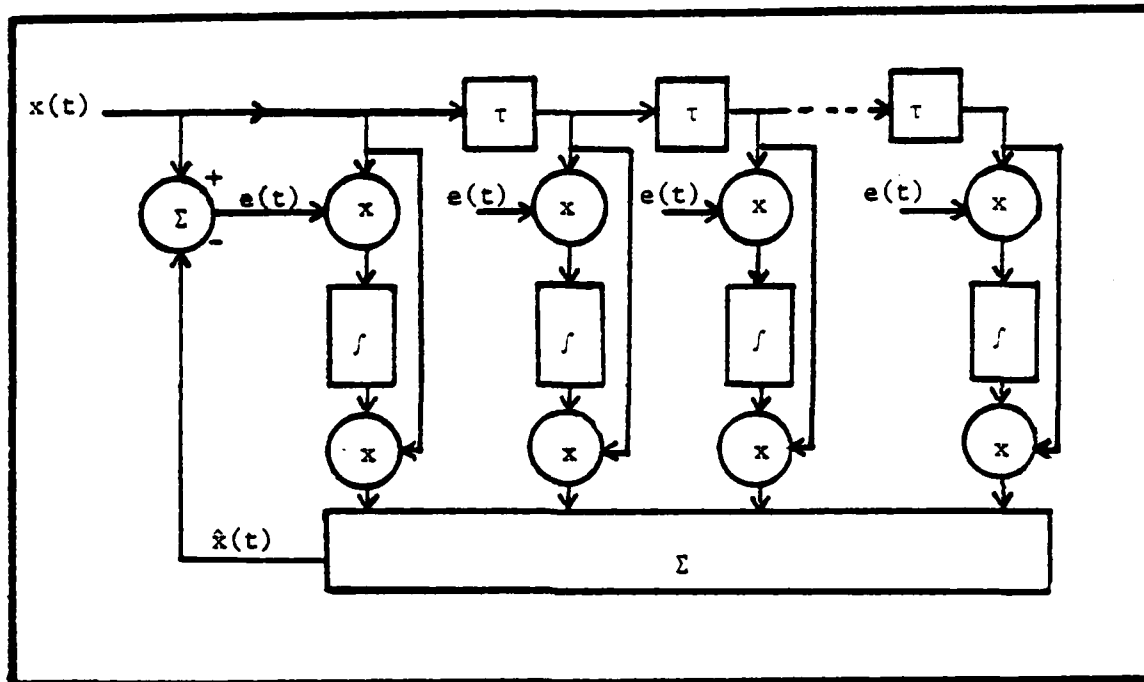


Fig. 2. Adaptive Linear Predictor Implemented with Correlation Cancellation Loops

bandwidth (BW) of 5-7 MHz. The implementation of CCLs with optical hardware appears promising (Ref. 22) and is innovative.

Previous work in this area has concentrated on the implementation of a CCL using optical hardware, with the associated processing in the time domain. In this thesis, the emphasis will be on determining the feasibility of implementing a broadband CCL in the optical frequency domain via optical signal processing (OSP) techniques. In what follows, the terms ALP and CCL will be used interchangeably.

Background

To implement this broadband ALP, the "Optical Adaptive Filter: Frequency Domain Implementation (OAFFI)" structure was selected (Ref. 22) for the following reasons:

1. An alternative implementation, the Optical Adaptive Filter: Time Domain Implementation (OAF) is limited to about 100 MHZ BW.
2. OAFFI may yield the full potential BW (1 GHZ) available in state-of-the-art Bragg cells (acousto-optic modulators).
3. Optical implementations provide broadband parallel processing in real-time.

Note that the OAF used a Bragg cell, which was constrained to operate in the "linear in intensity range" of the modulation transfer curve (Fig. 13) as a result of the time domain implementation (Ref. 22:144). This constraint limited the useful BW of the Bragg cell to 100 MHZ.

But OAFFI permits the Bragg cell to operate in the "linear in amplitude range" of the curve (Fig. 13) as a result of the frequency domain implementation (Ref. 22:144). This requirement, which will be discussed later, makes possible the use of the maximum BW capability (≥ 1 GHZ) of Bragg cells. In addition to greater BW, improved signal-to-noise ratio (SNR) should be achieved by integration of the input power spectrum.

State-of-the-Art

Currently, there are three suggested architectures to develop an optical broadband ALP: 1.) OAF, 2.) OAFFI and 3.) Adaptive Optical Processor (AOP). Until this current report, OAF was the only one of the three architectures which had been tested for feasibility. However, many problems arose with equipment characteristics and the optical set-up. Also, the Liquid Crystal Light Valve (LCLV) works best with a green light source; however, a red light source (Krypton-ion laser) was used (with increased integration time achieved by driving the LCLV at a lower frequency rather than the recommended frequency). The second

architecture (subject of this report), OAFFI, uses a frequency domain implementation as opposed to the time domain implementation used in OAF. The third architecture, AOP, also uses a frequency domain implementation (Ref. 26).

Moreover, the AOP employs three Bragg cells and numerous anamorphic transforming and imaging lenses in order to avoid the LCLV, which demonstrated a limited dynamic range in the OAF. This method also requires the Bragg cells to be operated in the "linear in amplitude range" of the curve (Fig. 13). One disadvantage of the AOP appears to be the numerous optical components required. Thus, AOP would entail a more detailed optical setup than the OAFFI. For these reasons, the OAFFI will be the primary objective of this thesis.

Proposal

This thesis will test the feasibility of implementing an optical adaptive linear predictor in the frequency domain. In the pursuit of OAFFI, theory and experimentation will be combined to achieve the following goal: tracking by the filter output, a 70 MHz sine wave input; i.e., cancellation of a 70 MHz sine wave by the CCL. The attainment of this goal will help to determine many aspects of system performance (i.e. minimum time delay, time aperture, BW range, time-bandwidth product, frequency resolution, cancellation ratio and SNR effects). Although, this goal may appear to be trivial, it will require meticulous optical alignment to achieve. Once this goal is attained, many of the system characteristics and limitations will be identified.

III. Theoretical Development

Introduction

OAFFI is the frequency domain equivalent of the OAF. The theory of the OAF is based on adaptive linear prediction (ALP) with correlation cancellation loops (CCLs). By using CCLs, an optimum method for obtaining the minimum mean-square error (MMSE) estimation of an input signal is achieved. CCLs can be constructed by using a weighted tapped-delay line in a closed-loop feedback arrangement. The MMSE estimate, $\hat{x}(t)$, continuously adapts to approach the actual value of the input signal, $x(t)$.

In this chapter of the thesis, a tutorial on the fundamentals of ALP (with CCLs) and OSP will be discussed. Following the discussion on ALP and OSP, OAF theory will be reviewed; and this will then be followed by the development of OAFFI theory.

Fundamentals of Adaptive Linear Prediction

Adaptive filtering techniques are used in spectrum analysis (band rejection), system modeling (closed-loop feedback) and speech processing (linear predictive coding or LPC). The origins of adaptive linear prediction lie in the theory of FIR digital filters, window techniques and weighted tapped-delay lines, which are discussed in literature (Refs. 5, 10, 19). The basic structure of an adaptive linear predictor (ALP) is that of a tapped-delay line with variable weights. A tapped-delay line is sometimes called a transversal filter. Therefore, a review of an adaptive transversal filter will introduce this section on ALP.

Adaptive Transversal Filter (Ref. 24)

An Nth order adaptive transversal filter is shown in Fig. 3. In

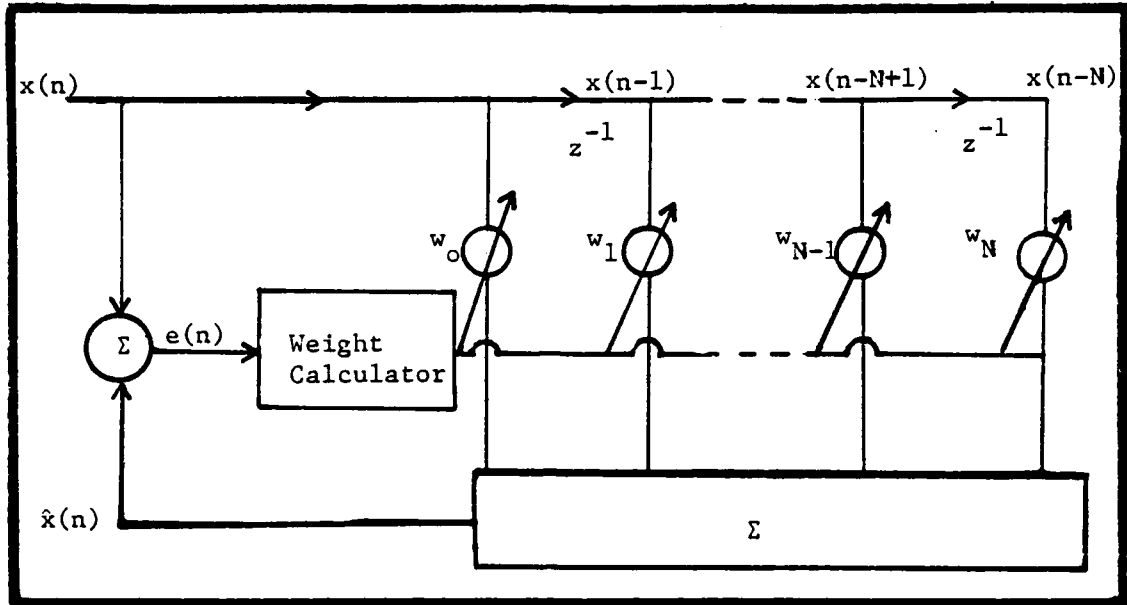


Fig. 3. Adaptive Transversal Filter Using an Adaptive Linear Combiner and a Tapped-Delay Line (Ref. 27:616)

the figure, z^{-1} represents the z-domain transfer function of a unit delay element. The output $\hat{x}(n)$ of the filter is given by Eq. (1).

$$\hat{x}(n) = \sum_{k=0}^N w_k x(n-k) \quad (1)$$

In the z-domain, the output $\hat{x}(n)$ becomes $\hat{X}(z)$ and can be related to $X(z)$, the z-transform of the input, by Eq. (2).

$$\begin{aligned} \hat{X}(z) &= X(z) w_0 + z^{-1} X(z) w_1 + \dots + z^{-N} X(z) w_N \quad (2) \\ &= X(z) [w_0 + z^{-1} w_1 + \dots + z^{-N} w_N] \end{aligned}$$

Now, Eq. (2) can be used to define the transfer function given by Eq.

(3)

$$H(z) \triangleq \hat{X}(z)/X(z) \quad (3)$$

From Equations (2) and (3), the transfer function relationship of Eq. (4) results.

$$\begin{aligned} H(z) &= \frac{w_0 + w_1 z^{-1} + \dots + w_N z^{-N}}{1} \\ &= \frac{w_0 z^N + w_1 z^{N-1} + \dots + w_N}{z^N} \end{aligned} \quad (4)$$

The weights w_i , $i = 0, 1, \dots, N$, dictate the location of the zeros of the filter and in turn are adjusted adaptively to yield the minimum mean-square of the error $e(n) = x(n) - \hat{x}(n)$ as defined by Fig. 3. In the next section, an optimal set of weights w for the minimization of $E[e^2(n)]$ will be discussed. Note that E here denotes the expectation operator.

Calculation of Optimum Adaptive Weights With CCLs (Refs. 18, 24).

First, the optimal weights w_i will be derived in the sampled data (digital) form and then they will be converted to their equivalent analog form. For notational compactness, Eq. (1) is rewritten in vector form as Eq. (5).

$$\hat{x}(n) = \bar{w}^T \bar{X}(n) \quad (5)$$

where

$$\bar{w}^T \triangleq [w_0 \ w_1 \ \dots \ w_N]$$

$$\bar{X}(n) \triangleq \begin{bmatrix} x(n) \\ x(n-1) \\ \vdots \\ x(n-N) \end{bmatrix}$$

Observe that the time index n implies the instant of time $n\tau$, where τ is the sampling period. For the ease of notation, the period τ will not be carried explicitly in the subsequent development. In order to find an optimal value W_{opt} of the weight vector \bar{W}^T , the LHS of Eq. (6) must be minimized.

$$E[\{x(n) - \hat{x}(n)\}^2] \geq 0 \quad (6)$$

Substituting Eq. (5) into Eq. (6) yields the following result for the mean-square error:

$$E[e^2(n)] = E[\{x(n) - \bar{W}^T \bar{X}(n)\} \{x(n) - \bar{X}^T(n) \bar{W}\}] \quad (7)$$

where

$$\bar{W}^T \bar{X}(n) = \bar{X}^T(n) \bar{W}$$

By expanding the RHS of Eq. (7), Eq. (8) results.

$$E[x^2(n) + \bar{W}^T \bar{X}(n) \bar{X}^T(n) \bar{W} - 2x(n) \bar{W}^T \bar{X}(n)] = E[x^2(n)] + \bar{W}^T R_{xx} \bar{W} - 2\bar{W}^T R_{x\bar{X}} \quad (8)$$

where

$$R_{xx} \triangleq E[\bar{X}(n) \bar{X}^T(n)], \text{ the covariance matrix of } x(n)$$

$$R_{x\bar{X}} = E[x(n) \bar{X}(n)], \text{ the correlation vector of } x(n) \text{ and } \bar{X}(n)$$

The minimization of Eq. (8) requires differentiating it with respect to

the weight vector \bar{W} and equating the result to zero. Thus

$$\frac{\partial}{\partial \bar{w}} E[x^2(n)] + \bar{W}^T R_{xx} \bar{W} - 2\bar{W}^T R_{x\bar{X}} = 2R_{xx} \bar{W} - 2R_{x\bar{X}} = 0 \quad (9)$$

For carrying out the above differentiation, the following scalar-vector differentiation rules were used:

$$\frac{d}{da} a^T B a = (B + B^T) a$$

and for symmetric B,

$$\frac{d}{da} a^T B a = 2Ba$$

$$\frac{d}{da} a^T B = B$$

where

B = a square matrix

a = a vector of compatible number of elements

The result of solving Eq. (9) for the optimal weight vector \bar{W}_{opt} is given by Eq. (10),

$$\bar{W}_{opt} = R_{xx}^{-1} R_{x\bar{X}} \quad (10)$$

which is referred to as the Wiener-Hopf solution for the MMSE filtering

problem. Equation (10) is also known as the least mean-square (LMS) solution of the adaptive filter problem in the open-loop form.

The open-loop LMS solution to the adaptive filtering problem, conceptually, is simple and straightforward; however, it has the following drawbacks:

1. $n(n+1)/2$ correlations are required for each calculation of R_{xx} .
2. An $n \times n$ matrix inversion is required. If n is large, the processing time is relatively long.
3. To compute the covariance matrices, infinite time records are required to compute their statistics. The actual values used for R_{xx} and $R_{x\bar{x}}$ are only estimates of R_{xx} and $R_{x\bar{x}}$.

The optimal solution of Eq. (10) can also be arrived at, in an iterative manner, via the so-called closed-loop LMS algorithm. The algorithm is also known as the recursive LMS algorithm, steepest descent LMS algorithm, and in its analog form, the CCL.

The recursive LMS algorithm consists of the following iterative steps:

1. Estimate the optimal weight vector with an initial value $\bar{W}(0)$. Note that since \bar{W} is now being arrived at iteratively, a step index (\cdot) is introduced. Thus \bar{W} becomes $\bar{W}(\cdot)$.
2. Calculate the cost function $E[e^2(o)]$ at $\bar{W} = \bar{W}(o)$
3. Calculate the gradient of the cost function with respect to \bar{W} ($\nabla_{\bar{W}} E[e^2(o)]$) at $\bar{W} = \bar{W}(o)$. Note that the gradient at $\bar{W}(o)$ points in the direction of the maximum rate of increase of $E[e^2(o)]$.
4. Adapt \bar{W} to reduce the cost function $E[e^2(o)]$ as much as possible.

Thus,

$$\bar{W}(1) = \bar{W}(0) + k_s \nabla_w^T \{E[e^2(0)]\} \bar{W} = \bar{W}(0)$$

where

k_s = negative constant that dictates the rate of adaptation of $\bar{W}(0)$ towards \bar{W}_{opt}

Steps 1 through 4 are then repeated to arrive at $\bar{W}(2)$. Repeated applications of the above process then yields \bar{W}_{opt} , provided the process converges. The general form of this algorithm is given by Eq. (11).

$$\bar{W}(n+1) = \bar{W}(n) + k_s \nabla_w^T \{E[e^2(n)]\} \bar{W} = \bar{W}(n) \quad (11)$$

where

$\bar{W}(0)$ = some initial estimate

Since the actual value for $E[e^2(n)]$ is not available at each adaptation, the estimate of $E[e^2(n)]$ or simply $e^2(n)$ is used in Eq. (11) to obtain Eq. (12).

$$\bar{W}(n+1) = \bar{W}(n) + k_s \nabla_w^T [e^2(n)] \bar{W} = \bar{W}(n) \quad (12)$$

Equations 13, 14, 15 and 16 are the direct result of the required gradient operation of Eq. (12), via the differentiation rules of page 12.

$$\nabla_w [e^2(n)] = 2e(n) \nabla_w [e(n)] \quad (13)$$

$$\nabla_w [e(n)] = \nabla_w [x(n) - \bar{W}^T(n) \bar{X}(n)] \quad (14)$$

$$\nabla_w [x(n) - \bar{W}^T(n) \bar{X}(n)] = -\bar{X}^T(n) \quad (15)$$

$$\nabla_{\bar{w}}^T [e^2(n)] = -2e(n) \bar{X}(n) \quad (16)$$

The final form of the recursive LMS algorithm given by Eq. (17) results from substituting Eq. (16) into Eq. (12).

$$\bar{W}(n+1) = \bar{W}(n) - 2k_s e(n) \bar{X}(n) \quad (17)$$

Observe that in the recursive LMS algorithm of Eq. (17), no explicit calculation of a correlation matrix and a correlation is required. The recursive LMS algorithm of Eq. (17) is useful for digital processing. For analog processing (for use in analog adaptive filters), the above difference equations can be converted into an equivalent differential equation as follows:

$$\bar{W}(n+1) - \bar{W}(n) = -2k_s e(n) \bar{X}(n)$$

Divide by T on both sides of the above equation,

$$\frac{\bar{W}(n+1) - \bar{W}(n)}{T} = -2 \frac{k_s}{T} e(n) \bar{X}(n) \quad (18)$$

For a sufficiently small sampling interval T, the LHS of Eq. (18) becomes $d\bar{W}/dt$; and Eq. (18) becomes Eq. (19), which can also be represented by Eq. (20).

$$\frac{d\bar{W}}{dt} = -2\mu_s e(t) x(t) \quad (19)$$

$$\bar{W}(t) = -2\mu_s \int_{-\infty}^t e(\tau) x(\tau) d\tau \quad (20)$$

where

$\mu_s = \frac{k_s}{T}$ is the convergence factor that controls the adaptation speed Equation (20) represents the analog version of the LMS adaptive filter which is illustrated in Fig. 4. Note that the LMS recursive

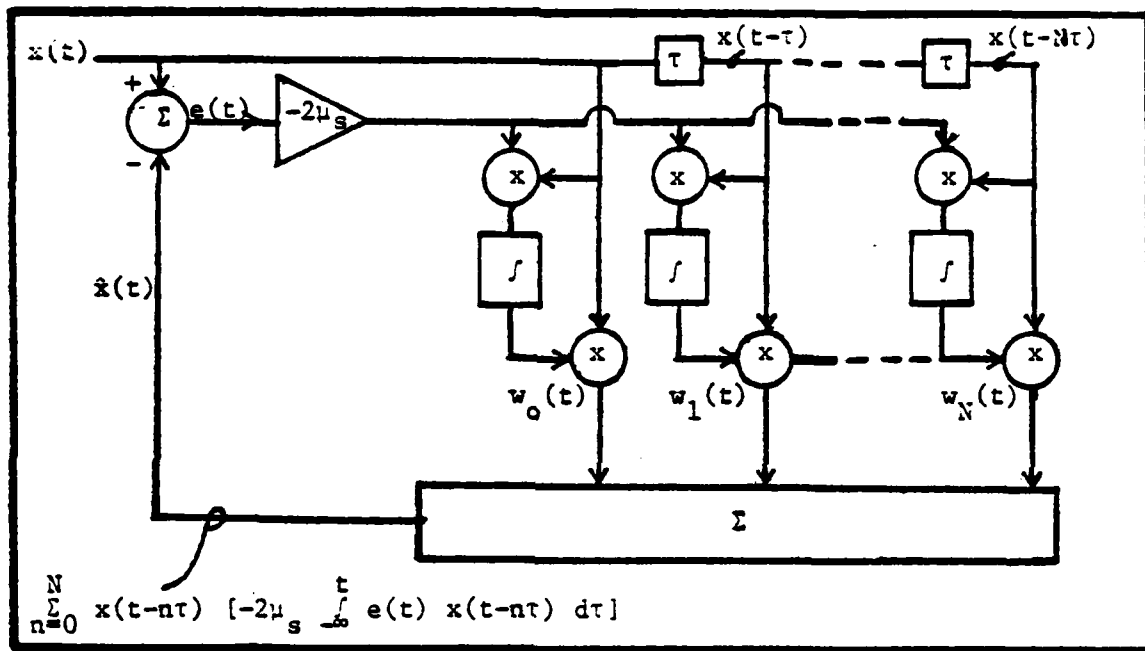


Fig. 4. An Analog LMS Adaptive Filter (Refs. 22:145, 24:21).

solution given by Eq. (17) must arrive at the optimal weight \bar{W}_{opt} of Eq. (10) when the iterative process is over. In fact, it can be shown as $n \rightarrow \infty$ and if k_s is chosen properly $\bar{W}(n)$ converges to \bar{W}_{opt} ; or more precisely $\lim_{n \rightarrow \infty} E[\bar{W}(n)]$ approaches \bar{W}_{opt} .

The above LMS analog filter consists of N correlation cancellation loops (CCL). A single CCL of Fig. 4 is illustrated in Fig. 5. Each CCL cancels the input component which is correlated with a delayed version of the input. Just as $\bar{W}(n)$ reaches \bar{W}_{opt} as $n \rightarrow \infty$, (as $t \rightarrow \infty$), the expected

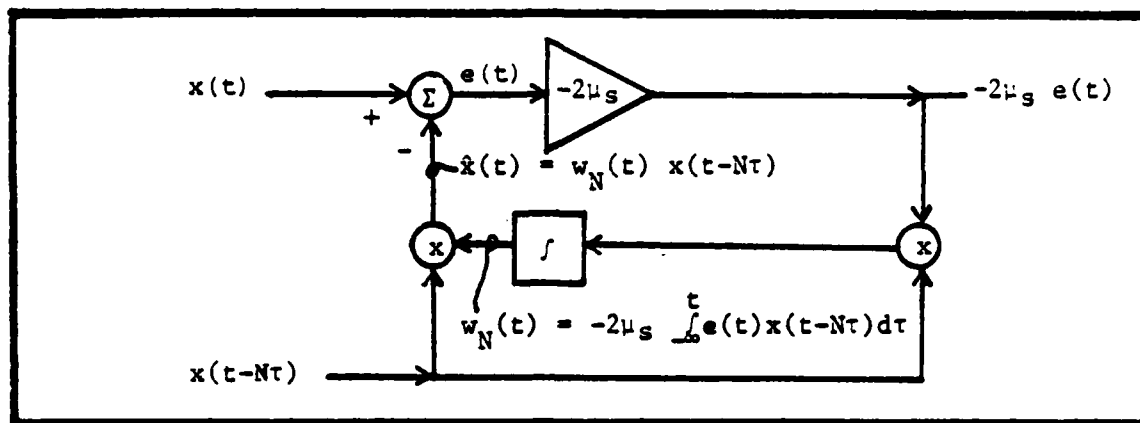


Fig. 5. The Nth Correlation Cancellation Loop of Fig. 4.

value of each linear tap weight $w_N(t)$ approaches the optimum weight required by Eq. (10).

In summary then, it has been demonstrated that an ALP can be designed by using several CCLs in a closed-loop feedback system as in Fig. 4. Furthermore, the CCL method for ALP can be interpreted as implementing the analog version of the recursive LMS algorithm directly, without intermediate computations. The CCL processor is computationally simple to implement and can be used for tracking nonstationary signals continuously rather than discretely by data blocks.

In the next section, a discussion of the fundamentals of Optical Signal Processing used in OAF and OAFFI will include Fourier optics and acousto-optics.

Fundamentals of Optical Signal Processing

OSP has an enormous advantage over current digital signal processing techniques in the areas of larger BW (50 MHz - 1 GHz), parallel processing, real-time performance, simplicity, size and cost (Refs. 1:22, 22:140). OSP requires a light source, light modulator, light detector and numerous lenses to implement the principles of

Fourier optics and acousto-optics (AO). The main asset of Fourier optics is the accomplishment of the Fourier transform (spatial frequency response) of a light distribution (message) in real-time by a converging lens (Ref 9:83).

Fourier Optics (Ref. 9)

The Huygen-Fresnel equation best represents the propagation of light as a wave. In the far field or the focal plane of a lens, the Fraunhofer equation can be used as a simplified form of the Huygen-Fresnel equation (Ref 9:61). These equations (based on the laws of diffraction) are instrumental in developing the Fourier transforming and imaging principles of Fourier optics.

Fourier Transforming Principles (Ref. 9)

The Fourier transforming configurations of a lens and object are illustrated in Fig. 6. The Fourier transforming configuration "b" (Object placed in front of the lens) is used in OAF and OAFFI. Therefore, only configuration "b" will be discussed.

A normally incident monochromatic plane wave of uniform amplitude A illuminates the object located at distance d_o in front of the lens (see Fig. 7). The amplitude transmittance of the object is represented by \bar{t}_o . $\bar{F}_o(f_x, f_y)$ represents the Fourier spectrum of the light transmitted by the object as in Eq. (21).

$$\bar{F}_o(f_x, f_y) = FT\{A\bar{t}_o\} \quad (21)$$

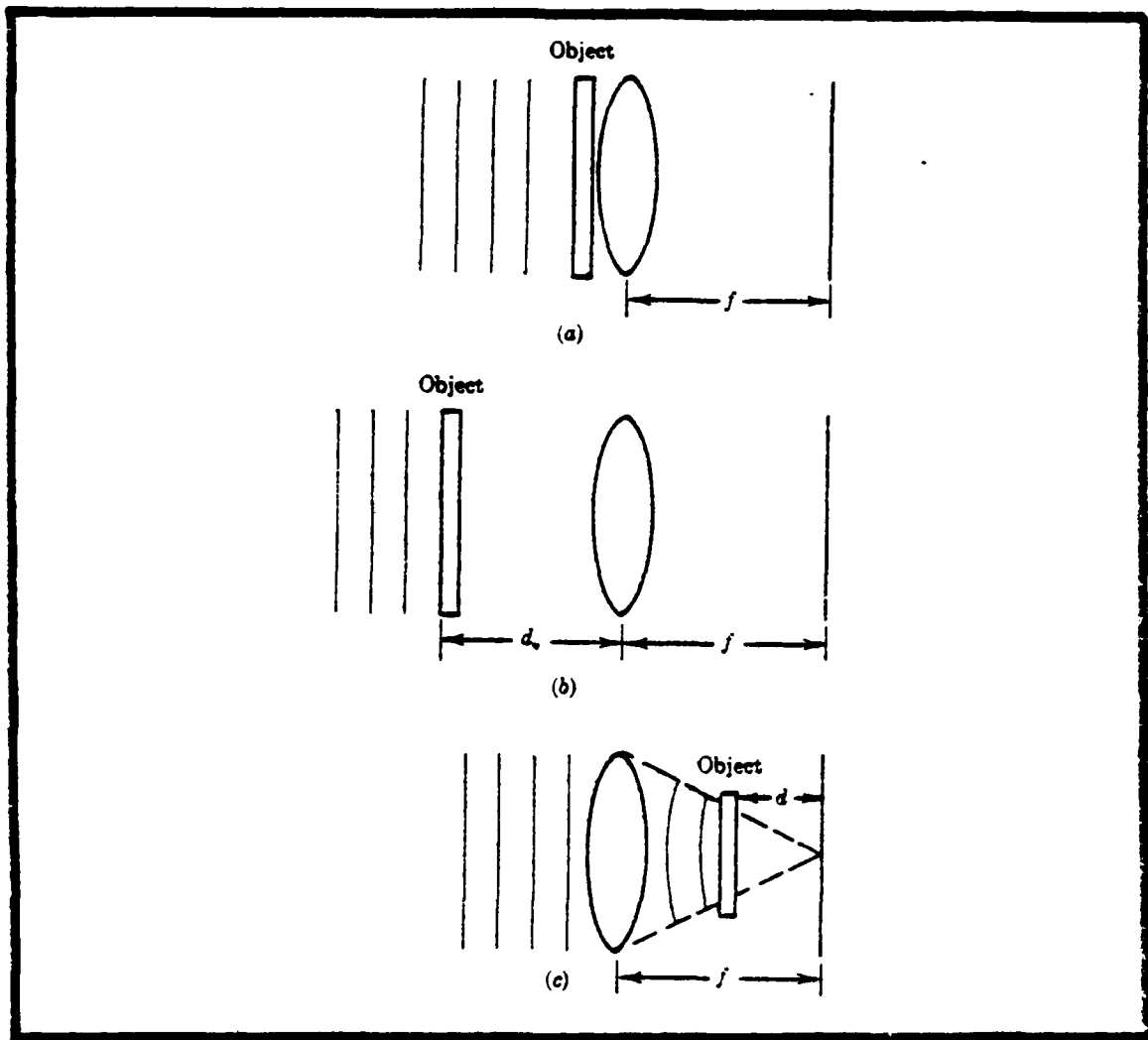


Fig. 6. Fourier Transforming Configurations (Ref. 9:84)

- a.) Object placed against the lens
- b.) Object placed in front of the lens
- c.) Object placed behind the lens

$\bar{F}_1(f_x, f_y)$ represents the Fourier spectrum of the light incident on the lens (U_1) as given by

$$\bar{F}_1(f_x, f_y) = FT\{\bar{U}_1\} \quad (22)$$

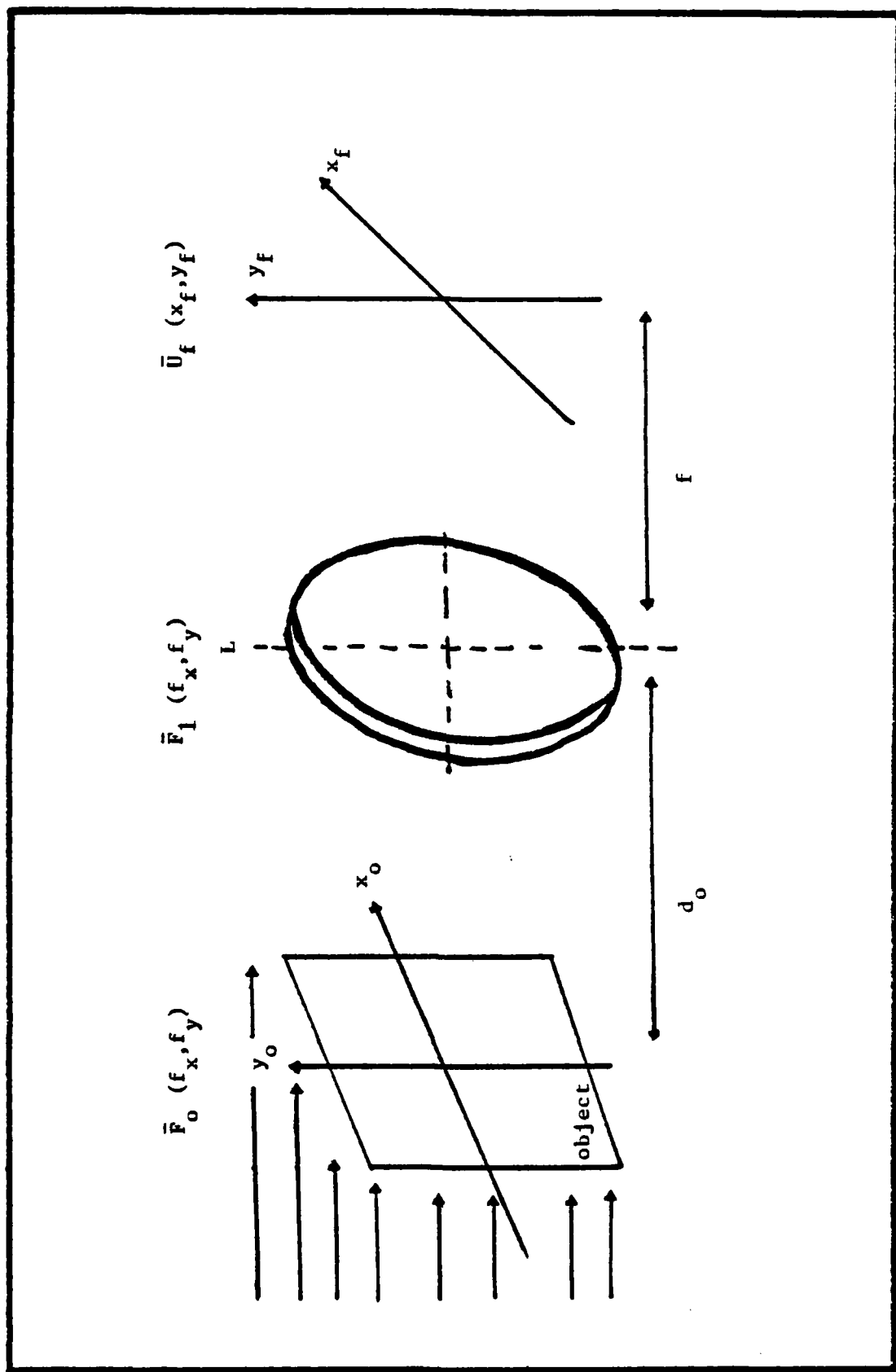


Fig. 7. Single Lens with Object Placed in Front of the Lens (Ref. 28:2-2)

Fresnel approximations over the distance d_o with the help of Eq. (23) describes the relationship of \bar{F}_o and \bar{F}_1 in Eq. (24).

$$\bar{H}(f_x, f_y) = \exp(jkz) \exp[-j\pi\lambda z(f_x^2 + f_y^2)] \quad (23)$$

where

$\exp(jkz)$ = constant phase delay term to be dropped

$$\bar{F}_1(f_x, f_y) = \bar{F}_o(f_x, f_y) \exp[-j\pi\lambda d_o(f_x^2 + f_y^2)] \quad (24)$$

where

d_o = object distance for z

Equation (23) is the transfer function which describes the effects of propagation in the region of Fresnel diffraction.

Eq. (25) represents the output at the back focal plane (Fourier plane).

$$\bar{U}_f(x_f, y_f) = \frac{A \exp[j\frac{k}{2f}(1 - \frac{d_o}{f})(x_f^2 + y_f^2)]}{j\lambda f} \iint_{\infty}^{\infty} t_o(x_o, y_o) \exp[-j\frac{2\pi}{\lambda f}(x_o x_f + y_o y_f)] dx_o dy_o \quad (25)$$

where

$P = 1$ is the pupil function of the lens aperture

The amplitude and phase of the light at coordinates (x_f, y_f) are related to the amplitude and phase of the object spectrum at spatial frequencies $(x_f/\lambda f, y_f/\lambda f)$. It is interesting to note that the phase factor, preceding the transform integral, disappears when $d_o = f$. The result is

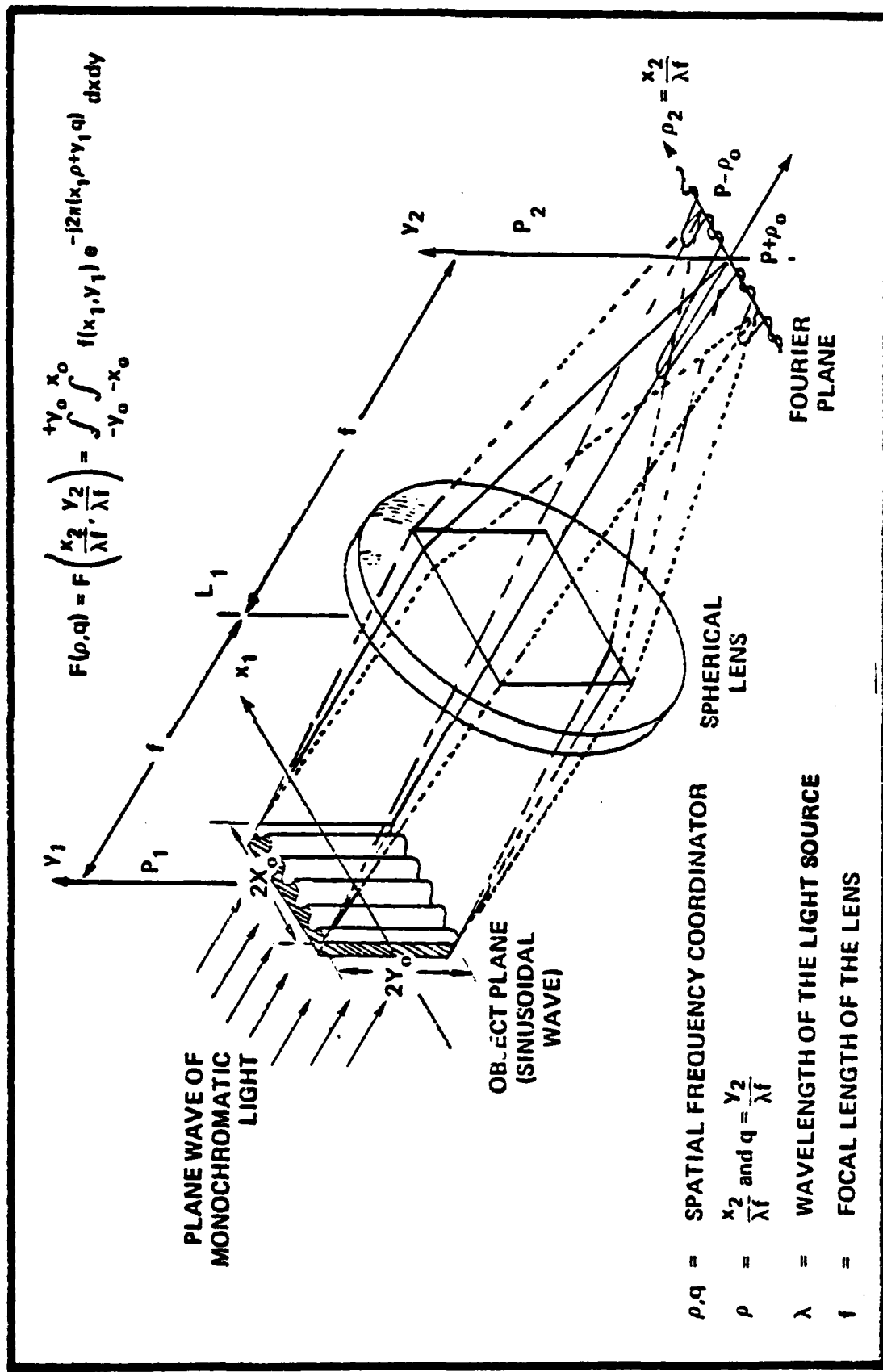


Fig. 8. Optical Fourier Transform System (Ref. 28:2-4)

an exact Fourier transformation (Ref. 9:87). Fig. 8 displays a good graphical representation of an optical Fourier transforming system.

Imaging Principles (Ref. 9)

The imaging principles of Fourier optics can be accomplished by a single lens or a lens pair. First, the imaging principles of a single lens will be discussed.

The field \bar{U}_i of Fig. 9 is represented by the superposition integral in Eq. (26).

$$\bar{U}_i(x_i, y_i) = \iint_{-\infty}^{\infty} \bar{h}(x_i, y_i; x_o, y_o) \bar{U}_o(x_o, y_o) dx_o dy_o \quad (26)$$

The impulse response $\bar{h}(x_i, y_i; x_o, y_o)$ is the field amplitude produced at

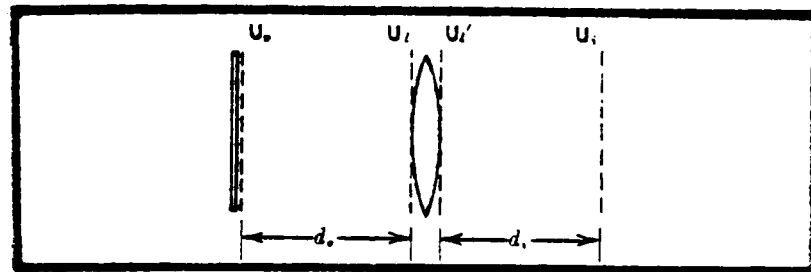


Fig. 9. Geometry For Image Formation (Ref. 9:90).

coordinates (x_i, y_i) by a unit-amplitude point source applied at object coordinates (x_o, y_o) . The impulse response is simplified by considering a distance d_i that satisfies the Lens Law of Eq. (27). Thus, if the

$$\frac{1}{d_o} + \frac{1}{d_i} - \frac{1}{f} = 0 \quad (27)$$

Lens Law is satisfied, the impulse response \bar{h} , given by

$$\bar{h}(x_i, y_i; x_o, y_o) \cong \frac{1}{\lambda^2 d_o d_i} \int_{-\infty}^{\infty} \int_{-\infty}^{\infty} p(x, y) \exp\{-j\frac{2\pi}{\lambda d_i} [(x_i + Mx_o)x + (y_i + My_o)y]\} dx dy \quad (28)$$

where

$p(x, y)$ = pupil function

$$M = \frac{d_i}{d_o} \text{ (magnification)}$$

d_i = image distance

d_o = object distance

Note that \bar{h} is the Fraunhofer diffraction pattern of the lens aperture, centered on image coordinates ($x_i = -Mx_o$, $y_i = -My_o$).

By using some approximations in Eq. (28), i.e. wavelength approaches zero and $p(x, y)$ equals unity, the impulse response can be simplified to the one given by Eq. (29).

$$\bar{h}(x_i, y_i; x_o, y_o) = \frac{1}{M} \delta\left(\frac{x_i}{M} + x_o, \frac{y_i}{M} + y_o\right) \quad (29)$$

If Eq. (29) is substituted into Eq. (26), Eq. (30) results.

$$\bar{U}_i(x_i, y_i) = \frac{1}{M} \bar{U}_o\left(-\frac{x_i}{M}, -\frac{y_i}{M}\right) \quad (30)$$

Equation (30) describes the object and image amplitude distributions derived by geometrical optics. The image $\bar{U}_i(x_i, y_i)$ predicted by geometrical optics is an "exact" replica of the object, magnified and inverted in the image plane (Ref. 9:95).

However, diffraction effects are not included in the "exact"

geometrical optics prediction. To include the diffraction effects, a revised impulse response is necessary to give the exact relationship of object and image in Eq. (31). The included diffraction effects produce the image

$$\bar{U}_i(x_i, y_i) = \bar{h}_r(x_i, y_i) * \bar{U}_g(x_i, y_i) \quad (31)$$

where

$\bar{U}_g(x_i, y_i)$ is the image predicted by geometrical optics according to Eq. (30),

$\bar{h}_r(x_i, y_i)$ denotes the revised impulse response, and is given by

$$\bar{h}_r(x_i, y_i) = \int_{-\infty}^{\infty} \int_{-\infty}^{\infty} p(\lambda d_1 x', \lambda d_1 y') \exp[-j2\pi(x_i x' + y_i y')] dx' dy'$$

$$x' = \frac{x}{\lambda d_1}$$

$$y' = \frac{y}{\lambda d_1}$$

Thus, when the diffraction effects of the pupil are included, an image which is a smoothed version of the object is produced in the back focal plane of the lens.

Next, the imaging principles of a lens pair will be discussed (Ref. 28:2-5). A lens pair accomplishes imaging by "Fourier transforming a Fourier transform". The first lens (L1) of Fig. 10 produces the Fourier transform of the object (arrow) at plane P_1 . The second lens (L2) produces the Fourier transform at plane P_2 of the Fourier transform at plane P_1 . The transform of a transform (Ref. 8) is given by Eq. (32).

$$FT\{FT\{f(y_o)\}\} = f(-y_o) \quad (32)$$

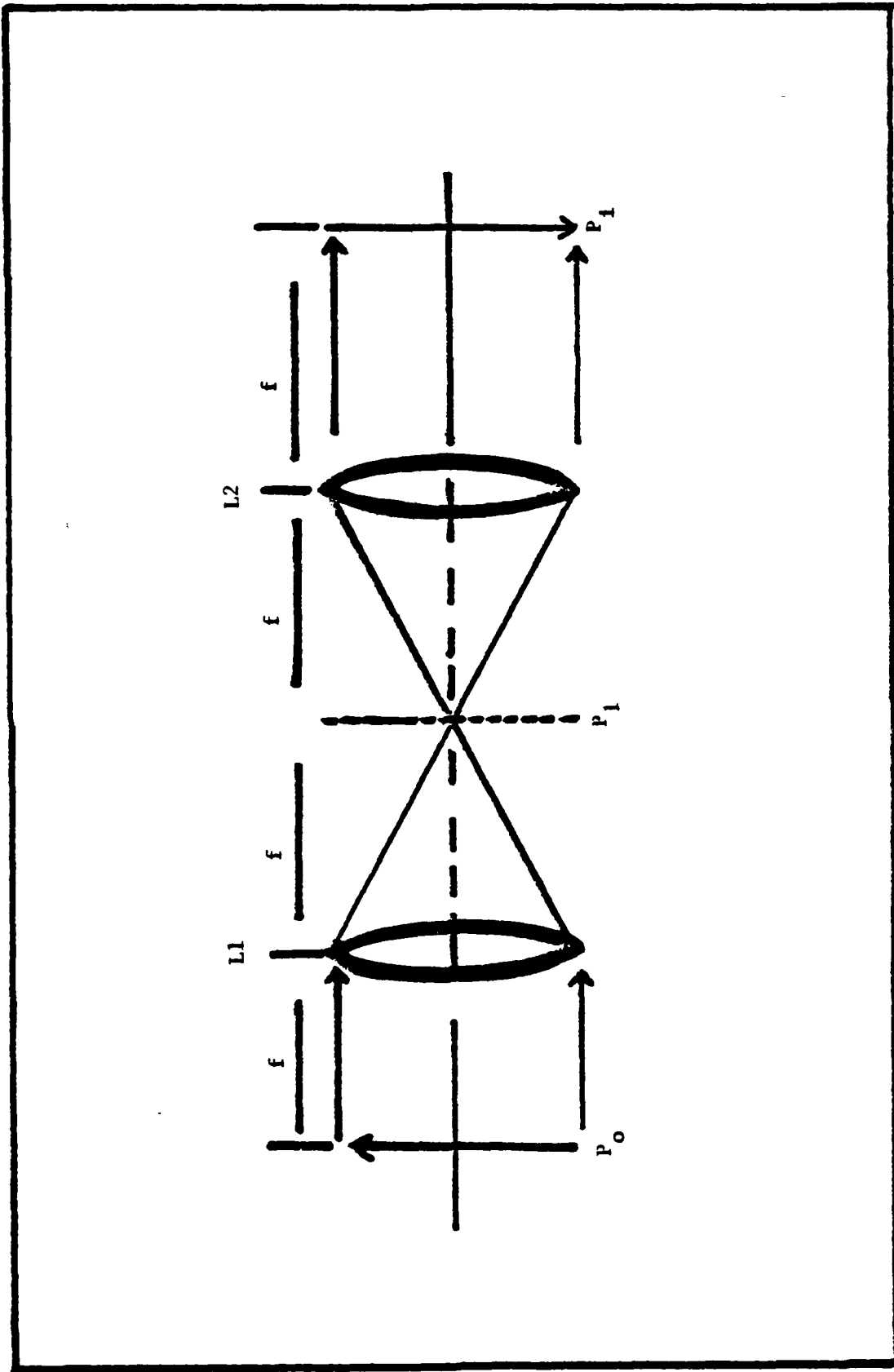


Fig. 10. Two-Lens System In One-Dimension (Ref. 28:2-6)

Therefore, an inverted image is produced at the output image plane P_1 . One additional benefit of the lens pair (two-lens system) is that the spatial frequency distribution in plane P can be filtered by blocking or excision (notching) techniques (Ref. 28:2-5).

In summary, the Fourier transforming and imaging principles of Fourier optics were discussed. Keep in mind that the Fourier transforms and images described here are achieved in the time that light takes to travel through the optical system. Another important topic of OSP is acousto-optics, which is discussed below.

Acousto-Optics

Acousto-optics is the interaction of sound and light. Bragg cells are the most common and efficient AO modulator available today. They provide the required AO interaction used in OAF and OAFFI. A Bragg cell is a block of transparent material with a piezoelectric transducer on one end (Ref. 25:81). The opposite end is tapered to absorb the acoustic waves and sufficiently loaded (acoustically) to provide an acoustic termination (Fig. 11). The piezoelectric transducer, placed between electrodes, oscillates linearly and at the same frequency as the applied voltage, usually at RF frequencies. Hence, the Bragg cell transforms an electrical signal into an acoustical signal.

After this transformation, the sound wave (message) propagates along the length of the cell. The compressions and rarefractions of the sound wave provides a variable index of refraction, along the length of the cell, which interacts with (scatters) the applied light field (Ref. 29). The index of refraction increases at a compression and decreases at a rarefraction (Ref. 25:81).

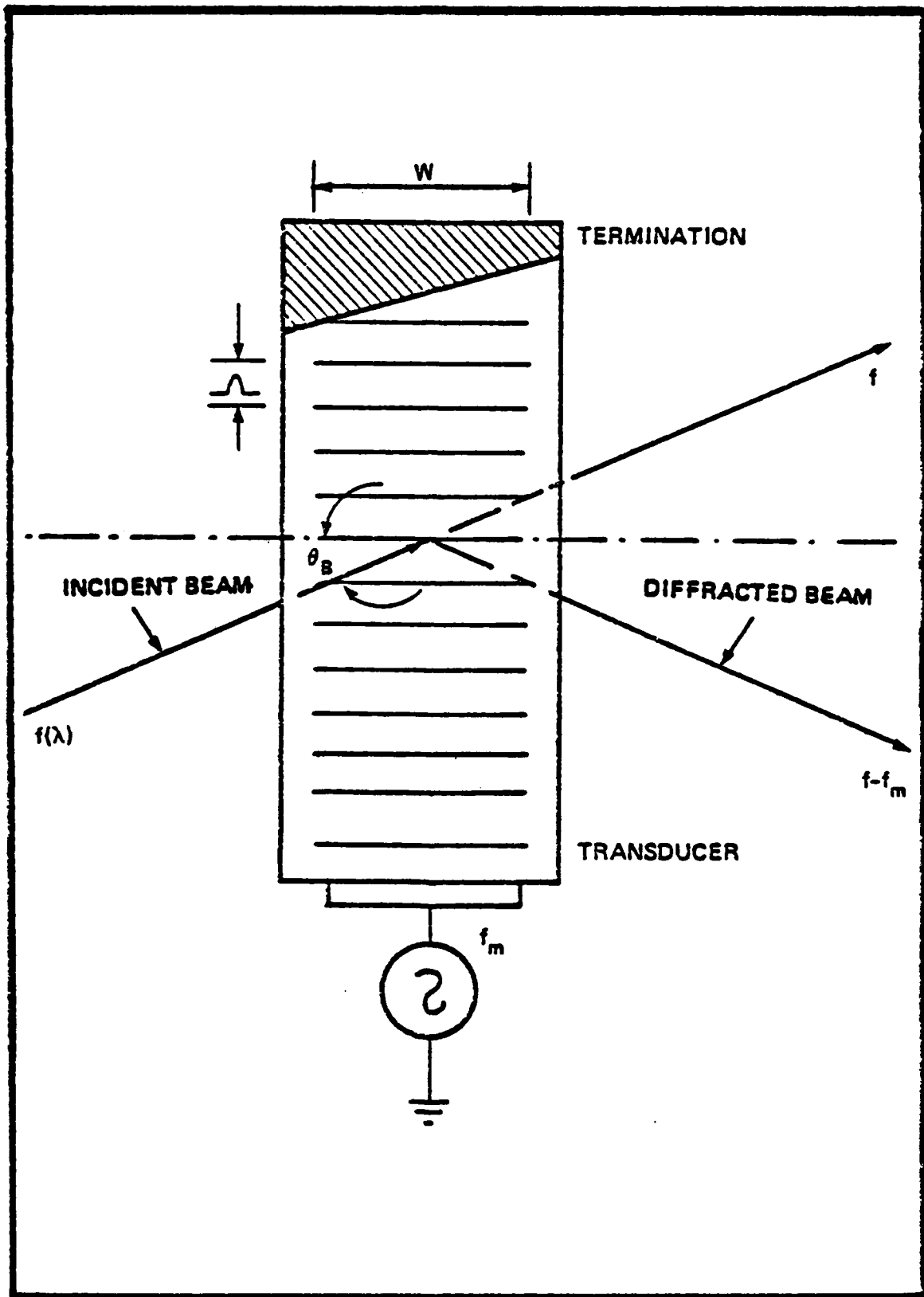


Fig. 11. Bragg Regime Light Diffraction (Ref. 28:3-4)

The Bragg cell also functions as a linear delay line. The signal delay is represented in Fig. 12 by (d/v) , where d represents the

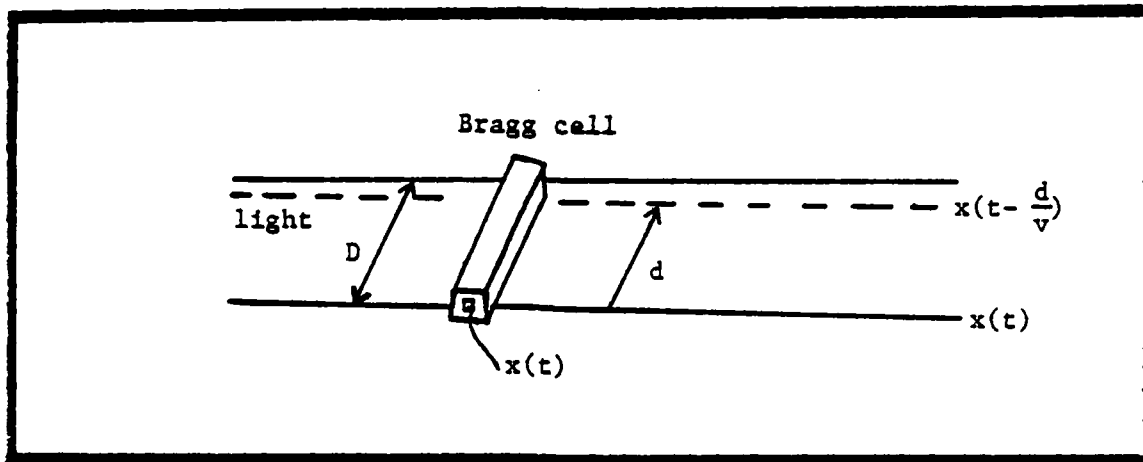


Fig. 12. Bragg Cell as an AO Delay Line (Ref. 22:145).

distance from the transducer and v is the acoustic velocity in the medium. The total time aperture of the Bragg cell is (D/v) , where D is the total length of the Bragg cell window. See Appendix A for additional information on the Bragg cell used in OAFFI.

There are two common modes of Bragg cell operation, based on which optical parameter (amplitude or intensity) of the diffracted light is proportional to the input electrical signal power. To see these, consider an RF sinusoidal signal applied to the Bragg cell with the voltage waveform depicted in Eq. (33).

$$V(t) = V \sin(2\pi ft) \quad (33)$$

The acoustic wave propagates as an optical index of refraction modulation proportional to the input voltage (Ref. 11:149 - 150). The index of refraction modulation is represented by Eq. (34).

$$\Delta n(d, t) = \mu_m \sin [2\pi f(t - d/v)] \quad (34)$$

where

μ_m = amplitude of the index modulation

f = acoustic frequency

d = distance from transducer

v = velocity of sound in medium

The AO grating diffraction efficiency (percentage of light diffracted into the first order for Bragg incidence) is given by Eq. (35).

$$\frac{I_1}{I_0} = \sin^2(n) \approx n \text{ for } n \ll 1 \quad (35)$$

where

I_1 = first-order diffracted intensity

I_0 = zero-order intensity

$$n = \left(\frac{\pi^2 M_2 P_{ac} (L/H)}{2\lambda^2 \cos^2 \theta_i} \right)^{1/2} \approx \left(\frac{V}{2} \right)^2 \propto |V(t)|^2$$

M_2 = figure of merit for Bragg cell material

P_{ac} = acoustic power present in Bragg cell

L = length of transducer in Bragg cell

H = height of transducer in Bragg cell

λ = wavelength of optical source

Equation (35) reveals the two common modes of Bragg cell operation as mentioned above. The first mode (linear in amplitude mode) uses small signals for input to the Bragg cell. Thus, in the case of small signal approximation, the diffracted light amplitude is linearly

proportional to input electrical amplitude. The second mode (linear in intensity mode) uses large signals for input to the Bragg cell. Here, the diffracted light intensity is linearly proportional to input electrical amplitude. The two modes stated above are further illustrated in Figure 13. Small signal and large signal are defined by the required dynamic range of the specific Bragg cell in use.

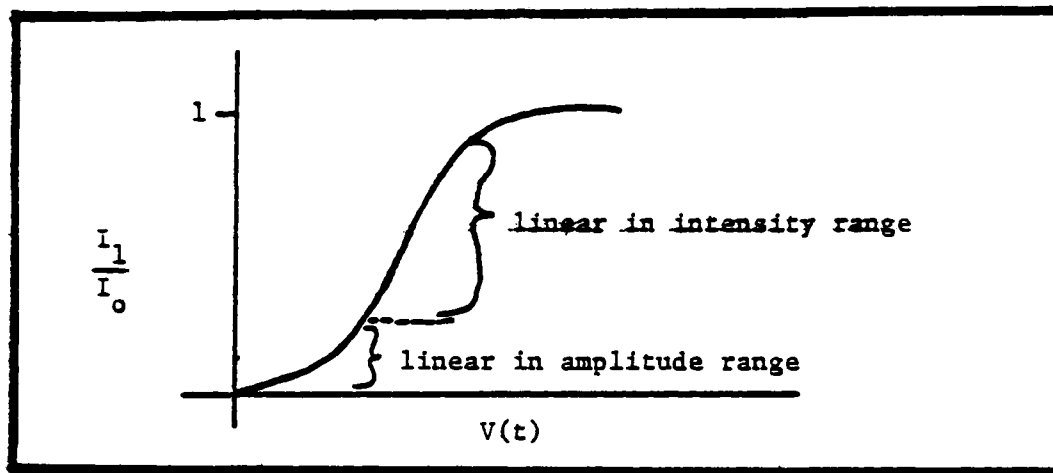


Fig. 13. Ratio of Diffracted Intensity to Incident Intensity Vs. Input Electrical Amplitude.

Note that OAF required the Bragg cell to be operated in the "linear in intensity range" of the curve shown in Fig. 13. Moreover, OAFFI was designed for the Bragg cell to operate in the "linear in amplitude range" of the above curve. However, this was not verified during the OAFFI feasibility test.

The light (carrier), which interacts with the sound wave (message), must be coherent; i.e. single frequency and constant phase, usually obtained from a laser (Ref. 12). A coherent laser beam, at an incident angle θ , strikes the sound wave and is scattered by the variations in refractive index. In general, the scattered light interferes

destructively. However, when Eq. (36) is satisfied (known as the "Bragg condition"), constructive interference occurs.

$$\theta_B = \sin^{-1} \left(\frac{\lambda}{2\Lambda} \right) \quad (36)$$

where

Λ = sound wavelength

θ_B = "Bragg" angle of incidence between light beam and acoustic beam

λ = optical wavelength

Since the sound wave is moving, a "Doppler" frequency shift occurs in the scattered optical beam. Thus heterodyning (frequency shifting) is possible through this interaction of light and sound. The Doppler frequency shift, given by Eq. (37), is also illustrated in Fig. 14.

$$f_d = f_i \pm f_s \quad (37)$$

where

f_d = frequency of diffracted light wave

f_i = frequency of incident light wave

+ = sound wave moving toward f_i

- = sound wave moving away from f_i

f_s = frequency of sound wave

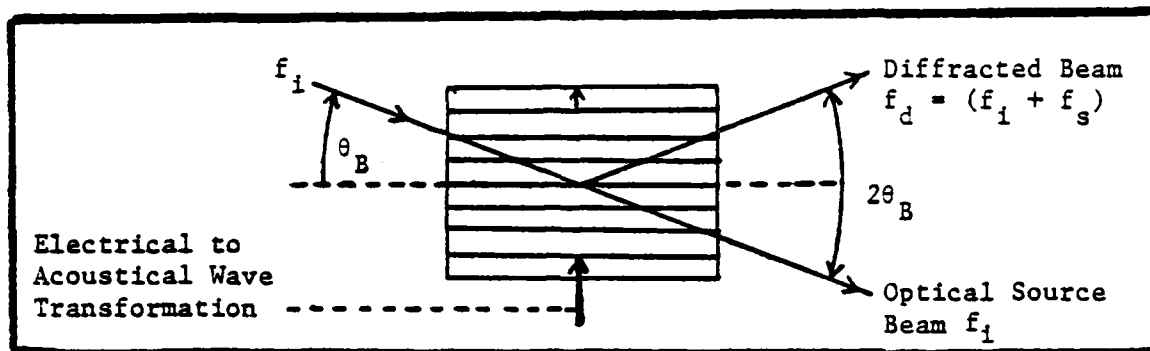


Fig. 14. Bragg Diffraction.

Furthermore, if the frequency of the sound wave is increased by Δf_s , the diffracted optical beam will be "deflected" by an additional amount $\Delta\theta$ as in Eq. (38) and as illustrated in Fig. 15.

$$\Delta\theta = (\lambda/f_s) (\Delta f_s) \quad (38)$$

where

$\Delta\theta$ = change in direction of diffracted beam

λ = optical wavelength

f_s = initial frequency of sound wave

Δf_s = increase in frequency of sound wave

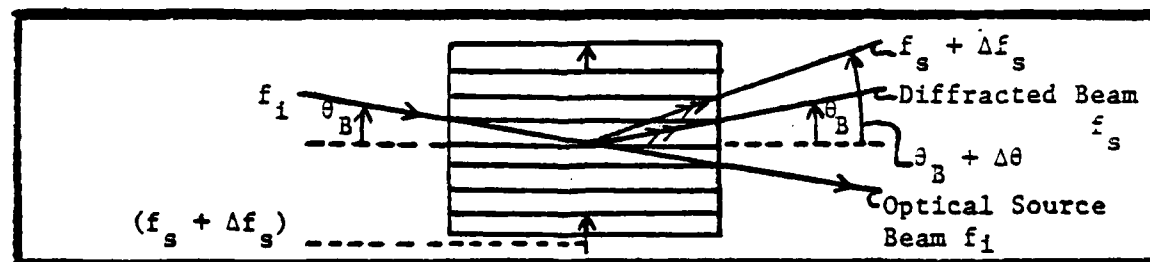


Fig. 15. Deflection of Light Beams by Increasing Sound Frequency (Ref. 29).

Each frequency component (of the signal driving the Bragg cell) diffracts light in a unique direction. The Fourier transform lens

focuses all light diffracted in unique directions into unique positions on its focal plane (the Fourier transform plane). Thus, position on the Fourier transform plane corresponds to frequency driving the Bragg cell and light intensity on the Fourier transform plane relates to power in the corresponding frequency component driving the Bragg cell (Fig. 16).

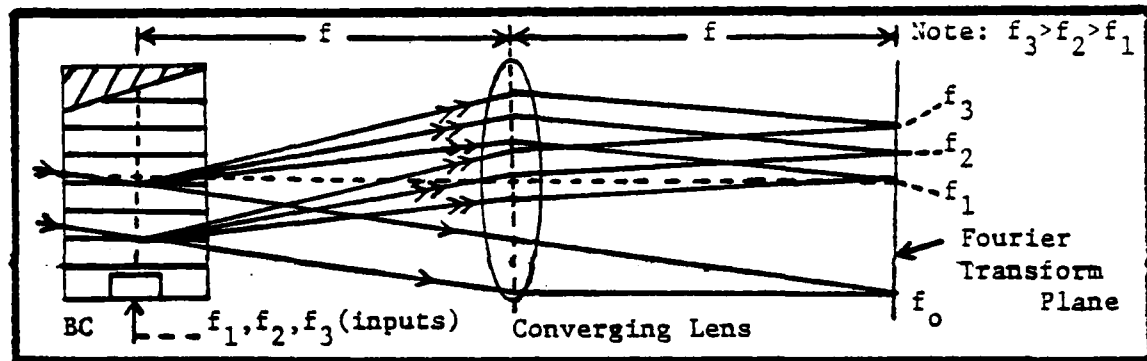


Fig. 16. Demodulation of the Light Spectrum (Ref. 13:51).

In summary, the possible uses of AO Bragg cells are implementation of a linear delay line for parallel processing, heterodyning, large BW (1 GHz) signal processing and almost real-time performance at the speed of light. The Bragg cell is the most efficient AO modulator available today.

Fourier optics and acousto-optics are the fundamental building blocks of OSP. Fourier optics contribute Fourier transforms and images in real-time, while AO contribute parallel processing (in the sense that the Fourier transform is obtained simultaneously for all frequencies) and large BW in real-time. As a result of combining the principles of Fourier optics and AO, OSP accomplishes broadband parallel processing in real-time.

OAF (Ref. 22)

Until now, ALP and OSP were discussed separately. Integrating both of these techniques results in an optical adaptive filter which has many advantages over conventional signal processing schemes. Specifically, the most outstanding advantage over current broadband adaptive filtering architectures is the enormous BW (1GHZ) that can be processed in times limited only by the speed of light (3×10^8 m/sec).

The first adaptive filter to be implemented optically was the Optical Adaptive Filter (OAF), which was implemented in the time domain. The following analysis of OAF is from Ref. 22.

The theory of ALP with CCLs was developed earlier. Briefly restated, (Fig. 4) the estimated signal $\hat{x}(t)$ is computed by Eq. (39).

$$\hat{x}(t) = \sum_{n=0}^N w_n(t) x(t-n\tau) \quad (39)$$

The tap weights $w_n(t)$ are computed by Eq. (40).

$$w_n(t) = -2\mu \int_{-\infty}^t e(t) x(t-n\tau) dt \quad (40)$$

where

$$e(t) = x(t) - \hat{x}(t)$$

$$x(t-n\tau) = \text{delayed input}$$

The RHS of Eq. (40) correlates each delayed version of the input $x(t)$ with the error signal $e(t)$. Once the system reaches steady-state, the tap weights of Eq. (40) are determined.

A Bragg cell can be considered a tapped-delay line. The maximum

number of taps is determined by the time-bandwidth product of the Bragg cell. The time portion of this product is derived from the time aperture or window of the Bragg cell.

An electrical signal $x(t)$ enters the Bragg cell at the transducer end. An acoustic replica of the time-shifted electrical signal is available at a "delay" position "d" in the Bragg cell (Fig. 12). The time-shifted signal, $x(t-d/v)$, in a Bragg cell of width D can be simultaneously processed (resulting in "parallel" processing) with all time-shifted signals in the following range: $0 \leq d/v \leq D/v$. The actual processing that takes place is an intensity modulation of an optical beam, passing through the Bragg cell, by the signals $x(t-d/v)$.

In OAF, the error signal $e(t)$ modulates the intensity of a coherent optical beam via an electrooptic modulator as illustrated in Fig. 17.

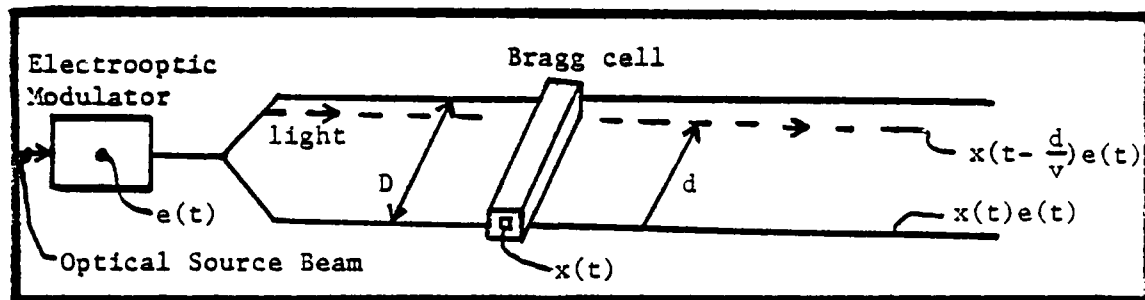


Fig. 17. Modulation of Input Light Intensity by an Electrooptic Modulator and a Bragg Cell (Ref. 22:145)

After passing through the Bragg cell, the optical beam is a modulated intensity product of $x(t-d/v) e(t)$. This product is imaged onto and integrated optically by a Hughes liquid crystal light valve (LCLV). The output of the LCLV is thus the integral $\int x(t-d/v) e(t) dt$ which is the desired correlation integral. The image formation is characteristic of the time domain implementation. See Appendix B for details on the LCLV.

As a result of LCLV processing, the polarization of light exiting the LCLV represents the tap weight values. An analyzer converts polarization to intensity, which is then imaged onto a second Bragg cell. Light whose intensity represents the tap weights w_d illuminates the second Bragg cell, which also receives the input $x(t)$. Diffracted light emerging from that Bragg cell has intensity $w_d x(t-d/v)$ or the resulting products of the tap weights and delayed versions of $x(t)$.

To obtain $\hat{x}(t)$, the products are summed by a photomultiplier tube (PMT). The PMT is an optical-to-electrical transducer. The output, $e(t)$, of a difference amplifier, which performs the subtraction $[x(t) - \hat{x}(t)]$ electrically, is then fed back to the electrooptic modulator as input to achieve a closed-loop structure. This closed-loop feedback system is illustrated in Fig. 18. An optical schematic of the system appears in Fig. 19. For a description of the OSP principles of Fig. 19, see page 141 of Ref. 22.

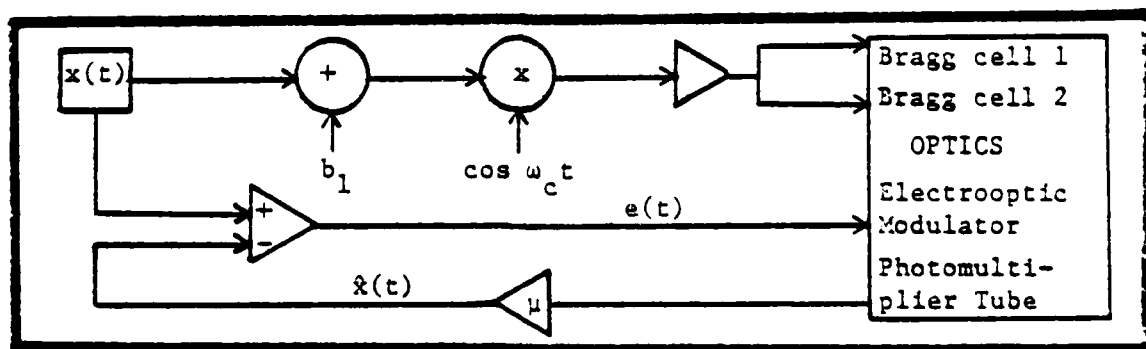


Fig. 18. Optical Adaptive Filter Block Diagram (Ref. 22:145).

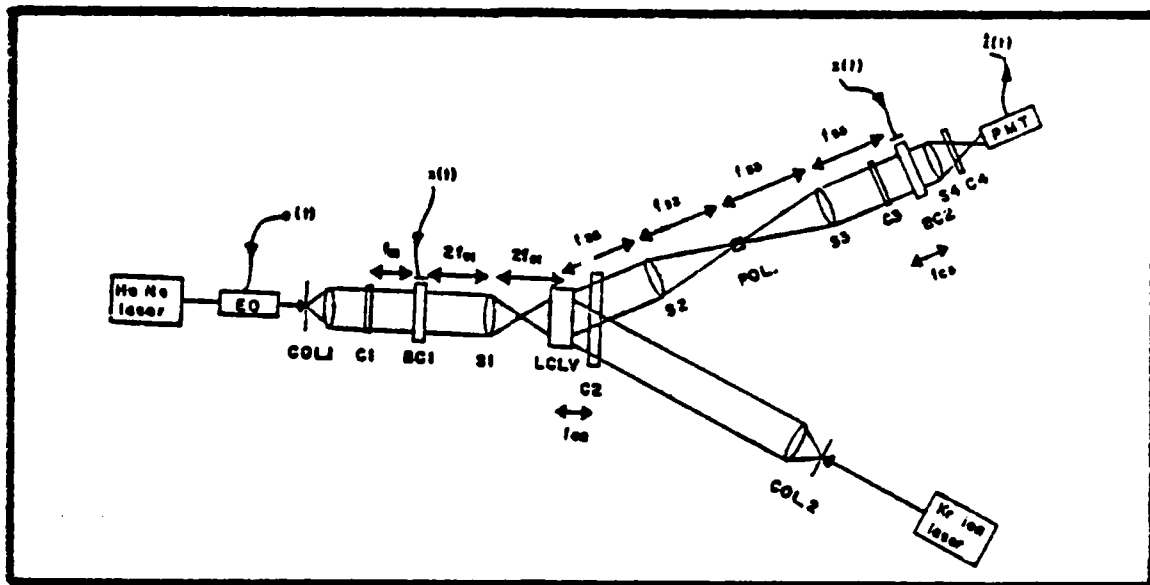


Fig. 19. Schematic of the Optical Portion of the Optical Adaptive Filter (Ref. 22:146). Abbreviations are:

f: focal length POL: polarizer EO: electrooptic modulator
 C: cylindrical lens COL: collimator PMT: photomultiplier tube
 S: spherical lens BC: Bragg cell LCLV: liquid crystal light valve

Two basic operational differences exist between the optical implementation and the CCL architecture of Fig. 4. The light intensity, which is the square of the light amplitude, is always a positive quantity. Also, the LCLV performs a finite integration over time τ (i.e. its output decays with time constant τ) as opposed to a true integration over time from $-\infty$ to the present. The discrete integration time prevents $e(t)$ from reaching a zero value. Since all inputs to the integral function are positive, the integral would increase eternally. However, the finite integration time (τ) enables $e(t)$ to reach a nonzero equilibrium value.

The OAF was tested for feasibility. The experimental results revealed the actual equilibrium values which were reached by $e(t)$. For a 3.6 MHz sinusoidal input, a signal rejection of 20 dB was achieved. For an impulse train input, a signal rejection of 10 dB was observed.

The feasibility test generated some interesting observations. Many problems arose, stemming from equipment characteristics and the architecture of the optical setup. The LCLV required a green light source; however, a red light source (Kr-ion laser) was used instead. Thus, the LCLV had to be driven at a frequency lower than the recommended frequency to achieve an adequate response. The alignment of tap weights must be one-to-one in both size and time-shift between the first Bragg cell and the second Bragg cell. This alignment is very difficult to achieve and requires meticulous adjustments.

Some instabilities were observed in the system, possibly due to the long path length of light and thermal currents. A possible solution to the path length problem is to use lenses with shorter focal lengths.

OAF accomplished linear prediction over a 5 MHz BW. A drawback towards achieving a larger BW was the electrooptic modulator driver, which was limited to a maximum frequency of 10 MHz. Therefore, the maximum available BW was 10 MHz, which was further limited to 5 MHz due to some instability problems which caused frequency variations in the phase difference between $x(t)$ and $\hat{x}(t)$.

In retrospect, there were some inherent problems encountered with the architecture of OAF in addition to a severely constrained BW. Also, OAF requires the Bragg cells to be operated in the "linear in intensity range" of the curve of Fig. 13. As a result, the actual BW capability is further limited to about 100 MHz.

In the quest for a feasible optical adaptive filter, other architectures are being considered. To realize the full potential bandwidth of 1 GHz available in state-of-the-art Bragg cells, a

frequency domain approach was investigated. One of these investigations, subject of this thesis, for a feasible frequency domain architecture is the Optical Adaptive Filter: Frequency Domain Implementation (OAFFI).

OAFFI (Ref. 22)

OAFFI is based on the same theory of ALP and OSP as OAF with the exception of modeling changes, which were necessary to implement the frequency domain approach. The following analysis of OAFFI is found in Ref. 22.

In order to implement the frequency domain approach, note that a linear combination of continuously sampled tap weights is used to calculate $\hat{x}(t)$. Therefore, Eq. (39) becomes Eq. (41) and Eq. (40) becomes Eq. (42).

$$\hat{x}(t) = \int w(\tau) x(t-\tau) d\tau \quad (41)$$

$$w(\tau) = -2\mu_g \int e(t') x(t'-\tau) dt' \quad (42)$$

Note that the continuous variable t has replaced the discrete variables n in the above equations. Substitution of Eq. (42) into Eq. (41) results in

$$\hat{x}(t) = \int [-2\mu_g \int e(t') x(t'-\tau) dt'] x(t-\tau) d\tau \quad (43)$$

The Fourier transform of Eq. (43) can be derived simply from Eq. (42) and Eq. (41). From the convolution property of Fourier transforms (Ref. 20:32) given by Eq. (44),

$$f(t) = \int_{-\infty}^{\infty} f_1(\tau) f_2(t-\tau) d\tau \Leftrightarrow F_1(\omega) F_2(\omega) = F(\omega) \quad (44)$$

Eq. (41) becomes Eq. (45).

$$\hat{X}(\omega) = W(\omega) X(\omega) \quad (45)$$

From the correlation property of Fourier transforms (Ref. 20:32) given by Eq. (46), Eq. (42) becomes Eq. (47).

$$f(t) = \int_{-\infty}^{\infty} f_1^*(\tau) f_2(\tau+t) d\tau \quad F_1^*(\omega) F_2(\omega) = F(\omega) \quad (46)$$

$$W(\omega) = KE(\omega) X(\omega) \quad (47)$$

where

$K = \text{the constant } -2u_s$

By substituting Eq. (47) into Eq. (45), the Fourier transform of Eq. (43) is realized in Eq. (48).

$$\hat{X}(\omega) = X(\omega) [KE(\omega) X^*(\omega)] = KE(\omega) |X(\omega)|^2 \quad (48)$$

Now to put $\hat{x}(t)$ into a mathematical representation which can be implemented optically, the inverse Fourier transform of Eq. (49) is used.

$$f(t) = \frac{1}{2\pi} \int_{-\infty}^{\infty} F(\omega) e^{j\omega t} d\omega \quad (49)$$

Thus $\hat{x}(t)$, described by Eq. (50), is the inverse Fourier transform of Eq. (48).

$$\hat{x}(t) = \frac{K}{2\pi} \int_{-\infty}^{\infty} E(\omega) |X(\omega)|^2 e^{j\omega t} d\omega \quad (50)$$

Moreover, the Fourier transforms that were used in the above derivation assume an integration time from $-\infty$ to $+\infty$. However, the actual integration time is of finite duration (τ). A computer simulation of the frequency domain implementation using finite integration limits suggested that this implementation would work.

To implement the basic design of OAFFI, as illustrated in Fig. 20, $x(t)$ drives the first Bragg cell (BC_1). By AO principles, BC_1 produces

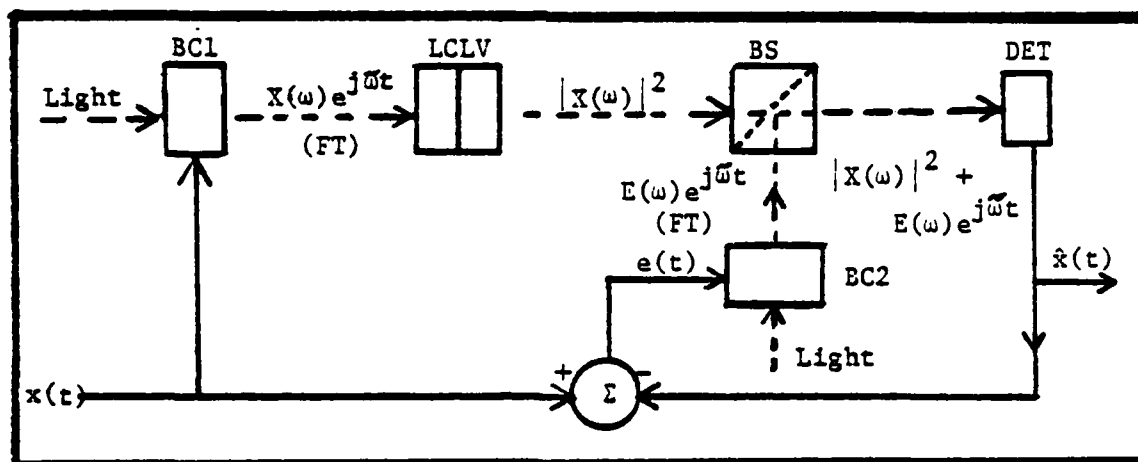


Fig. 20. Optical Adaptive Filter: Frequency Domain Implementation (Ref. 22:147).

the time-shifted signals $x(t-d/v)$, which amplitude modulate the light (optical beam). By the principles of Fourier optics, a spherical lens produces the "Doppler shifted" Fourier transform, $X(\omega) e^{j\omega t}$; which enters the write side of the LCLV. The Fourier transform input to the

LCLV is characteristic of the frequency domain implementation. The LCLV functions as a square law device (Appendix B), producing $|X(\omega)|^2$.

Note that the LCLV is an optical integrator. The signal power spectrum is assumed to vary slowly in relation to LCLV integration time. Therefore, integration effects are ignored and the polarization of the read beam is rotated by an angle $(\alpha + \delta)$, where δ is proportional to the squared modulus of the input light amplitude. The "biasing" angle α is approximately constant and characteristic of the nonilluminated LCLV. An analyzer (polarizer) oriented normal to α , transmits light with amplitude proportional to $\sin \delta$, which for small δ is approximately equal to δ . The analyzer of course blocks light polarized in direction α .

A beam splitter combines the output of the LCLV with the Doppler shifted Fourier transform of $e(t)$. Imaging lenses (Fig. 10) are used to image $|X(\omega)|^2$ onto the photo-detector. Also, a spherical lens is used to produce the Doppler shifted Fourier transform of $e(t)$. Thus, the optical signal amplitude incident on the detector is $|X(\omega)|^2 + E(\omega) e^{j\tilde{\omega}t}$.

The square law detector performs the integration of the received signal with respect to ω , the spatial variable at the detector to yield

$$\int | |X(\omega)|^2 + E(\omega) e^{j\tilde{\omega}t} |^2 d\omega$$

Expansion of this integral yields

$$\int [|E(\omega)|^2 + |X(\omega)|^4 + E^*(\omega) X(\omega) |^2 e^{-j\tilde{\omega}t} + E(\omega) |X(\omega)|^2 e^{j\tilde{\omega}t}] d\omega$$

At equilibrium, the integration of the first two terms produces a constant, or a slowly varying signal which will be dropped for convenience. Since $e(t)$ and $x(t)$ are real, an integration of the last two terms, individually, gives the same results; i.e.

$$\int E(\omega) |X(\omega)|^2 e^{j\bar{\omega}t} d\omega$$

Note that $\omega = 2\pi f_i$ and $\bar{\omega}$ represents Doppler shift of $2\pi f_d$, where $f_d = f_i \pm f_s$.

As a result of these approximations, Eq. (51) is obtained.

$$\hat{x}(t) = 2 \int E(\omega) |X(\omega)|^2 e^{j\bar{\omega}t} d\omega \quad (51)$$

Note that Eq. (51) differs from Eq. (50) by a factor of " $4\pi/K$ ".

Therefore, the detector output is within a constant ($4\pi/K$) of being the inverse Fourier transform of $\hat{X}(\omega)$, which is $\hat{x}(t)$. After passing through a variable gain amplifier, the output of the detector, $\hat{x}(t)$, is subtracted from $x(t)$ electrically to produce $e(t)$. Note that $e(t)$ drives the second Bragg cell (BC_2) and thus, the basic design of the closed-loop system of OAFFI is completed.

OAFFI requires the Bragg cells to be operated in the "linear in amplitude range" of the curve (Fig. 13). This promises to yield the full BW potential of up to 1 GHz. Furthermore, OAFFI does not require an electrooptic modulator, which severely constrained the BW capabilities of OAF to about 10 MHz.

However, a drawback exists in the OAFFI architecture: it is interferometric (see Refs. 3, 4, and 14) and also requires meticulous

optical alignment to achieve the precise registration of $|X(\omega)|^2$ and $E(\omega) e^{j\omega t}$. Also, Shot Noise, which results from the detector's constant terms of integration: $\int [|E(\omega)|^2 + |X(\omega)|^4] d\omega$, will reduce the SNR at the output, $\hat{x}(t)$.

Based on the theory and basic optical design presented here, OAFFI looks promising. This thesis will test the feasibility of OAFFI as an optical adaptive linear predictor.

Summary

In this chapter, the theoretical development of OAF and OAFFI was discussed. The basic fundamentals of ALP and OSP were included in this discussion.

The discussion on ALP covered adaptive transversal filters and calculation of adaptive weights with CCLs. By incorporating these ALP techniques, an optimum method for obtaining the MMSE estimation $\hat{x}(t)$ of the input signal $x(t)$ is achieved.

In addition, the discussion on OSP covered Fourier optics and acousto-optics. By using the principles of Fourier optics, a lens can accomplish Fourier transforming and imaging of an input light distribution. A lens pair can also accomplish imaging of an input light distribution. By using the principles of AO, a Bragg cell functions as a linear delay line; providing the tap weights in the form of $x(t-d/v)$. These tap weights amplitude modulate the optical beam input.

As a result of integrating ALP and OSP, the theoretical basis for OAF and OAFFI was established. Moreover, the most outstanding advantage of ALP with OSP, over current broadband adaptive filtering

architectures, is the enormous BW (1 GHZ) that can be processed at the speed of light.

OAF accomplished linear prediction over a 5 MHz BW. Many problems, concerning electrical components and the particular architecture, were discussed. However, a signal rejection of 20 dB was achieved for a 3.6 MHz sinusoidal input. A signal rejection of 10 dB was also observed for an impulse train input. An optical adaptive filter seems feasible, but the BW potential has not yet been realized.

Therefore, to realize the full potential BW (1 GHZ) in state-of-the-art Bragg cells, a frequency domain approach was developed. OAFFI will entail meticulous optical alignment to achieve the interferometric requirements of the architecture.

In the following chapter, some fundamental OSP schemes will be discussed. These were necessary to understand the principles of the optical architectures leading to OAFFI.

IV. Optical Architectures Leading to OAFFI

Introduction

The OAFFI and various optical systems, sometimes referred to in the sequel as optical architectures, upon which the OAFFI is based, will be the subject of discussion in this chapter. The optical architectures which were built and tested as part of the feasibility test for the OAFFI are:

- 1) Optical Spectrum Analyzer
- 2) Optical Excisor (two versions)
- 3) Liquid Crystal Light Valve

Finally the OAFFI, which was designed and implemented in two versions will be presented.

A detailed discussion, associated theory and laboratory procedure followed during the construction of the above optical systems is presented next.

Optical Spectrum Analyzer

Theory

The Optical Spectrum Analyzer (Fig. 21) was the first optical architecture constructed. The theory of its operation is fundamental to understanding the principles of OAFFI.

The coherent light source was a Spectra-Physics Model 120 He-Ne laser with a red light wavelength λ of 633 nanometers (Ref. 29:170-172). The microscope objective MO focused the optical beam, which contains

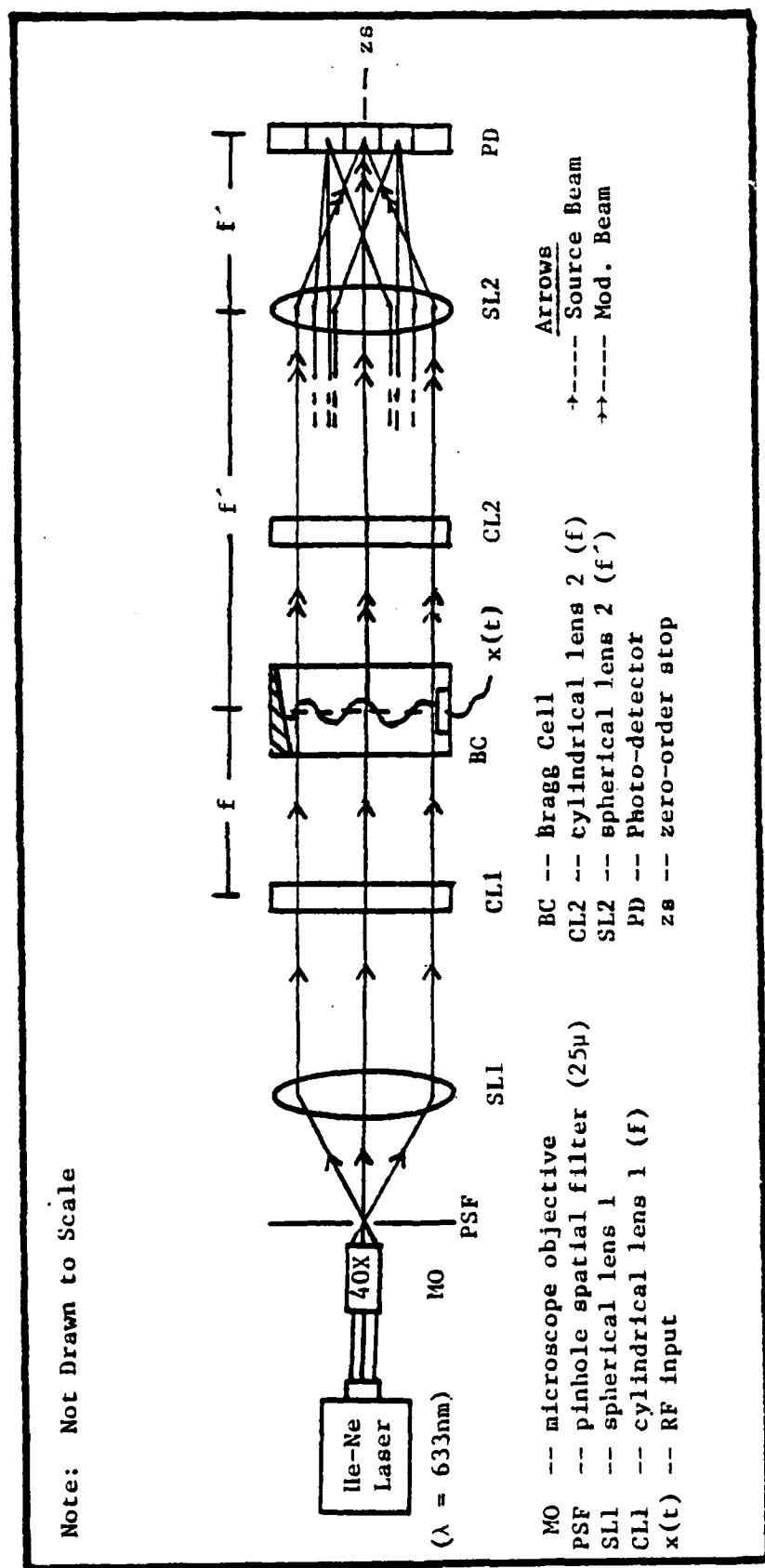


Fig. 21. Optical Spectrum Analyzer (Top View).

scattered or straying rays of light, onto pinhole spatial filter PSF. The PSF removes essentially all spatial frequency components except the zero order. The filtered beam diverges as it travels away from the PSF.

Therefore, a spherical lens SL1 is placed so that the entire lens is illuminated by the diverging optical beam. The SL1 collimates the diverging optical beam for future processing. The cylindrical lens CL1 (focal length f) focuses in the vertical dimension to produce a one-dimensional horizontal line of illumination within the BC.

The Bragg cell BC intensity modulates the light via the AO principles discussed in Chapter III. For a quick review, the Bragg cell is rotated by a horizontal angle θ , with respect to the direction of the incident optical beam, to obtain maximum Bragg diffraction (first-order intensity spot) for a specific RF (radio frequency) input.

The cylindrical lens CL2 (focal length f) expands the one-dimensional, AO modulated line to a two-dimensional optical beam by an anamorphic process. The end result is a collimated beam. In other words, the first cylindrical lens reduces the optical beam to fit the aperture of the Bragg cell. The second cylindrical lens reverses the process of the first cylindrical lens to produce, once again, a collimated beam, which has been AO modulated by the Bragg cell.

Spherical lens SL2 (focal length f') performs a Fourier transform (FT) on the input light distribution, whereby frequency corresponds to spatial position. Thus, a sine wave (single frequency) would result in a spot of light at a single position in the output (photo-detector) plane. Photo-detector PD performs a finite time integration of the intensity received from across the entire Bragg cell; and is a square

law device. The zero-order stop ZS blocks the unwanted DC (unmodulated) spot from the photo-detector. The DC spot is blocked because it contains no useful information and sometimes, the intensity of the DC spot saturates or over-drives the photo-detector. Normally, the detector does not extend to the zero-order. The location of the first and second-order spots is directly related to the specific RF input to the Bragg cell.

Observations

The first observation gained from the optical spectrum analyzer was that a spectrum of spots does appear at the output for an input sine wave. In the actual setup, a white index card was used instead of a photo-detector to view the output spectrum. Four resolvable spots were visible in the output as illustrated in Fig. 22.

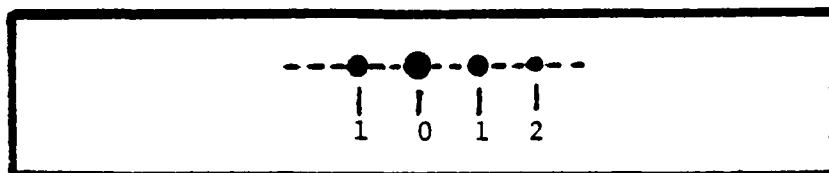


Fig. 22. Optical Spectrum Analyzer Output

The DC (straight-through) beam produced the brightest intensity spot. It is also known as the zero-order spot. The diffracted (modulated) beam produced the first-order spot with a Doppler shift ($f_i \pm f_s$) as stated in Eq. (37). Either one of the first-order spots ($f_i \pm f_s$) can be selected (for maximum intensity) by adjusting the Bragg angle θ_B described by Eq. (36). The diffracted beam also produced a second-order spot. In general, only one of the second-order spots is visible at any one time.

Moreover, as to be expected, the location of the spots depends upon the frequency of the RF input to the Bragg cell. As the RF input frequency was increased, the first-order diffracted spot would move away from the DC spot. As the RF input frequency was decreased, the first-order diffracted spot would move toward the DC spot.

Optical Excisor Version I

Theory

An optical excisor is an optical setup used to select, discern or excise a particular frequency in a broadband signal. Thus, it is in effect a notch filter. Two versions of the excisor were built and tested. The first version of the optical excisor, referred to as Version I is shown in Fig. 23.

An explanation about the workings of the optical setup in Fig. 23 is as follows. The microscope objective MO (40X power) focuses the He-Ne laser beam through the pinhole spatial filter PSF, having a diameter of 25 microns. A filtered optical beam exits the PSF. Spherical lens SL1 collimates the expanding optical beam.

The beam splitter BS1 separates the source beam into two components having equal intensity, which is equal to approximately one-half the intensity of the source beam. The two components consist of a "source" beam which is AO modulated by Bragg cell BC (\leftrightarrow) and a "reference" beam which remains unmodulated (\rightarrow). The unmodulated beam is used as a reference beam to demodulate the modulated beam at the detector. This demodulation results from the interference of the two beams at the detector.

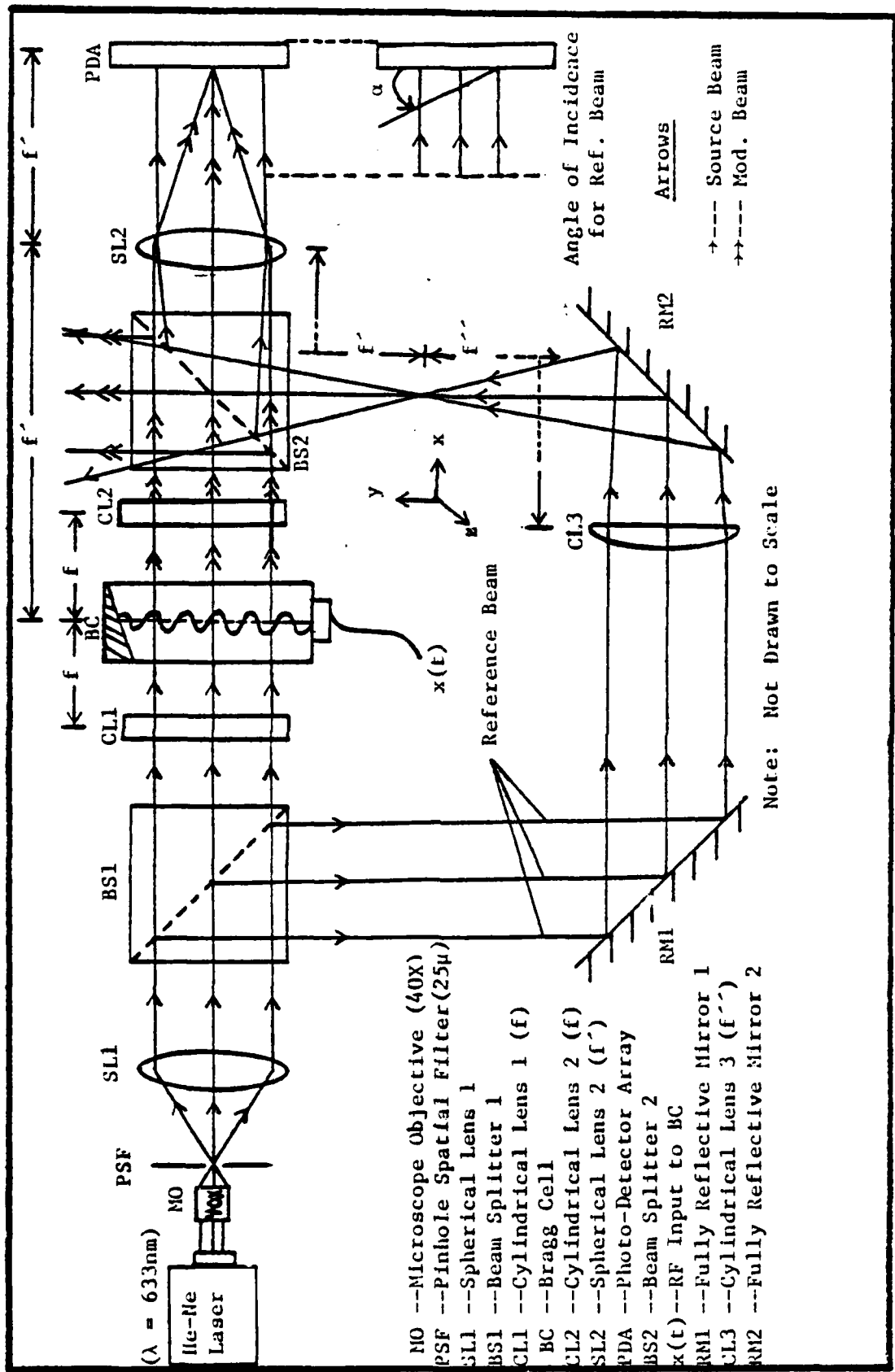


Fig. 23. Optical Excitor Version 1 (Top View).

Cylindrical lens CL1 (focal length f) compresses the two-dimensional optical beam to a horizontal one-dimensional line by an anamorphic process. Bragg cell BC intensity modulates the optical beam via an acoustic replica of $x(t)$. Cylindrical lens CL2 (focal length f) recollimates the expanding beam that exits BC. Beam splitter BS2 recombines the modulated beam (\leftrightarrow) and the unmodulated beam (\rightarrow). Note that one-half of the intensity of each beam is lost by BS2. Spherical lens SL2 (focal length f') performs two functions: Fourier transformation of the modulated beam and collimation of the unmodulated beam.

In the CL3 branch of the interferometer, fully reflective mirror RM1 directs the reference beam to cylindrical lens CL3 (focal length f''). CL3 compresses the reference beam to a line along the z-axis (coming out of the paper) at the focal point f'' . Fully reflective mirror RM2 directs the reference beam to BS2. Note that one-half of the reference beam's intensity is lost at BS2. The reference beam is transformed from a vertical line to a horizontal line at the PDA by SL2. This horizontal line (reference beam) provides multiple frequency detection.

Finally, the photo-diode array PDA used in this setup contains 100 photo-diodes, which can be addressed by two data buses. Hence, a specific frequency can be excised or notched by addressing the appropriate photo-diode(s). The characteristics of photo-diodes are described by Ref. 29:320-328.

In the Optical Excisor Version I of Fig. 23, two optical signals are coincident at the photo-diode array. Each photo-diode is a square

law device. Therefore, each photo-diode outputs a voltage proportional to the local magnitude squared sum of $X(\omega) e^{j\tilde{\omega}t}$, Doppler shifted FT of $x(t)$, and $R e^{j\omega\alpha}$, reference signal delayed by angle of incidence α . By summing the output of all individual photo-diode elements, integration is performed instantaneously across the entire frequency spectrum. Hence, the following operation takes place:

$$\int |X(\omega) e^{j\tilde{\omega}t} + R e^{j\omega\alpha}|^2 d\omega$$

where

$X(\omega)$ = FT of $x(t)$

$e^{j\tilde{\omega}t}$ = Doppler shift provided by Bragg cell

R = magnitude of reference beam

α = angle of incidence of R

expanding the above expression

$$\int (X(\omega) e^{j\tilde{\omega}t} + R e^{j\omega\alpha}) (X^*(\omega) e^{-j\tilde{\omega}t} + R e^{-j\omega\alpha}) d\omega$$

assuming R is real

$$\int [|X(\omega)|^2 + R X(\omega) e^{j\tilde{\omega}(t-\alpha')} + R X^*(\omega) e^{j\tilde{\omega}(\alpha'-t)} + R^2] d\omega$$

Now $\int |X(\omega)|^2 d\omega$ and $\int R^2 d\omega = R\omega$ are biasing terms which will be represented by constant K and

$$\begin{aligned} \int R X(\omega) e^{j\tilde{\omega}(t-\alpha')} d\omega &= \int R X^*(\omega) e^{j\tilde{\omega}(\alpha'-t)} d\omega \\ &= R x(t-\alpha') \end{aligned}$$

therefore

$$\int |X(\omega) e^{j\omega t} + R e^{j\omega\alpha}|^2 d\omega = K + 2R x(t-\alpha')$$

where

$$K = \int |X(\omega)|^2 d\omega + R^2\omega$$

The final expression $[K + 2R x(t-\alpha')]$ is the representation of the biased signal $x(t)$, time-shifted by the incident angle α of the reference beam R . If $\alpha = 0$, there will be no signal delay (with respect to the center of the Bragg cell) in the detected output.

Note that the Optical Excisor Version I is capable of selecting multiple frequencies for excision at the photo-detector. This Optical Excisor uses an asymmetrical (different path lengths) Mach-Zehnder interferometer (see Refs. 3, 4, and 14) to recover the original input signal $x(t)$. This process is known as heterodyning. Also, the asymmetry of the architecture is not critical with the He-Ne laser because it has a coherence length of approximately 1 to 2 meters.

Observations

The Optical Excisor Version I as employed here accomplishes practically nothing, from a classical signal processing viewpoint, since $x(t)$ enters the Bragg cell and $x(t)$ is recovered at the photo-detector. However, from an acousto-optical signal processing viewpoint, this is a very valuable and challenging setup for learning the intricacies of optical design and theory. Since this optical architecture is interferometric, the optical alignment of the equipment is crucial to achieving optimum performance. Therefore, all optical designs which are interferometric should be kept as simple as possible.

The biggest problem encountered with this setup involved the absence of the PDA output on an oscilloscope. A possible cause for this might have been that the horizontal line (reference beam) was saturating the PDA. The PDA is a small semiconductor chip and the horizontal line width (thickness) illuminated the entire aperture of each photo-diode in the PDA.

Another possible cause of no response from PDA might have been the angle of incidence α of the reference beam. If α is greater than some critical angle; phase cancellations in the reference beam arriving at the PDA may squelch the heterodyning process for demodulating $x(t)$.

In addition to this, the assymetry of the optical setup might have contributed to the absence of a PDA output. In particular, the reference beam traveled farther than the modulated beam by an optical path difference of BS1 to RM1 plus RM2 to BS2. Note that a change in relative path length (between both branches of the interferometer) by one wavelength of light coincides with a 360 degree phase change in the output. However, since a He-Ne laser (coherence length = 1 - 2 meters) was used, the former reasons for the absence of a PDA output seems more feasible.

Furthermore, the interferometer portion of the setup was verified to be aligned properly by visual inspection of interference fringes (see Refs. 3, 4, and 14) on a white index card. A pinhole in a white index card proved to be very valuable in aligning the two optical beams to produce interference fringes. Nevertheless, it is very tedious and time consuming to align an optical setup which is interferometric.

Due to the absence of an output from the PDA and the feasible

conclusions stated above, the Optical Excisor Version I was revised to obtain the Optical Excisor Version II. The resulting architecture succeeded where the Optical Excisor Version I had failed.

Optical Excisor Version II

Theory

The Optical Excisor Version II is not a true "excisor" since, as will be shown subsequently, it can only resolve a single frequency. The Optical Excisor Version II (Fig. 24) uses a symmetrical (equal path length) Mach-Zehnder interferometer to recover the original input signal $x(t)$. Again, this process is called heterodyning.

In Fig. 24, microscope objective MO (40X power) focuses the He-Ne laser beam through pinhole spatial filter PSF, having a diameter of 25 microns. A filtered optical beam exits PSF. Spherical lens SL1 collimates the expanding optical beam.

Beam splitter BS1 separates the source beam into two components having equal intensity, which is equal to approximately one-half the intensity of the source beam. The two components consist of a "source" beam which is AO modulated by Bragg cell BC (\leftrightarrow) and a "source" beam which remains unmodulated (\rightarrow). The unmodulated beam is used as a reference beam to demodulate the modulated beam at the detector. This is accomplished through interference of the two coincident beams at the photo-detector.

Again, Bragg cell BC intensity modulates the optical beam via an acoustic replica of $x(t)$. Fully reflective mirror RM1 directs the modulated beam to beam splitter BS2. Fully reflective mirror RM2

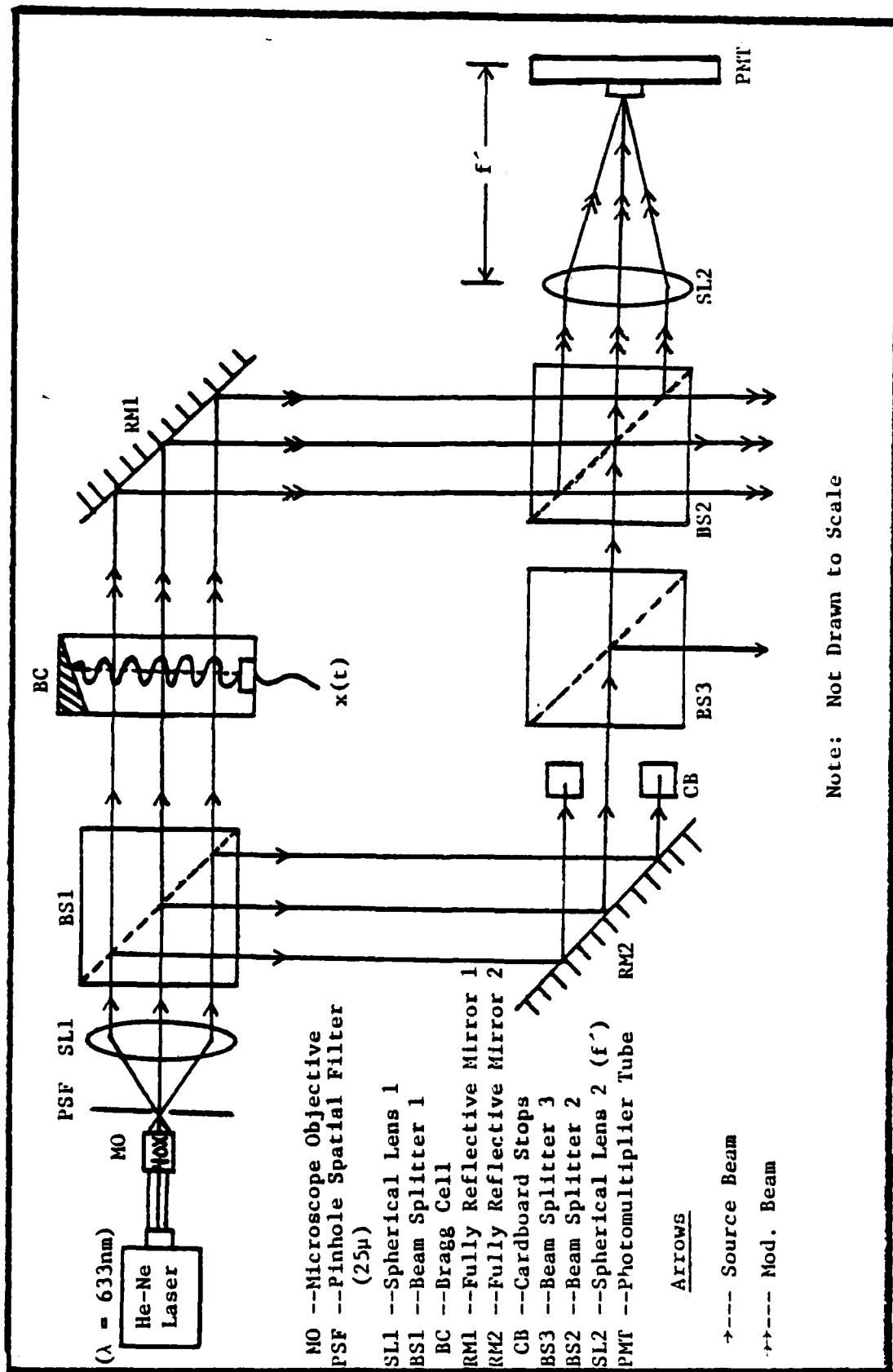


Fig. 24. Optical Excitor Version II (Top View).

directs the unmodulated (reference) beam to beam splitter BS3. The beam splitter BS3 is used merely to reduce the intensity of the reference beam by one-half and passes it to BS2. Also, white index cards (cardboard) CB blocks part of the reference beam being directed to BS3. An explanation for blocking the reference beam will be covered in the next section.

The beam splitter BS2 recombines the modulated beam ($\rightarrow\rightarrow$) and the reference beam (\rightarrow). Note that one-half of the intensity of each beam is lost by BS2. Spherical lens SL2 (focal length f') performs a Fourier transform on the input light distribution which is provided by the modulated beam and the reference beam. The Fourier transform appears at PMT.

Since the reference beam is focused onto a point at the detector, only one frequency component at a time can be reconstructed via heterodyning. In other words, interference is only possible at one frequency. Hence, this is not a "true" excisor; whereas in an excisor, multiple frequencies can be reconstructed simultaneously via heterodyning.

Also, note that the photo-diode array has been replaced by the photomultiplier tube PMT (Photo 1). The characteristics of PMTs are described by Ref. 29:300-309.

Finally, the mathematical theory of the Optical Excisor Version II is the same as that derived for the Optical Excisor Version I. The PMT is also a square law device and accomplishes optical detection similar to that of the photo-diode.

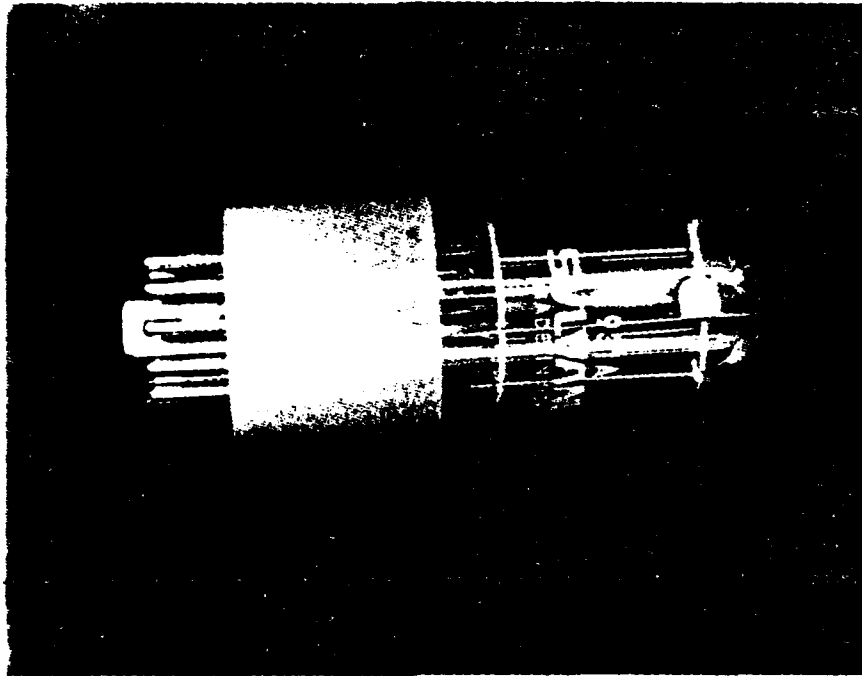


Photo 1. Photomultiplier Tube (931A) Used as a Photo Detector in Optical Excisor Version II and Succeeding Architectures.

Observations

Initially, the PDA was used for photo-detection in the Optical Excisor Version II. An output was achieved with the PDA. However radio frequency interference (RFI) was significant. The source of the RFI was the signal generator for $x(t)$. The RFI was observed on a spectrum analyzer by blocking the optical signal from the PDA. The spectrum analyzer showed a PDA output of 8 - 16dB SNR (RFI) with no optical input to the detector. Therefore, a switch to the PMT was made to solve the RFI problem. The switch to PMT did not completely solve the problem; and in fact, RFI remained a plaguing issue throughout this research effort (Photos 4 and 7). The analysis for the above RFI problem will be shown in a later section (page 149).

In addition, the PMT was very sensitive to the received intensity. Therefore, BS3 and CB were used to reduce input intensity and to keep the PMT from saturating (Photos 5 - 9). Note the reference beam intensity is much greater than the modulated beam intensity exiting the Bragg cell (Fig. 23). Blocking part of the modulated beam (first-order diffracted spot) is not feasible since it contains the information. However, the DC spot which passes straight through the Bragg cell is blocked by a zero-order stop at the PMT.

At first, adjusting CB seemed to help maximize the SNR at the output. The CB was adjusted to block a portion on each side of the reference beam. Without this blockage, it was conjectured that phase cancellations in the reference beam were taking place at the PD. Light rays on the sides of the optical beam would cancel with some light rays in the center and on the opposite side of the optical beam when brought into focus. Later on, however, it was discovered that the white cardboard CB (being slightly translucent) contributed 3dB SNR at the PD as a result of scattered light (page 82).

As a result of seeking the simplest optical architecture for implementing the Optical Excisor Version II, all cylindrical lenses were removed. The SNR results at the PD were not much lower (1 - 2dB) from previous results which included cylindrical lenses (Photos 2 - 4). In fact, by adding the extra beam splitter BS3 to reduce the intensity at the PD; an overall improvement of 4dB was observed (Photos 5 - 7). The result of reinserting CL3 (for multiple frequency detection) in the architecture was a smaller SNR (Photos 8 and 9). Therefore, the cylindrical lenses were eliminated as excess hardware. By removing CL3

from the path of the reference beam, the ability to discern multiple frequencies is forfeited; however, a larger SNR results at the single demodulated frequency.

Since this was the first (for this report) optical architecture (Fig. 24) to display results on an oscilloscope and a spectrum analyzer; it is appropriate to include some observations via photos. For the following photos, the RF input $x(t)$ to the Bragg cell was a 70 MHz sine wave. The Bragg cell (Appendix A) has a center frequency of 70 MHz and a BW of 40 MHz. Also, the PMT was used for the PD. A 70 MHz bandpass filter with a BW of 20 MHz was used in later architectures but not here; therefore, "w/o Filter" indicates that the 70 MHz filter was not used.

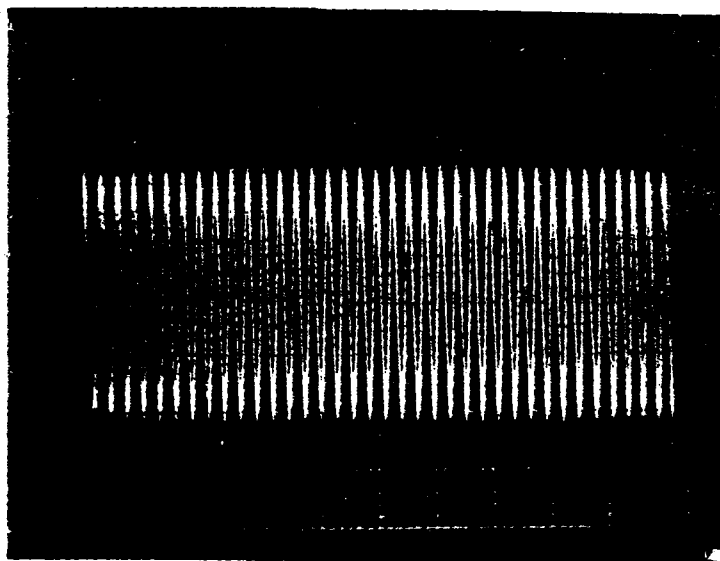


Photo. 2. 70 MHz Optical Signal w/o Filter.
Vert. = 0.2 Volts/Div. (.96 Volts P-P)
Hor. = .05 μ sec/Div. (1 Div. = 3.5 T)

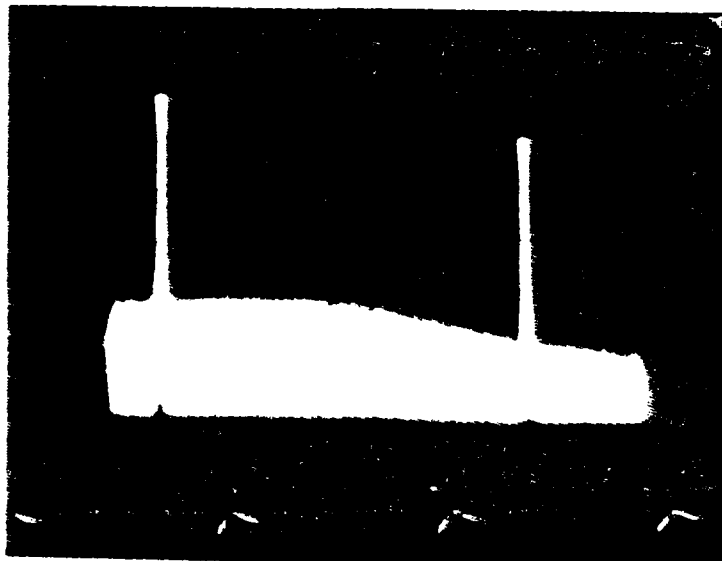


Photo 3. Spectrum of 70 MHz Optical Signal (Photo 2).
Scan Width = 10 MHz/Div.
DC = 40dB SNR, 70MHz = 40dB SNR
Note the Noise "Roll-Off" of the PMT.

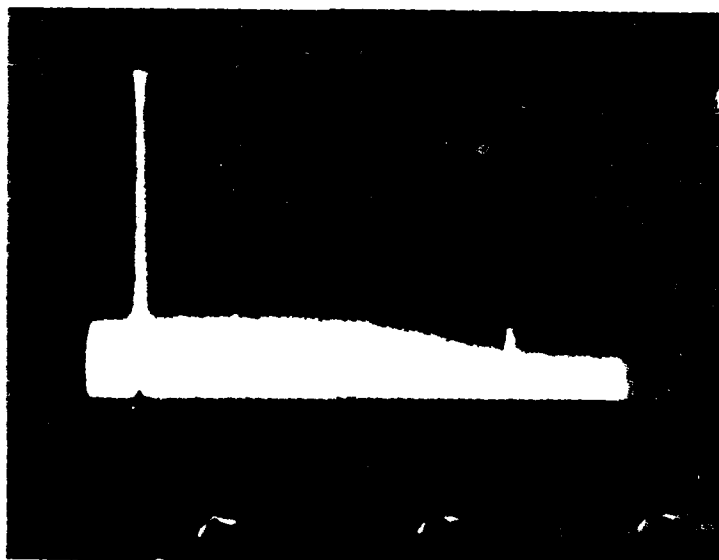


Photo 4. Spectrum of 70 MHz RFI w/o Filter.
Scan Width = 10 MHz/Div.
RFI = 8dB from Noise Floor

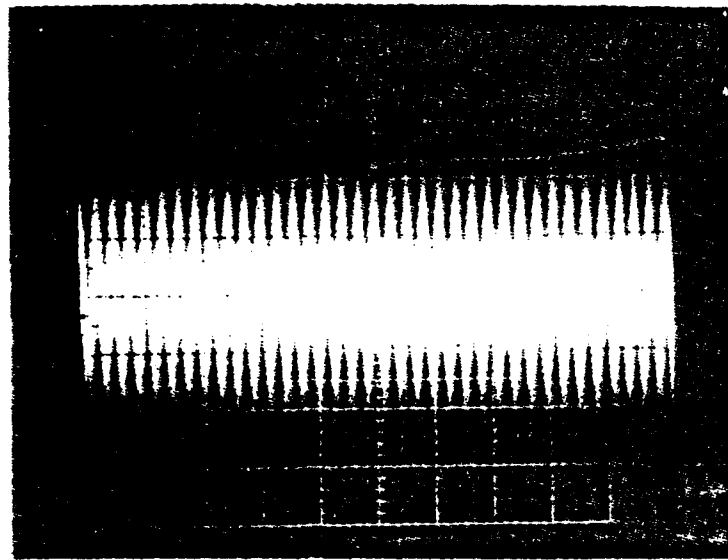


Photo 5. 70 MHz Optical Signal w/o Filter.
 Extra Beam Splitter (BS3) Added to Reference Path.
 All Cylindrical Lenses Removed.
 Vert. = 0.2 Volts/Div. (1.0 Volt P-P)
 Hor. = .05 μ sec/Div. (1 Div. = 3.5 T)

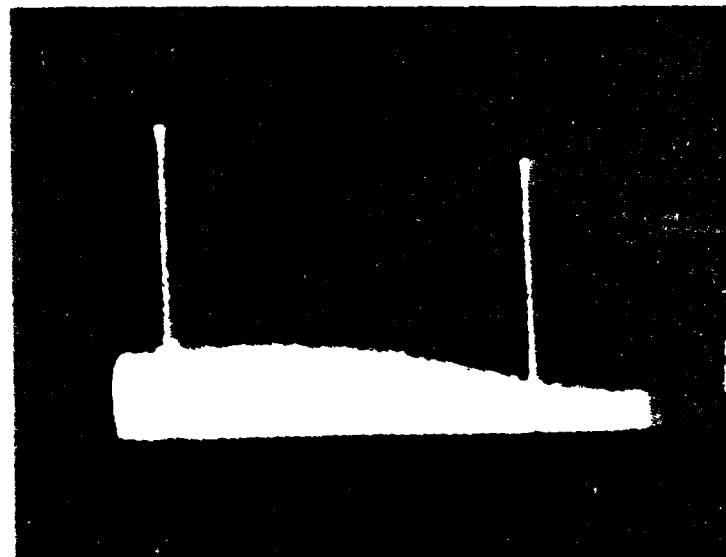


Photo 6. Spectrum of 70MHz Optical Signal (Photo 5).
 Extra Beam Splitter (BS3) Added to Reference Path.
 All Cylindrical Lenses Removed.
 Scan Width = 10 MHz/Div.
 DC = 44dB SNR, 70 MHz = 44dB SNR

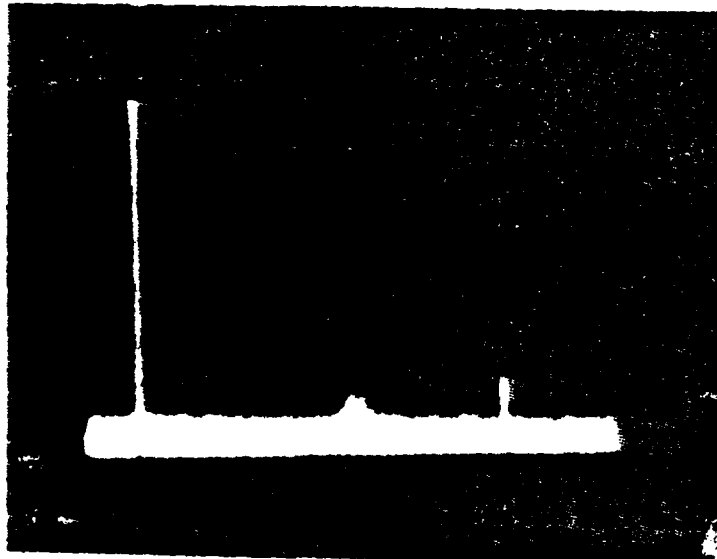


Photo 7. Spectrum of 70 MHz RFI w/o Filter.
Extra Beam Splitter (BS3) Added to Reference Path.
All Cylindrical Lenses Removed.
Scan Width = 10 MHz/Div.
RFI = 16dB from Noise Floor
Note the Mysterious Noise at 42 MHz.

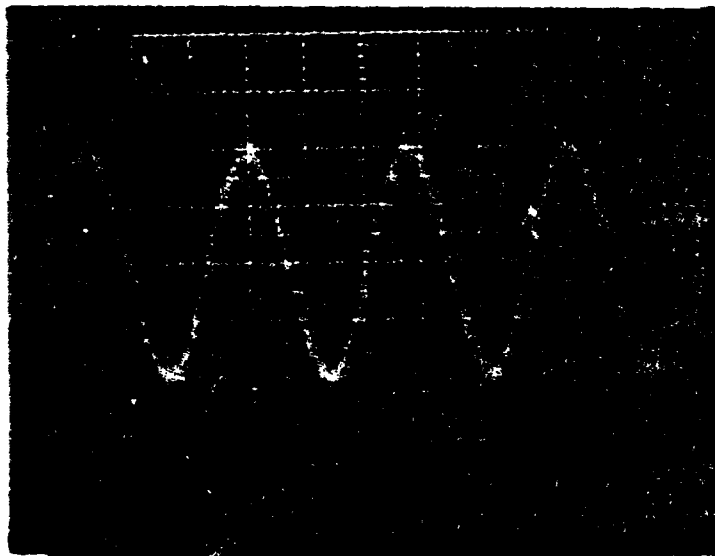


Photo 8. 70 MHz Optical Signal w/o Filter.
Extra Beam Splitter (BS3) and Cylindrical
Lens (CL3) Added to Reference Path.
Vert. = 20 mv/Div (120 mv P-P).
Hor. = .05 usec/Div (10Div. = 3.5 T)

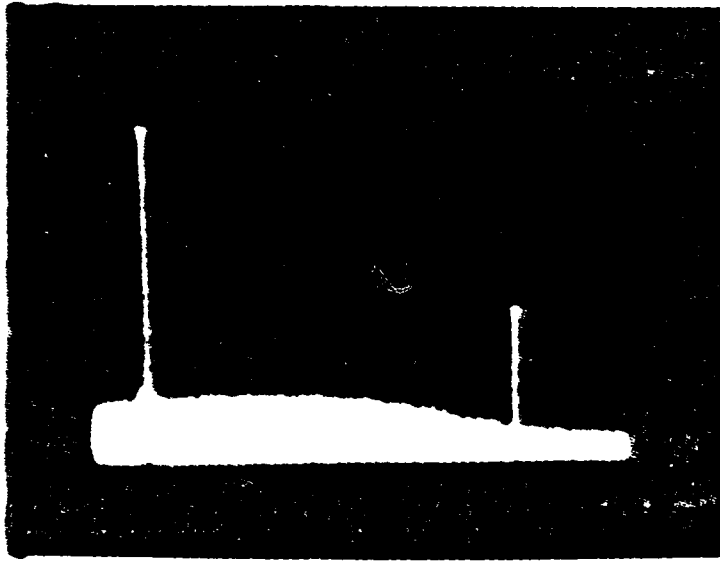


Photo 9. Spectrum of 70 MHz Signal (Photo 8).
 Extra Beam Splitter (BS3) and Cylindrical
 Lens (CL3) Added to Reference Path.
 Scan Width = 10 MHz/Div.
 70 MHz = 22dB SNR

Liquid Crystal Light Valve Test

Theory

The objective of using the LCLV is to produce an optical signal whose amplitude is proportional to the power spectrum squared modulus $|X(\omega) e^{j\omega t}|^2$ of an input signal $x(t)$, which will be imaged onto the PD for subsequent use in OAFFI. A detailed description on the operation of the LCLV is found in Appendix B. Basically, the LCLV is an optical-to-optical transducer which yields a read beam whose polarization is rotated (locally) by an angle that is approximately proportional to the squared modulus of the input light amplitude.

Since the LCLV has a photo response displayed by Fig. 25; an Argon-

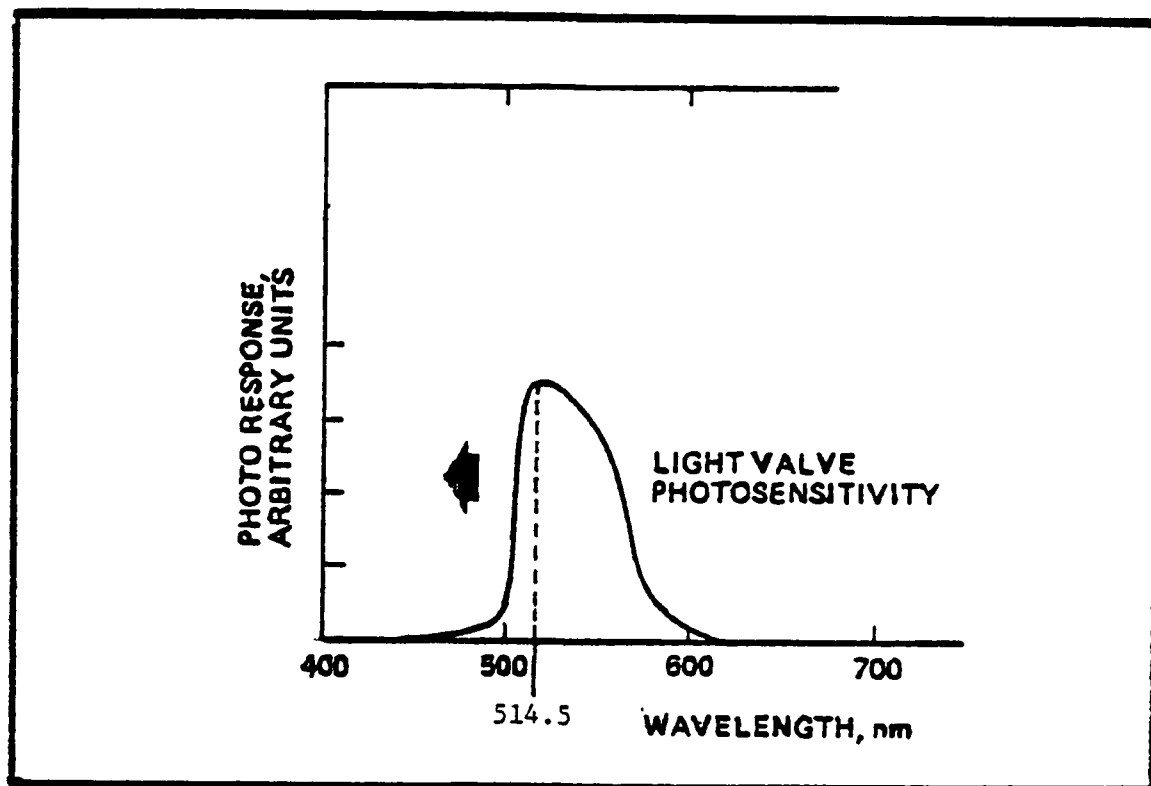


Fig. 25. LCLV Photo Response Characteristics (Ref. 21:88).

ion laser ($\lambda = 514.5$ nm) is the best optical source for an optimum response. Note from Fig. 25 that a He-Ne laser ($\lambda = 633$ nm) would severely constrain LCLV performance. Also recall that problems were encountered in OAF when the He-Ne laser was used for the optical source.

To verify that the LCLV was operating properly, the architecture of Fig. 26 was constructed. The optical architecture, in part, resembles those used for the optical excisors just discussed. Most of the setup is therefore self-explanatory. The LCLV is the only new element in this architecture. An explanation for the role of the LCLV and the propagation of the light beam downstream from the LCLV is in order.

Observe that the Fourier transform of the light entering BC appears at the input side of the LCLV. The LCLV input side is known as the write side because the information, in the form of light intensity,

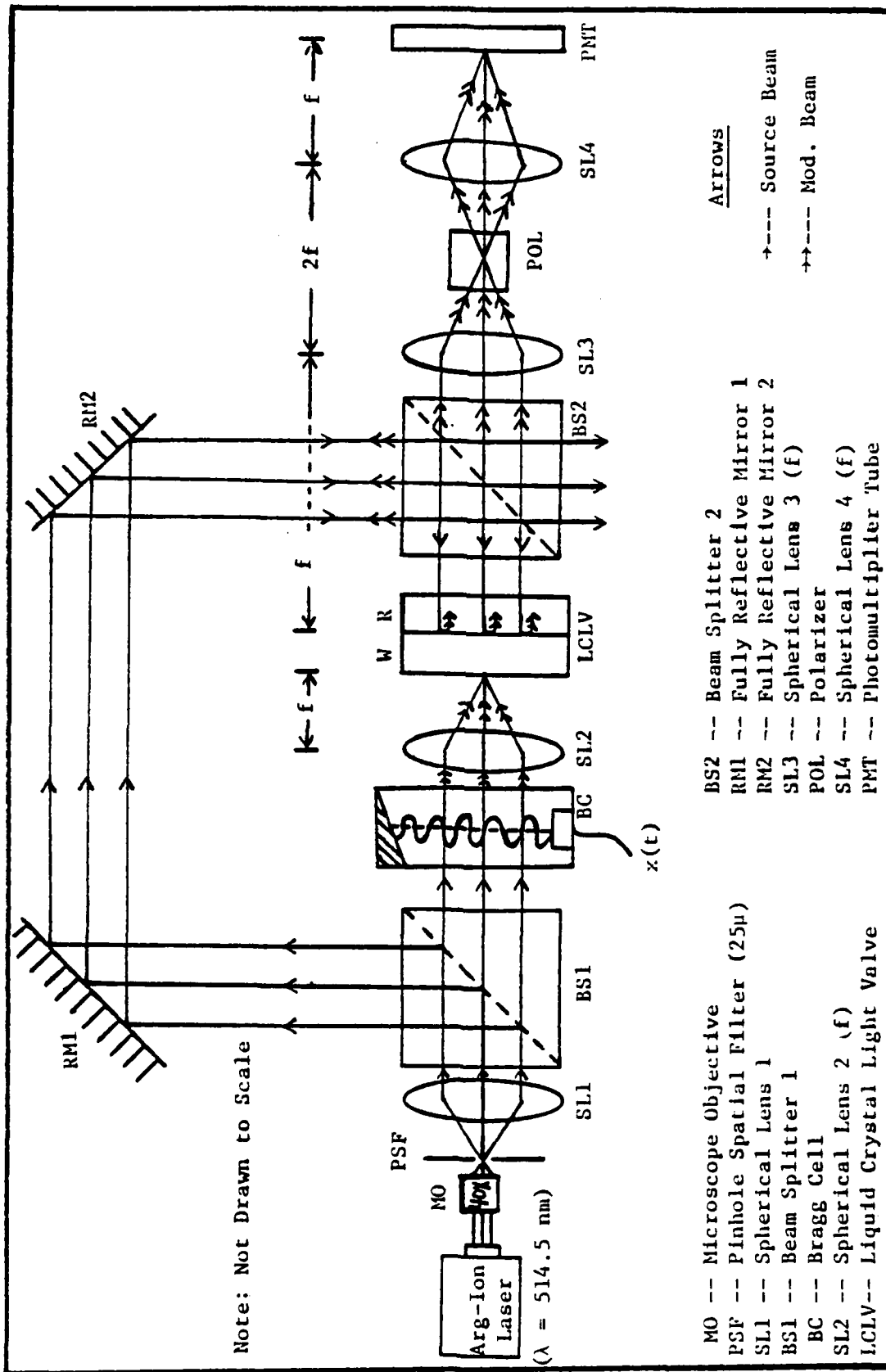


Fig. 26. Liquid Crystal Light Valve Test.

impinges upon the surface and can only be processed one-way through the LCLV (Appendix B).

Hence, the output side cannot be used as an input side. The output side of the LCLV is known as the read side because the processed information is obtained by using a polarized optical beam (read beam) whose polarization, after being reflected from the output surface of the LCLV, is rotated through an angle approximately proportional to the averaged squared modulus of the input light amplitude. It should be noted that the output unmodulated optical beam of the Arg-ion laser is polarized vertically.

The required read beam is provided by the beam splitter BS2 and the fully reflective mirrors RM1 and RM2. Once the read beam is reflected from the LCLV, BS2 directs the modulated read beam downstream for imaging. Note again that one-half of the intensity of the reflected read beam is lost. Therefore, by the time the modulated read beam arrives at spherical lens SL3, only one-eighth of the original source intensity remains.

Spherical lenses SL3 and SL4 (focal lengths f) image the polarized intensity light distributions (obtained by the read beam) to the PMT. The polarizer POL is used as an analyzer to obtain only the information contributed by $|X(\omega) e^{j\omega t}|^2$ on the write side of the LCLV. See Appendix B for details. Note that POL is placed where the entire beam is small enough to pass through the POL. Finally, the photomultiplier tube PMT detects the processed signal $|X(\omega)|^2$.

Observations

The PMT was included in the original LCLV test design (Fig. 26);

however, in the actual testing, a white index card was substituted in order to observe the results of rotating polarizer POL. In fact, the results of rotating POL were the most important observations made during the LCLV test.

By rotating POL, one could choose to maximize either the intensity distribution of $|X(\omega)|^2$ (Fig. 27) or the intensity due to the "ambient

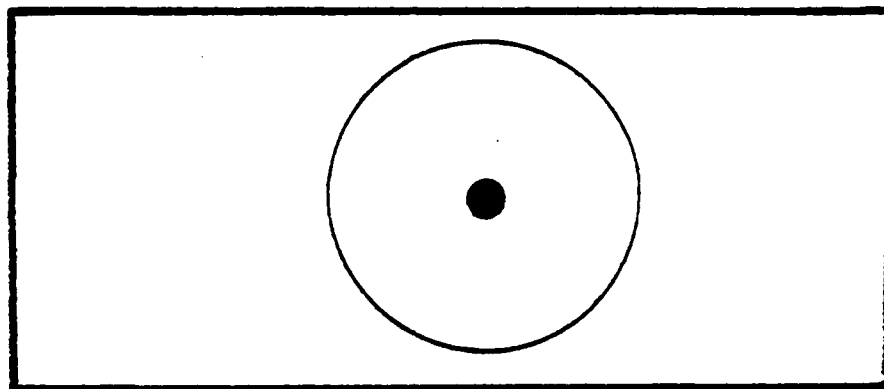


Fig. 27. Maximized Intensity of $|X(\omega)|^2$ by Polarizer POL.

state" of the LCLV (Fig. 28). The explanation for this observation is

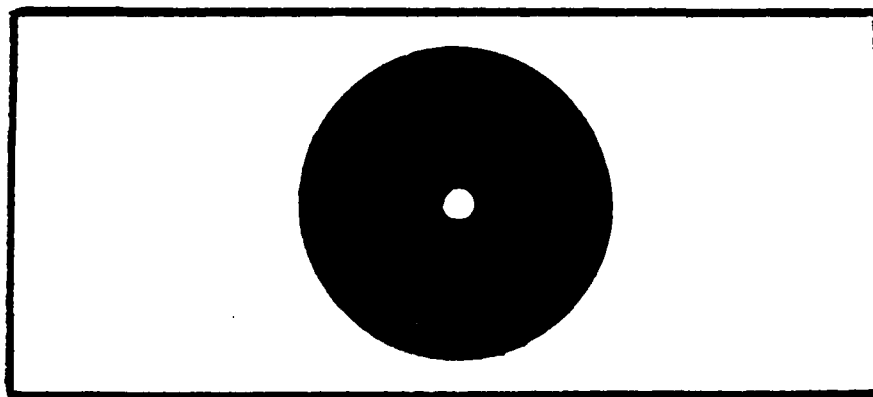


Fig. 28. Maximized Intensity of LCLV "Ambient State" by Polarizer POL.

based upon the fact that the ambient state of the LCLV maintains a sort of "dark rotation" which is polarized at some angle α and the light

possessing the intensity distribution of $|X(\omega)|^2$ is rotated by an additional angle δ , via an intensity to polarization transformation (Appendix B). Therefore, the polarizer POL can maximize the intensity due to the ambient state by being aligned with the light polarized at angle α . On the other hand, the polarizer POL can maximize the intensity distribution due to $|X(\omega)|^2$ by being aligned with the light polarized at angle $(\alpha + \delta)$.

The LCLV test was very successful in that the principles of the LCLV and the POL were thoroughly examined and understood. Moreover, now that the LCLV operation has been verified; the optical principles required by OAFFI have been successfully demonstrated.

In summary then, the three basic optical architectures on which OAFFI principles are based were successfully implemented and tested. The Optical Spectrum Analyzer demonstrated the fundamental OSP principles of frequency analysis in the Fourier transform plane. Also, the diffraction property of Bragg cells was observed. In the Optical Excisor Version I, the principles of heterodyning with an interferometric optical architecture were revealed. With an interferometric architecture, the optical alignment of the equipment is crucial to achieving optimum performance. In the Optical Excisor Version II, a simpler optical architecture was gained by removing all cylindrical lenses. However, the ability to resolve multiple frequencies was forfeited when cylindrical lens CL3 was eliminated from the architecture. In the LCLV test, the optical-to-optical transducer property of the LCLV was verified. By rotating polarizer POL, a maximum

transfer of information can be obtained from the LCLV polarized output read beam.

The first approach to OAFFI will include a Mach-Zehnder interferometer (MZI). Furthermore, since the LCLV is required, the Arg-ion laser will be used throughout the remaining architecture of this report.

Because of the inherent danger of eye injury due to direct exposure to the Arg-ion beam, the He-Ne laser was used in earlier architectures where the LCLV was not required. This permitted the "novice" student sufficient time to become familiar with laser precautions. As a result, the student survived the 1 - 5 watt range of the Arg-ion laser by experimenting first with the 1 - 3 milliwatt range of the He-Ne laser. The word "survived" indicates that no injuries were incurred.

OAFFI (MZI)

Theory

By combining the principles demonstrated in the previous architectures, the optical architecture of Fig. 29 was constructed to test the feasibility of the Optical Adaptive Filter: Frequency Domain Implementation (OAFFI). The OAFFI was designed and tested in two versions. In each version, an interferometer was used as part of the design. In the first version, a Mach-Zehnder interferometer was used, whereas in the second version, a common path interferometer was used. The two versions will thus be called the MZI version and the CPI version, respectively, of the OAFFI.

OAFFI(MZI) proved to be a challenge to achieve proper optical

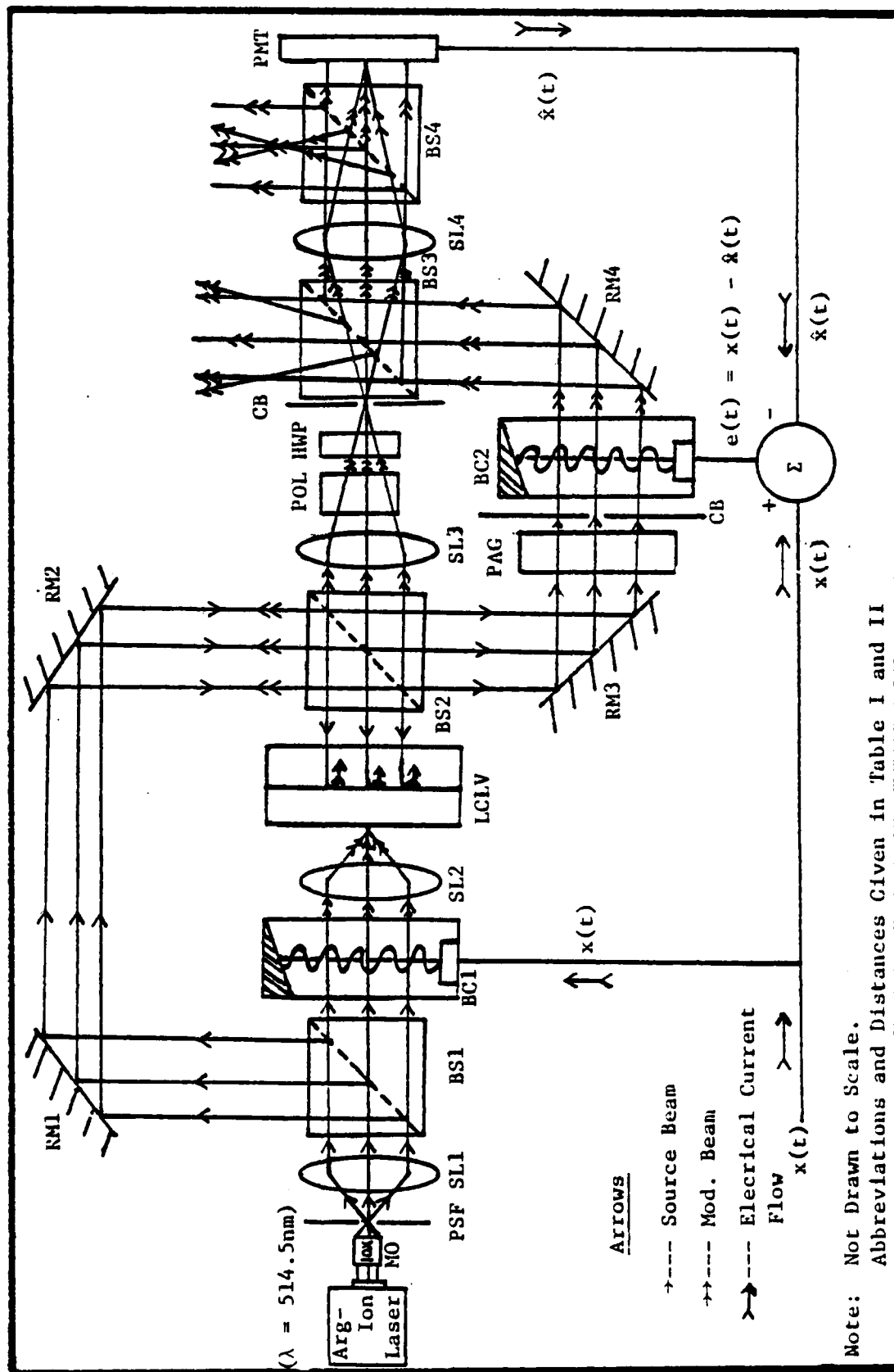


Fig. 29. OAFFI Implemented with Mach-Zehnder Interferometer.

alignment of the equipment. Two index cards with pinholes, which were placed at the center of the optical beam, were used to align the optical beams in order to achieve interference of the two beams (one from LCLV and one from BC2) at photomultiplier PMT. Both cards were placed at beam splitter BS2 (one for the LCLV read beam and one for the "source" beam headed to BC2). After adjusting fully reflective mirrors RM3 and RM4 and beam splitter BS3 with beam splitter BS4 absent, the two optical beams (spots) were coincident at PMT. Interference fringes were observed on a white index card placed in front of the PMT.

Before explaining the architecture of Fig. 29, a definition of abbreviations (Table I) and a statement of distances (Table II) is in order. Again, the optical beam source is a Spectra-Physics Model 164 Argon-ion laser ($\lambda = 514.5 \text{ nm}$). Microscope objective MO (10X power) focuses the Arg-ion laser beam through pinhole spatial filter PSF, having a diameter of 25 microns.

Note that MO has been switched from a 40X power to a 10X power. The reason for the change is to create a smaller optical beam for processing. The 10X power objective has a slightly longer focal length (Fig. 30) than the 40X power focal length, which facilitates the placement of a smaller beam through the center portion of SL1. The smaller beam lessens the amount of distortion induced by the edges of the lens. Since the optical architecture of Fig. 29 is elaborate, distortions need to be kept at a minimum to stifle their increasing effect downstream.

A filtered optical beam exits PSF. Spherical lens SL1 collimates the expanding optical beam. Beam splitter BS1 separates the source beam

Table I

Abbreviations Used in Fig. 29

Abbrev.	Definition
MO	Microscope Objective (10X)
PSF	Pinhole Spatial Filter (25)
SL1	Spherical Lens 1
BS1	Beam Splitter 1
RM1	Fully Reflective Mirror 1
RM2	Fully Reflective Mirror 2
BC1	Bragg Cell 1 (70 MHZ CF, 40 MHZ BW)
SL2	Spherical Lens 2 (focal length f)
LCLV	Liquid Crystal Light Valve
BS2	Beam Splitter 2
RM3	Fully Reflective Mirror 3
PAG	Phase Adjusting Glass
CB	Cardboard
BC2	Bragg Cell 2 (70 MHZ CF, 40 MHZ BW)
RM4	Fully Reflective Mirror 4
SL3	Spherical Lens 3 (focal length f)
POL	Polarizer (analyzer)
HWP	Half-Wave Plate
BS3	Beam Splitter 3
SL4	Spherical Lens 4 (focal length f)
BS4	Beam Splitter 4
PMT	Photomultiplier Tube

Table II

Distances Between Devices in Fig. 29

From	To	Distance (cm)
Arg-ion Laser	MO	24.45
MO	PSF	0.64
PSF	SL1	13.34
SL1	BS1	5.72
BS1	RM1	5.72
RM1	RM2	55.88
RM2	BS2	12.70
BS1	BC1	13.97
BC1	SL2	8.26
SL2	LCLV	22.86
LCLV	BS2	10.80
BS2	RM3	11.43
RM3	PAG	11.43
PAG	CB	8.89
CB	BC2	17.78
BC2	RM4	7.62
RM4	BS3	10.80
BS2	SL3	8.26
SL3	POL	19.05
POL	HWP	5.72
HWP	CB	2.54
CB	BS3	8.26
BS3	SL4	7.30
SL4	BS4	11.43
BS4	PMT	10.48

Note: All distances were "coarsely" measured from/to the center of each device in inches prior to conversion to centimeters.

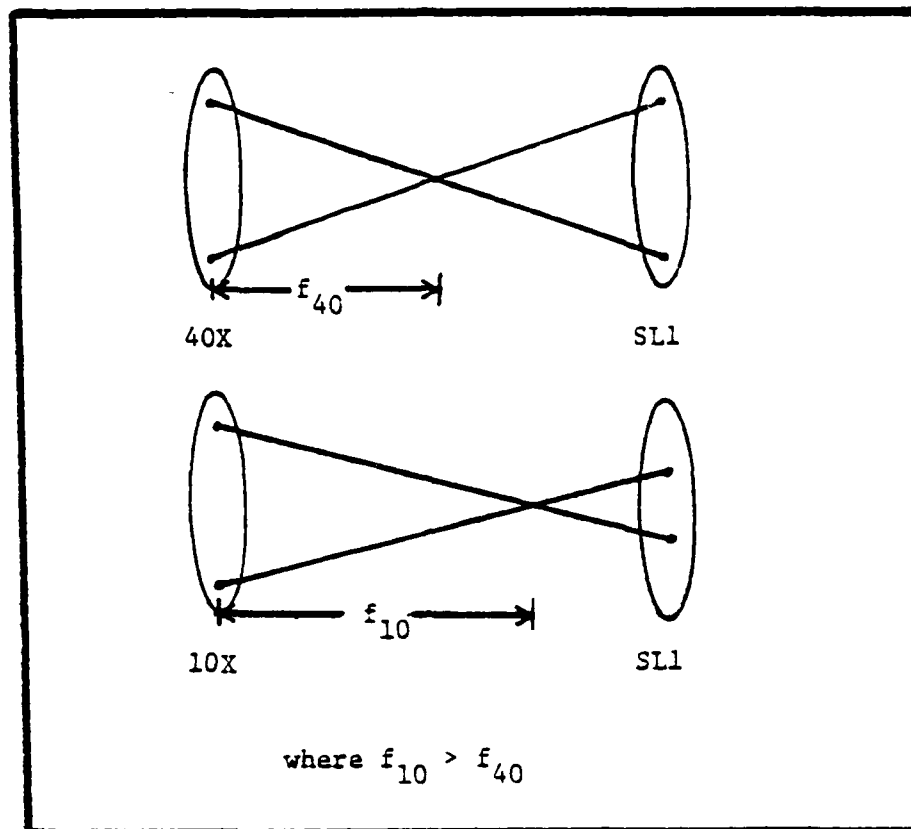


Fig. 30. Comparison of Microscope Objectives (40X vs. 10X).

into two components having equal intensity, which is equal to one-half the intensity of the source beam. The two components consists of a "source" beam which becomes the LCLV input (write) beam and a "source" beam which becomes the LCLV output (read) beam. Reductions in source beam intensity will be annotated by the addition of " ", _____, () and (()) to the word "source".

In the straight-through path, Bragg cell BC1 (70 MHZ CF, 40 MHZ BW) amplitude modulates the optical beam via an acoustic replica of $x(t)$. Spherical lens SL2 (focal length f) performs a FT on the input light distribution which is provided by the AO modulated beam. The FT appears at the input side of the LCLV. All spots are blocked except the first-

order diffracted spot. Hence, $X(\omega) e^{j\omega t}$ is incident on the write side of the LCLV. The LCLV (square law device) processes the information and produces $|X(\omega)|^2$ to be scanned by the read beam at the output (See Appendix B for details).

Whereas, the read beam originates as one of the "source" beams at BS1. After being directed by fully reflective mirrors RM1 and RM2, it arrives at BS2. Beam splitter BS2 separates the "source" beam into two components having equal intensity, which is equal to one-half the intensity of the "source" beam. The two components consist of a "source" beam which becomes the LCLV read beam and a "source" beam which is AO modulated by Bragg cell BC2.

In the straight-through path, BS2 again separates the read beam (reflecting from LCLV) into two components having equal intensity, which is equal to one-half the intensity of the "source" beam. The two components consist of a ("source") beam which is directed back toward the source via RM2, RM1, BS1 and SL1 and a ("source") beam which is directed downstream as the read beam for imaging. Note that the read beam contains; not only information $|X(\omega)|^2$ at some polarization angle $(\alpha + \delta)$, but also biasing (ambient state) information at some polarization angle α .

Spherical lens SL3 and SL4 (focal lengths f) image the polarized intensity spot (obtained by the read beam) to the PMT. Polarizer POL is used as an analyzer to obtain from the read beam, only the information contributed by $|X(\omega)|^2$. Therefore, it passes information at angle $(\alpha + \delta)$ while blocking information at angle α .

Now that the information $|X(\omega)|^2$ is obtained; it still is polarized

AD-A141 090

OPTICAL ADAPTIVE FILTER FREQUENCY DOMAIN IMPLEMENTATION 2/3

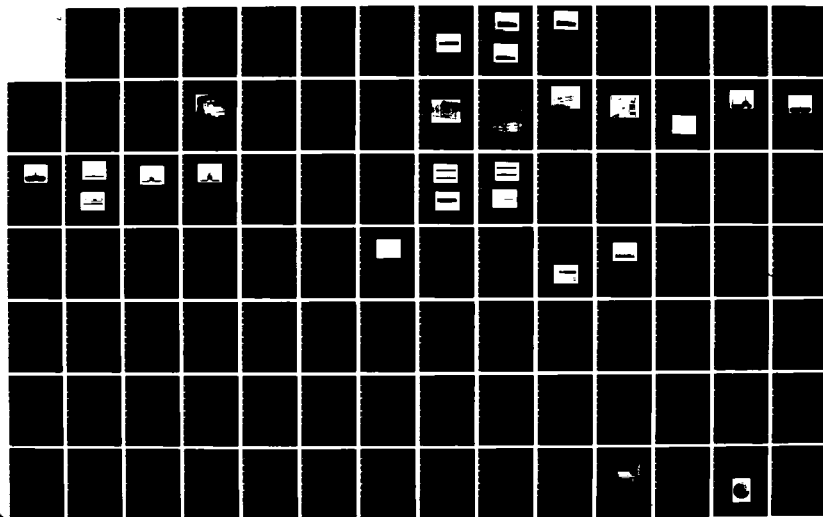
(U) AIR FORCE INST OF TECH WRIGHT-PATTERSON AFB OH
SCHOOL OF ENGINEERING J L NEWMAN DEC 83

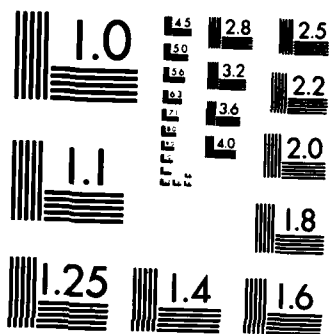
UNCLASSIFIED

AFIT/GE/EE/83D-51

F/G 20/6

NL





MICROCOPY RESOLUTION TEST CHART
NATIONAL BUREAU OF STANDARDS-1963-A

at an angle of $(\alpha + \delta)$; while the ("source") beam being modulated by BC2 is polarized at some initial angle β . In order to have maximum interference at the PMT, these two optical beams (spots) need to possess the same polarization in addition to being coincident (one-on-one).

By rotating half-wave ($\lambda/2$) plate HWP, the polarization of the read beam can be rotated to match the polarization of the ("source") beam; i.e. angle $(\alpha + \delta)$ becomes angle β . Note that HWP can be placed in either optical path; however, HWP was placed between SL3 and SL4 because the read beam was small enough to pass through HWP.

White index cards CB were used to reduce the intensity of both the read beam and the BC2 modulated ("source") beam at the PMT. The partial blocking of the beams with CB demonstrated an increased SNR in the detector output. This will be further discussed in the "Observations" section.

Fully reflective mirror RM3 directs the ("source") beam from BS2 to phase adjusting glass PAG. In order for OAFFI(MZI) to perform the summation of $e(t) = x(t) - \hat{x}(t)$; the sinusoidal RF signal $x(t)$ and the sinusoidal optical signal $\hat{x}(t)$ must be 180 degrees out of phase. By rotating PAG, horizontal to the optical path, the path length for the BC2 modulated ("source") beam could be varied; which equates to changing the phase of $\hat{x}(t)$. Therefore, PAG provided a means to easily adjust the phase of $\hat{x}(t)$ described by Eq.(51), repeated here for convenience.

$$\hat{x}(t) = 2 \int E(\omega) |X(\omega)|^2 e^{j\omega t} d\omega$$

Furthermore, Bragg cell BC2 amplitude modulates the optical

("source") beam via an acoustic replica of the error signal $e(t)$. The AO processing accomplished by BC2 is the chief cornerstone of OAFFI(MZI). Specifically, $e(t)$ provides the adaptive weighting at the PMT when its Doppler shifted Fourier transform, $E(\omega) e^{j\omega t}$, interferes with $|X(\omega)|^2$ as required by Eq. (51).

Fully reflective mirror RM4 directs the BC2 modulated ("source") beam to beam splitter BS3. BS3 recombines the read beam and the BC2 modulated ("source") beam, which were separated by BS2. Once again, each of the two approaching beams loses half of its intensity at BS3. Since both beams have the intensity of a ("source") beam prior to rejoining at BS3; the resulting beam that exits BS3 for spherical lens SL4 also has the intensity of a ("source") beam.

In addition to its role in imaging $|X(\omega)|^2$ onto the PMT as described by L2 in Fig. 10; SL4 performs a FT on the input light distribution which is provided by the BC2 modulated beam. Thus, the Doppler shifted FT of $e(t)$ appears at the PMT.

Beam splitter BS4 is used primarily to further reduce the intensity of the ("source") beam to produce the ((("source"))) beam which arrives at the PMT. This keeps the PMT from going into saturation. This final reduction in intensity produces an optical beam (spot) which has one-sixteenth of the original intensity of the source beam. Recall that reductions in source beam intensity have been annotated by the addition of " ", _____, () and (()) to the word "source".

A secondary use of BS4 is that one path of the output spectrum, which includes the DC spot, two first-order spots and one second-order spot, could be viewed on cardboard while its orthogonal equivalent path

was being processed by the PMT. This secondary use proved to be very beneficial when the architecture required realignment; i.e. the output spectrum could be viewed while the PMT remained stationary.

Finally, the PMT performs an integration on the processed signals $|X(\omega)|^2$ and $E(\omega) e^{j\omega t}$ as described by Eq. (51). The first-order diffracted distribution (or diffracted spot for a single frequency) from BC1, which has been imaged from the LCLV to the PMT, provides the $|X(\omega)|^2$ distribution and the first-order diffracted distribution from BC2 provides the $E(\omega) e^{j\omega t}$ distribution. Note that "2" is just a constant of integration. Interference occurs between these two distributions as shown in Fig. 31. The DC spot is blocked by a zero-

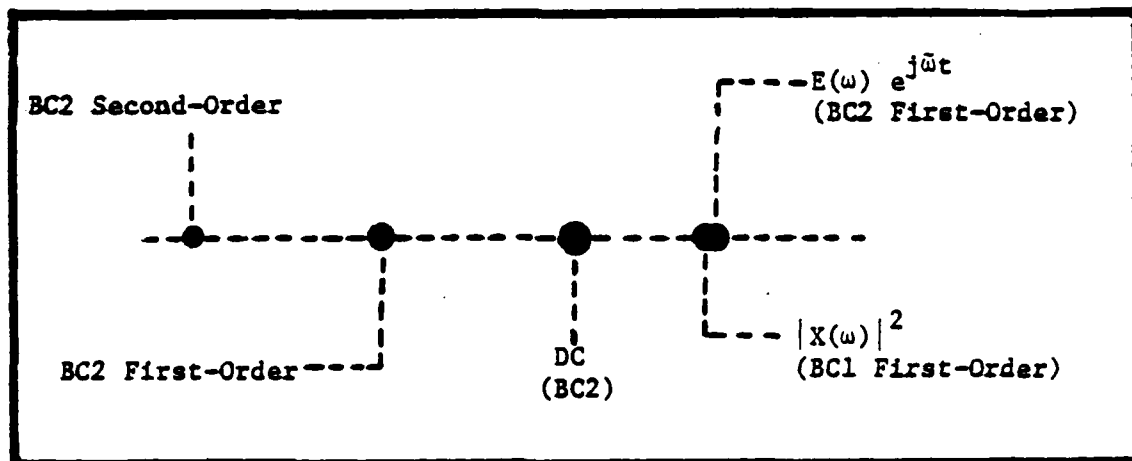


Fig. 31. Output Spectrum of OAFFI(MZI)

order stop at the PMT. The first-order and second-order distributions on the LHS of Fig. 31 are neglected due to their low intensity and lack of interference with other distributions (signals).

Now that $\hat{x}(t)$ has been optically detected, the summer performs the following operation: $e(t) = x(t) - \hat{x}(t)$. Note again that PAG is rotated to keep the sinusoidal optical signal $\hat{x}(t)$ 180 degrees out of

phase with the sinusoidal RF signal $x(t)$. Thus, PAG governs the optical path length which directly corresponds to controlling the phase of $\hat{x}(t)$.

Observations

As mentioned in the Optical Excisor Version II, adjusting cardboard CB increased the SNR at the output (PMT). By blocking portions of both component beams in the MZI arrangement of Fig. 29, an improved SNR was observed. However, as a result of changing to an opaque optical stop, it was discovered that scattered light from the white cardboard CB (being slightly translucent) contributed 3dB SNR at the PMT output. This would introduce misleading information about the performance of the system. Therefore, all optical stops were made opaque.

Possibly the most important observation from an analysis standpoint was the phase stability problem. Historically, the Mach-Zehnder interferometer has been very sensitive to external disturbances; especially if these disturbances affect each of the two paths differently (Ref. 7:174). The most common external disturbances to optical beams are air currents in a well ventilated room and vibrations from operating machinery in other parts of the building.

To combat the problem of air currents, the entire OAFFI(MZI) architecture was enclosed on six sides. Since the optical table had an overhead storage area, a barrier was provided for the top and bottom. Cardboard provided the barrier for the back side of the setup. The remaining three sides were enclosed by a black opaque curtain. To combat the problem of vibrations, air supports were used to "float" the

table. Thus, the floating table should have been insensitive to floor vibrations.

In spite of attempts to eliminate these external disturbances via black opaque curtains and an air-supported optical table, air currents and vibrations still caused the phase of $\hat{x}(t)$ to drift sporadically. By fanning the optical beam or pounding on the optical table or even closing a nearby door, extreme phase fluctuations were observed in $\hat{x}(t)$. On the average, ambient phase fluctuations were approximated from the oscilloscope to be 2.9 nsecs out of a period of 14.29 nsecs or 73.1 degrees. An attempt was made to manually compensate for the phase drift by rotating PAG. This proved to be unrewarding. Therefore, manual correction of the phase drift was not feasible which further emphasizes the randomness of the phase fluctuations.

Another observation included the mysterious appearance of an optical signal at 72.5 MHZ (Photo 11). Since the RF input to both Bragg cells was 70 MHZ, the source of the 72.5 MHZ optical signal still remains a mystery.

Once again, RFI was observed in the output of the PMT when the optical beam was blocked (Photo 13). This problem was previously mentioned in the "Observations" section of the Optical Excisor Version II. In OAFFI(MZI), RFI varied from 6 to 34 dB above the noise floor of the spectrum analyzer, depending on the placement of coaxial cables, location of the experimenter and other undetermined phenomenon. A detailed analysis on RFI will be discussed in a later section (page 149).

The remaining observations have been recorded on film. For the following photos, the RF input $x(t)$ to BC 1 was a 70 MHZ sine wave.

Both Bragg cells BC1 and BC2 have a CF of 70 MHz and a BW of 40 MHz. See Appendix A for specific details on these Bragg cells. Also, the PMT was used for the PD. A 70 MHz filter (20 MHz BW) was used in some architectures and not in others. Therefore, "w/o Filter" indicates that the 70 MHz filter was not used.

To test the optical architecture of OAFFI(MZI) for proper alignment, a 70 MHz RF sinusoidal signal was simultaneously input to BC1 and BC2. This was an open-loop configuration (no feedback). Photos 10 - 13 display the resulting output of the PMT.

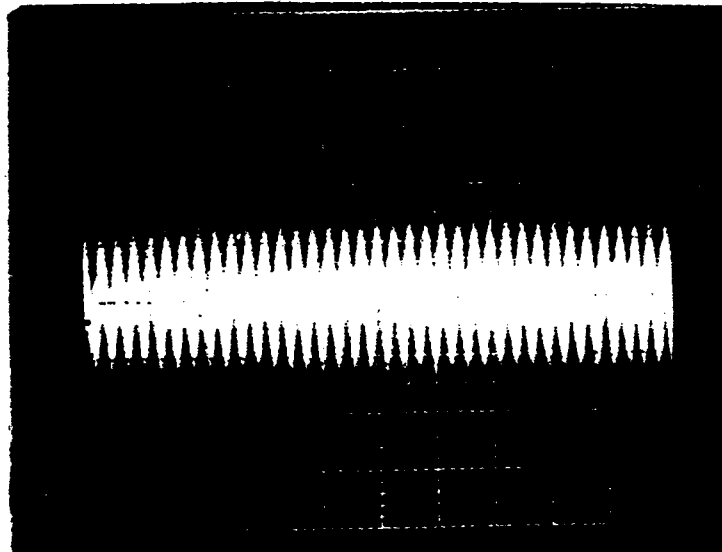


Photo 10. 70 MHz Optical Signal w/o Filter.
Vert. = 0.5 Volts/Div. (1.5 Volts P-P)
Hor. = .05 μ sec/Div. (1 Div. = 3.5T)

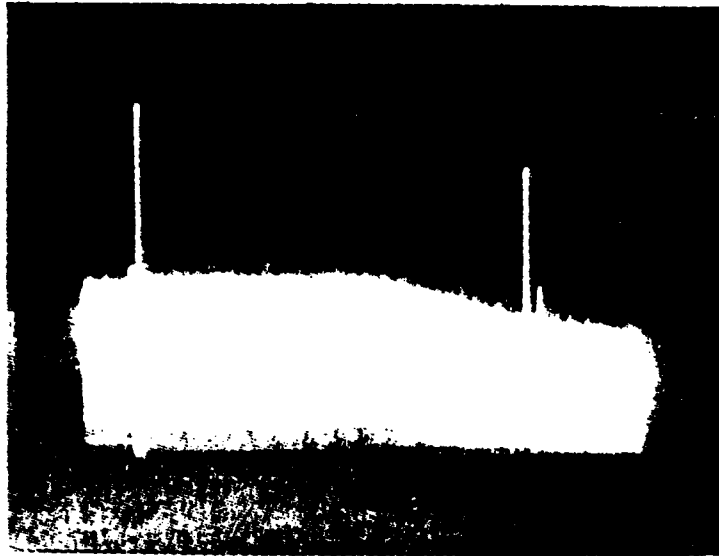


Photo 11. Spectrum of PMT Output for Photo 10.
Scan Width = 10 MHz/Div.
DC = 32 dB SNR, 70 MHz = 30 dB SNR
72.5 MHz = 10 dB SNR

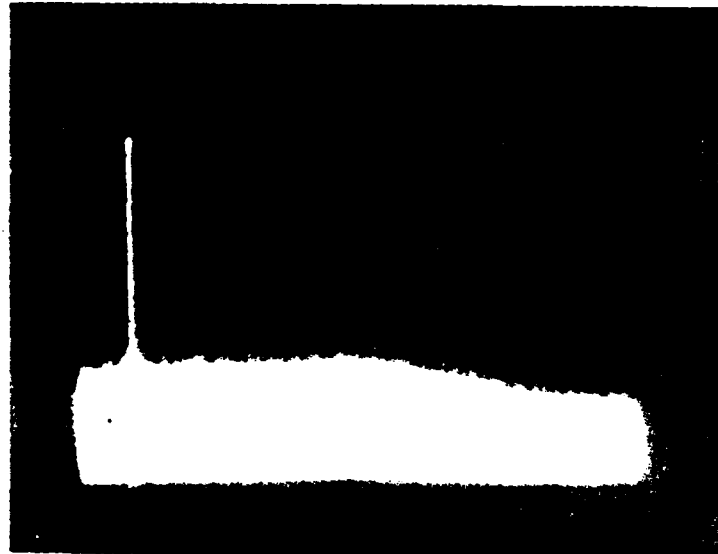


Photo 12. Spectrum of PMT Output w/o Filter and with
Optical Signal Blocked from BC2 Path of MZI.
Noise Floor Decreased from Photo 11.



Photo 13. Spectrum of PMT Output w/o Filter and with Optical Signal Blocked from LCLV. Possibly, 70 MHZ Signal Results from Heterodyning of Unmodulated Read Beam and BC2 Modulated Beam or RFI.

usions

OAFFI(MZI) encountered three significant problems: output phase stability, a mysterious optical signal at 72.5 MHZ and RFI at 70 MHZ. The most significant of these problems is the output phase instability. Perhaps the mysterious 72.5 MHZ optical signal resulted from scattered light. This could generate an extra frequency component caused by the scattered light arriving at a slightly different angle than the Bragg angle. Since there is some tolerance observed in practical applications of the Bragg angle relationship given by Eq. (36), repeated below for convenience,

$$\theta_B = \sin^{-1}\left(\frac{\lambda}{2\Lambda}\right)$$

this explanation seems plausible. Hence, this problem appears to be

solvable by employing high quality optical equipment and by blocking all unnecessary light at each optical device.

Moreover, the RFI problem originates at the RF signal generator for $x(t)$. The PD acts like an antenna in that it picks up RF. Numerous attempts were unsuccessful in eliminating the RFI problem (see RFI page 149). However, since the source is known, the problem appears to be solvable by employing high quality equipment (e.g. a signal generator, amplifiers, coaxial cables and a PD).

Nevertheless, even if the 72.5 MHZ optical signal and the 70 MHZ RFI could be eliminated, the biggest obstacle, that of the phase instability remains. The output phase stability is crucial to the successful operation of OAFFI(MZI). The summation of $e(t) = x(t) - \hat{x}(t)$ requires a constant 180 degrees phase difference between $x(t)$ and $\hat{x}(t)$. This is not possible if $\hat{x}(t)$ experiences phase fluctuations.

The source of the output phase fluctuations was identified as air currents and vibrations. To solve this problem, an isolated immobile vacuum would be required, or somehow, each optical path could be made to experience identical perturbations. Perhaps this could be accomplished through a feedback system for sensing air currents and vibrations.

Since the feasibility of these modifications to solve the phase stability problem is questionable, OAFFI(MZI) is an unacceptable architecture. Therefore, no valuable data was obtained from OAFFI(MZI) other than that demonstrating its unacceptable performance.

A second optical architecture for OAFFI will be discussed next. It employs a common path interferometer (CPI). OAFFI(CPI) overcame the phase stability problem encountered by OAFFI(MZI).

OAFFI(CPI)

Theory

Due to the phase stability problems demonstrated by OAFFI(MZI), a common path interferometer architecture was sought and achieved. Recall in OAFFI(MZI), phase fluctuations resulted in the output because it was conjectured that the two optical paths were affected differently by external disturbances (air currents and vibrations). With a common path interferometer (see Refs. 3, 4, and 14), all disturbances will affect each optical path the same. Hence, no phase difference fluctuations should result.

The optical architecture of Fig. 32 was constructed to test the feasibility of OAFFI using a common path interferometer, which will be designated OAFFI(CPI). Before explaining the architecture of Fig. 32, a definition of abbreviations (Table III) and a statement of distances (Table IV) is in order.

The optical beam source is still a Spectra-Physics Model 164 Argon-ion laser ($\lambda = 514.5$ nm). Microscope objective MO (10X power) focuses the Arg-ion laser beam through pinhole spatial filter PSF, having a diameter of 25 microns. A filtered optical beam exits PSF. Spherical lens SL1 collimates the expanding optical beam.

Beam splitter BS1 separates the source beam into two components having equal intensity, which is equal to one-half the intensity of the source beam. The two components consist of a "source" beam which becomes the LCLV input (write) beam and a "source" beam which becomes the LCLV output (read) beam. Reductions in source beam intensity will

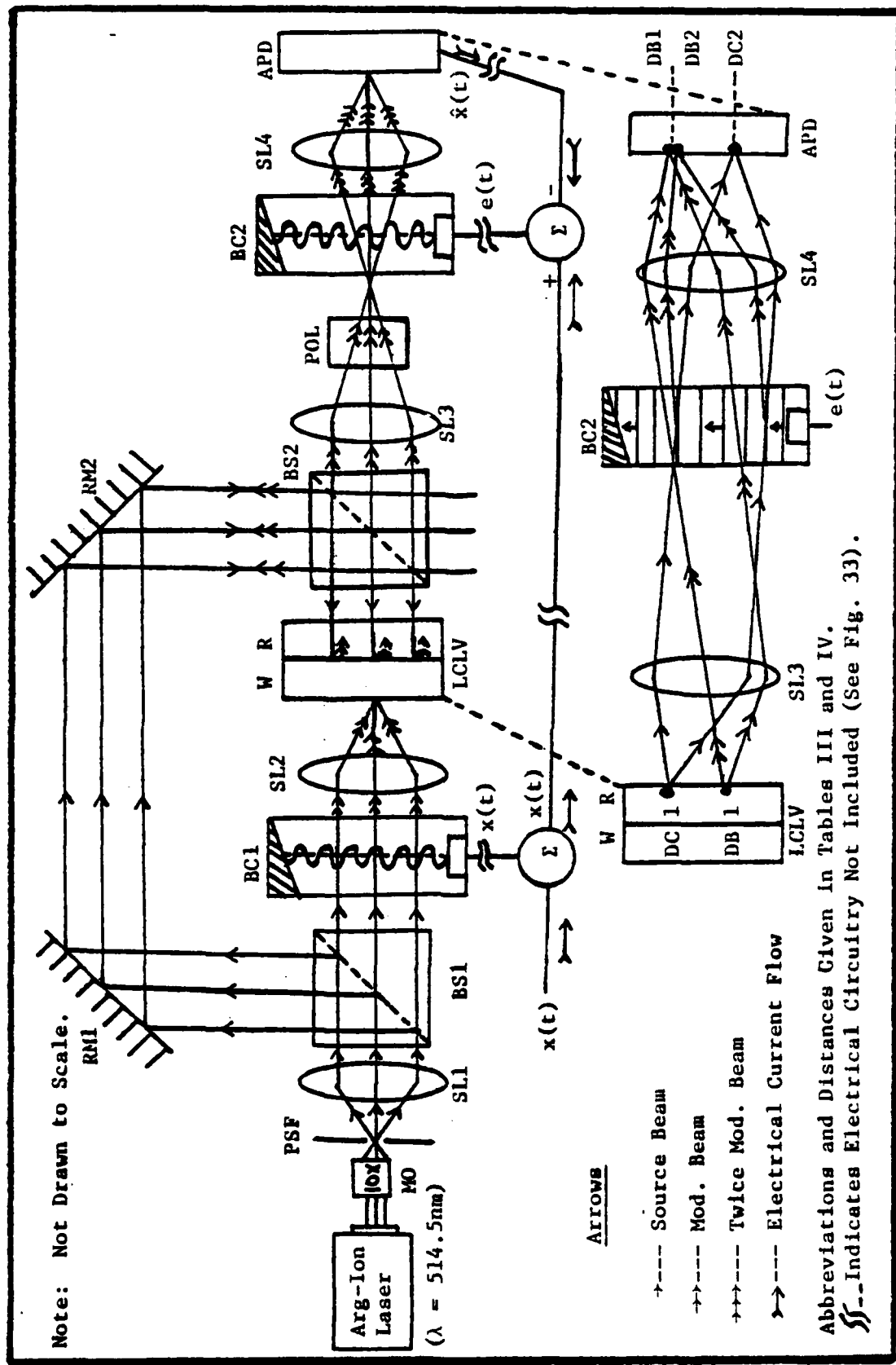


Fig. 32. OAFFI Implemented with Common Path Interferometer.

Table III

Abbreviations Used in Fig. 32

Abbrev.	Definition
MO	Microscope Objective (10X)
PSF	Pinhole Spatial Filter (25 μ)
SL1	Spherical Lens 1
BS1	Beam Splitter 1
RM1	Fully Reflective Mirror 1
RM2	Fully Reflective Mirror 2
BC1	Bragg Cell 1 (70 MHZ CF, 40 MHZ BW)
SL2	Spherical Lens 2 (focal length f)
LCLV	Liquid Crystal Light Valve
BS2	Beam Splitter 2
SL3	Spherical Lens 3 (focal length f)
POL	Polarizer (analyzer)
BC2	Bragg Cell 2 (70 MHZ CF, 40 MHZ BW)
SL4	Spherical Lens 4 (focal length f)
APD	Avalanche Photo-Diode
DB1	Diffracted Beam from BC1
DB2	Diffracted Beam from BC2
DC1	Straight-Through Beam from BC1
DC2	Straight-Through Beam from BC2

Table IV

Distances Between Devices in Fig. 32

From	To	Distance (cm)
Arg-Ion Laser	MO	23.50
MO	PSF	1.27
PSF	SL1	13.97
SL1	BS1	6.35
BS1	RM1	6.35
RM1	RM2	57.15
RM2	BS2	13.34
BS1	BC1	9.84
BC1	SL2	10.16
SL2	LCLV	19.05
LCLV	BS2	14.61
BS2	SL3	9.53
SL3	POL	8.26
POL	BC2	15.24
BC2	SL4	20.32
SL4	APD	19.69

Note: All distances were "coarsely" measured from/to the center of each device in inches prior to conversion to centimeters.

be annotated by the addition of " ", _____, () and (()) to the word "source".

In the straight-through path, Bragg cell BC1 (70 MHz CF, 40 MHz BW) amplitude modulates the optical beam via an acoustic replica of $x(t)$. Spherical lens SL2 (focal length f) performs a FT on the input light distribution which is provided by the AO modulated beam. The FT appears at the input side of the LCLV. All spots/distributions are blocked except for the DC spot and the first-order diffracted distribution. Note that "spot" designates a single frequency whereas "distribution" designates multiple frequencies. In this thesis, only a single frequency was used; however, OAFFI will eventually be expected to cover many frequencies, simultaneously. Therefore, the two terms are sometimes interchanged for discussion purposes. Hence, $X(\omega) e^{-j\omega t}$ (first-order distribution) and the DC spot are incident on the write side of the LCLV. The LCLV (square law device) processes the information and produces $|X(\omega)|^2$ and the DC spot to modulate the read beam at the output (see Appendix B for details).

The read beam originates as one of the "source" beams at BS1. After being directed by fully reflective mirrors RM1 and RM2, it arrives at BS2. Beam splitter BS2 separates the "source" beam into two components having equal intensity, which is equal to one-half the intensity of the "source" beam. The two components consist of a "source" beam which becomes the LCLV read beam and a "source" beam which is lost.

The read beam is polarization modulated by the information on the LCLV and is reflected back to BS2. The beam splitter BS2 again

separates the read beam into two components having equal intensity, which is equal to one-half the intensity of the "source" beam. The two components consist of a ("source") beam which is directed back toward the source via RM2, RM1, BS1 and SL1 and a ("source") beam which is directed down stream as the read beam for imaging and further processing. The read beam contains information on the first-order diffracted distribution ($|X(\omega)|^2$) and the DC spot. Recall that this information is polarized at some angle ($\alpha + \delta$). Also, included in the read beam, is biasing (ambient state) information at some polarization angle δ .

Spherical lens SL3 and SL4 (focal lengths f) image the polarized intensity distributions (obtained by the read beam) to the avalanche photo-diode APD. Polarizer POL is used as an analyzer to obtain from the read beam only the information contributed by $|X(\omega)|^2$ and the DC spot. Therefore, it passes information at angle ($\alpha + \delta$) while blocking information at angle α . Since a common path interferometer is used, the HWP of OAFFI(MZI) is not necessary.

As depicted in the expanded portion of Fig. 32 (BS2 and POL omitted for simplicity), the first-order diffracted spot of BC1 (DB1) and the DC spot of BC1 (DC1) enter BC2 for additional processing. The distribution from DB1 passes straight through BC2 without being further AO modulated. Whereas, DC1 is amplitude modulated by BC2 (70 MHZ CF, 40 MHZ BW) via an acoustic replica of $e(t)$. Moreover, DC1 separates into two component beams, the straight-through beam DC2 and the first-order diffracted beam DB2. Thus, the interference of DB1 and DB2 occurs at the APD.

Finally, the APD detects the processed signals $|X(\omega)|^2$ from DB1 and $E(\omega) e^{j\omega t}$ from DB2 as described by Eq. (51).

Note that the APD has been used instead of the PMT. Initially, the PMT was used for photo-detection in OAFFI(CPI). But another attempt was made to solve the RFI problem by switching to the APD (Photo 14). The

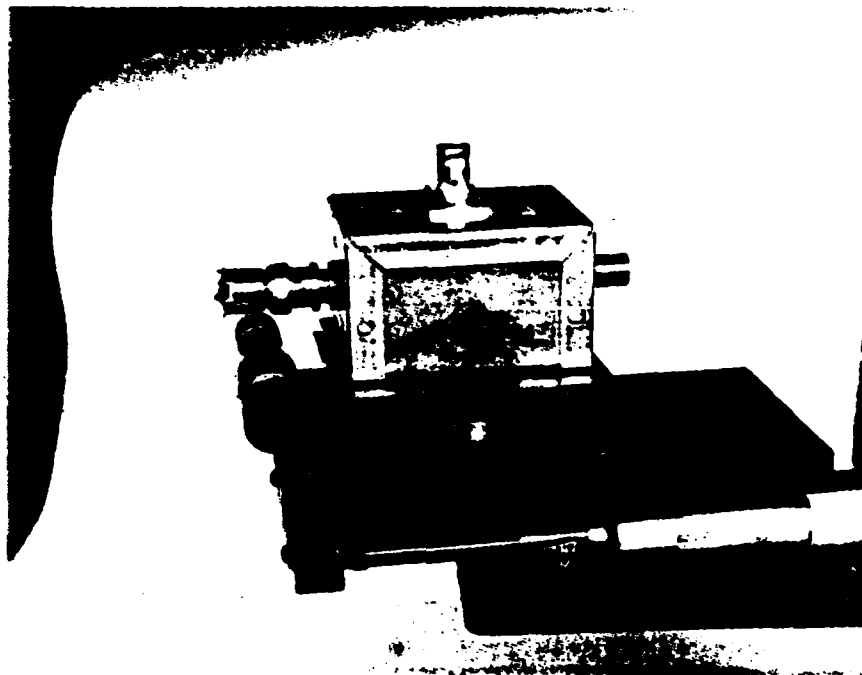


Photo 14. Avalanche Photo-Diode Used in OAFFI(CPI).
Top Connector: Input for 277 Volts from Power Supply. LHS Connector: Input for Optical Signal. RHS Connector: Output for Detected Optical Signal.

APD did not completely eliminate the RFI problem; however, it appeared to reduce RFI by 1 - 2 dB. This was not much help when RFI covered a SNR range of 8 - 33 dB (see page 149).

Now that $\hat{x}(t)$ has been optically detected, the summer performs the following operation: $e(t) = x(t) - \hat{x}(t)$. In order to precisely calculate $e(t)$, the sinusoidal optical signal $\hat{x}(t)$ must be 180 degrees out of phase with the sinusoidal RF signal $x(t)$. Note that this phase difference corresponds to choosing the appropriate tap weight along the

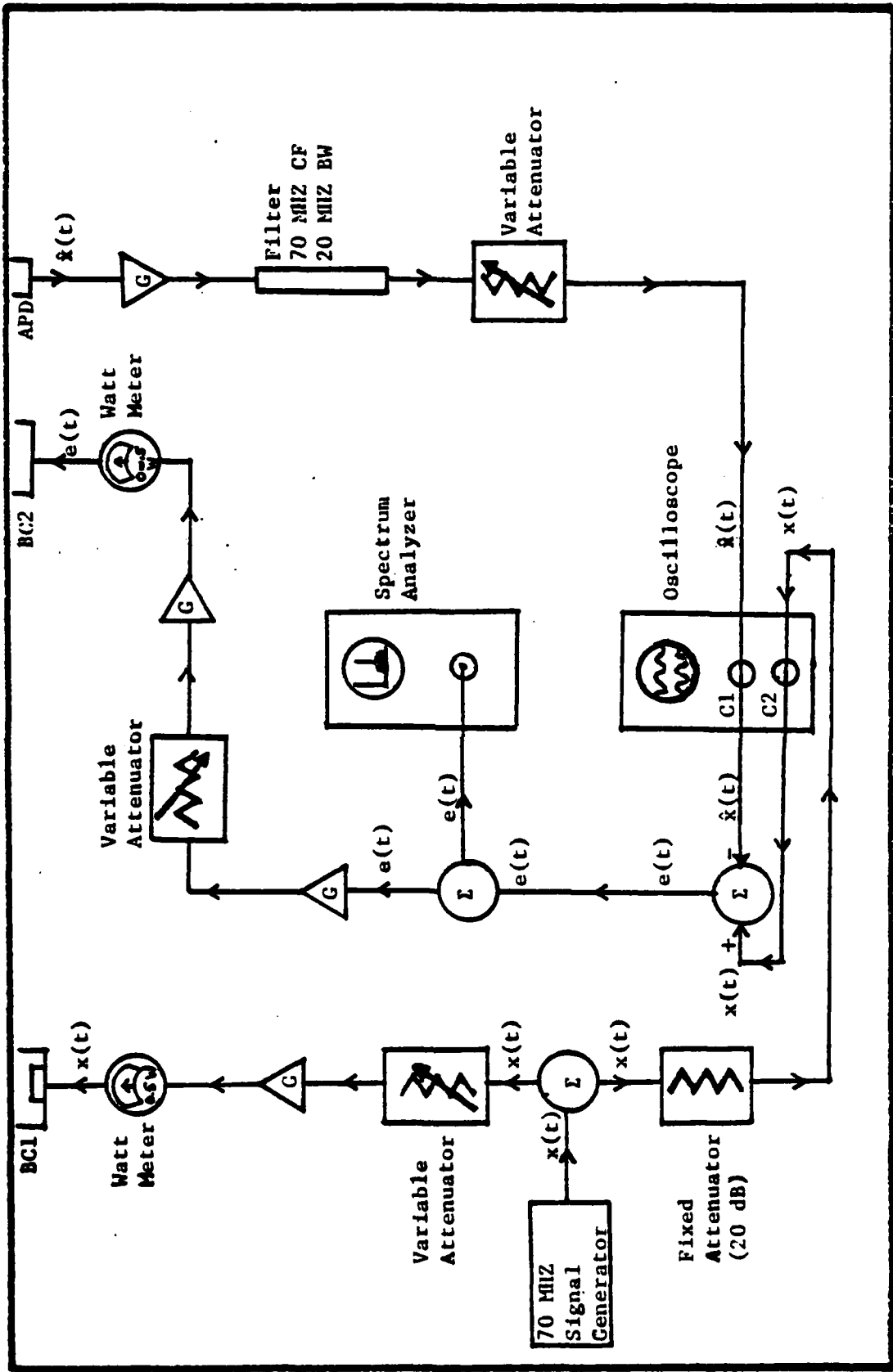


Fig. 33. Electrical Circuit for OAFFI(CPI) Not Shown in Fig. 32.

linear delay line of the Bragg cell (Fig. 12). Therefore, adding the two signals (180 degrees out of phase) accomplishes the subtraction requirement.

Of course, the end goal is to minimize the error signal $e(t)$. If $e(t)$ is in fact minimized; then $\hat{x}(t)$ will be a very good estimate of $x(t)$, and an optical adaptive filter is achieved. Fig. 33 shows the electrical circuit designed to monitor $e(t)$ for OAFFI(CPI).

To see if the feedback arrangement of Fig. 33 was working properly, the minimum possible value for $e(t)$ would be nice to know. The feedback arrangement was modeled by Fig. 34 for mathematical simplicity.

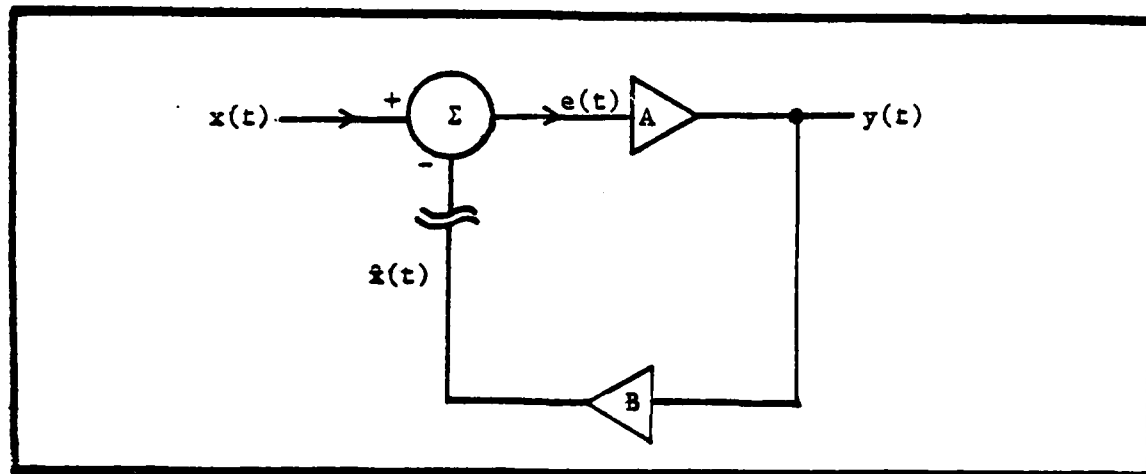


Fig. 34. Simplified Feedback Model for Fig. 33.

In the closed-loop arrangement of Fig. 34, the minimum possible value for the error signal can be derived as follows:

$$\begin{aligned}
 y(t) &= Ae(t) \\
 &= A(x(t) - \hat{x}(t)) \\
 &= Ax(t) - A \hat{x}(t), \text{ where } \hat{x}(t) = By(t) \\
 &= Ax(t) - A By(t) \\
 &= \frac{Ax(t)}{1 + AB}
 \end{aligned}$$

and

$$\begin{aligned}e(t) &= x(t) - \hat{x}(t) \\ &= x(t) - By(t) \\ &= x(t) - B\left\{\frac{Ax(t)}{1 + AB}\right\} \\ &= \frac{x(t) + ABx(t) - ABx(t)}{1 + AB} \\ &= \frac{x(t)}{1 + AB}\end{aligned}$$

Now to minimize $e(t)$, the following closed-loop constraint is required:

$$\hat{x}(t) = x(t)$$

But in the open-loop,

$$\hat{x}(t) = ABx(t)$$

When the loop is initially closed, $e(t)$ is minimized when

$$\hat{x}(t) = x(t) = ABx(t)$$

then

$$AB = 1$$

and

$$e(t) = \frac{x(t)}{1 + AB} = \frac{x(t)}{2} = -6\text{dB}$$

Therefore, the minimum possible value for $e(t)$ is -6 dB.

Observations

Before proceeding into the actual testing of OAFFI(CPI), a photographic account of the optical/electrical hardware used to construct OAFFI(CPI) is in order. Note that this hardware (Photos 15 - 18) implements the designs of Figs. 32 and 33.

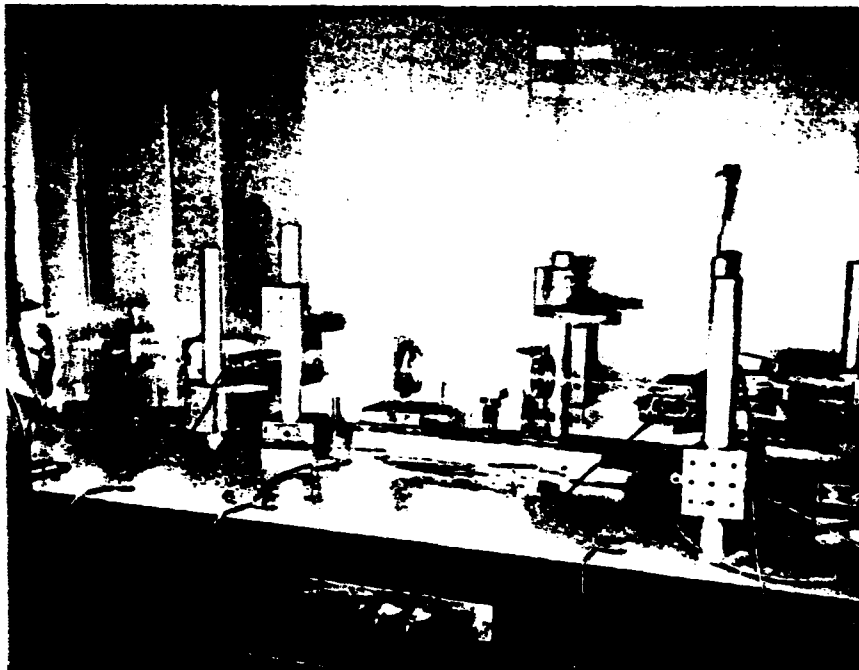


Photo 15. Optical/Electrical Hardware Used to Implement OAFFI(CPI).

In Photo 15, starting on the LHS:

Painted 5x7 index card reduces the intensity of the observed Argon-ion laser source.

Translation stage with three degrees of freedom is used to mount a 10X microscope objective and a 25 μ pinhole spatial filter.

Spherical lens SL1

Beam splitter BS1

Fully reflective mirrors RM1 and RM2 (on the back side)

Bragg cell BC1

Spherical lens SL2

Liquid Crystal Light Valve LCLV

Beam splitter BS2

Spherical lens SL3

Polarizer POL

Bragg cell BC2

Fully reflective mirror RM3 directs the optical beam toward the observation point (used for convenience only).

Spherical lens SL4

Avalanche Photo-Diode APD

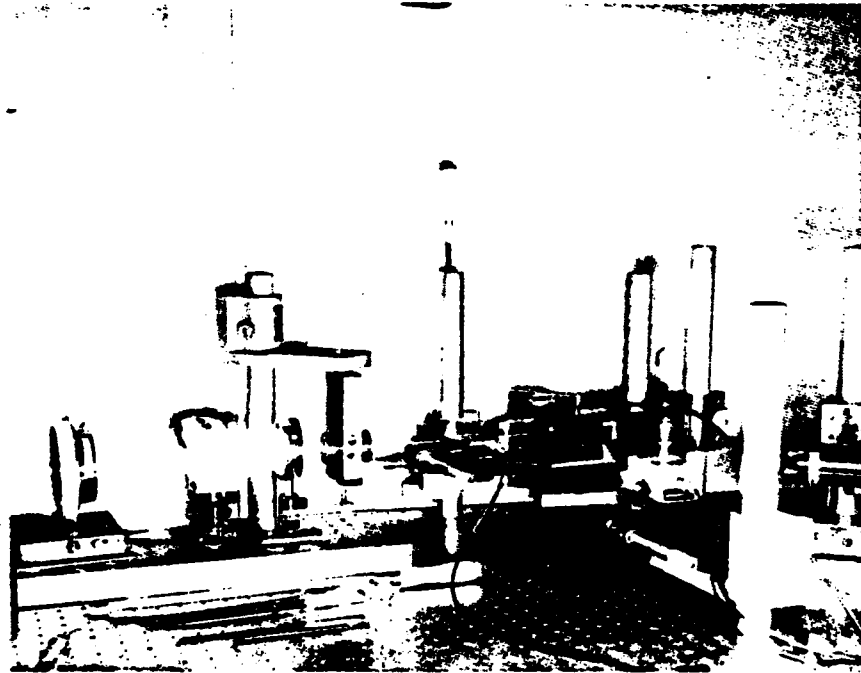


Photo 16. Better View of RM3 Region for Photo 15.
Notice the Photomultiplier Tube Housing
on the RHS.

In Photo 16, the region between LCLV and APD is easier to see than
in Photo 15.

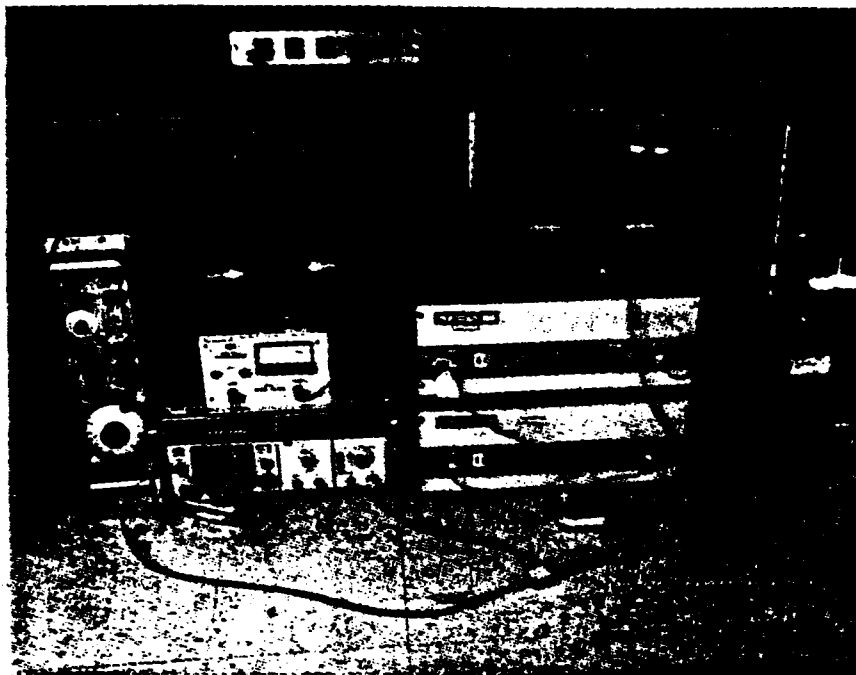


Photo 17. Supporting Equipment for OAFFI(CPI)

In Photo 17, starting on the LHS:

Variable Function Generator drove the LCLV at the recommended level: 13.7 VAC at 10 KHZ.

Wattmeter WM1 monitored BC1 input, which was kept constant at 0.5 watts.

Power Amplifier PA1 provided gain for $x(t)$ prior to entering BC1.

Frequency Synthesizer provided the 70 MHZ RF signal for $x(t)$.

Variable Attenuator VA1 controlled the input to PA1.

Two-Way Splitter TS1 (or summer) separates $x(t)$ into two paths; one to BC1 and the other to an oscilloscope for monitoring before it arrives at a second summer for $e(t) = x(t) - \dot{x}(t)$.

Fixed Attenuator (20 dB) isolates the electrical branch " $x(t)$ to BC1" from the rest of the circuit. This ensured that no reflected power from BC1 would enter into the other part of the circuit.

Variable Attenuator VA2 adjusted the gain of $e(t)$ prior to entering power amplifier PA3.

Power Amplifier PA2 increased the gain of $e(t)$.

Power Amplifier PA3 increased the gain of $e(t)$. A suitable combination of PA2, PA3 and VA2 was used to adjust the "total" gain of $e(t)$. If VA2 was not used, the signal entering PA3 would be too big and overdrive PA3.

Wattmeter WM2 monitored BC2 input, which varied from 0 - 0.5 watts due to fluctuating feedback conditions.

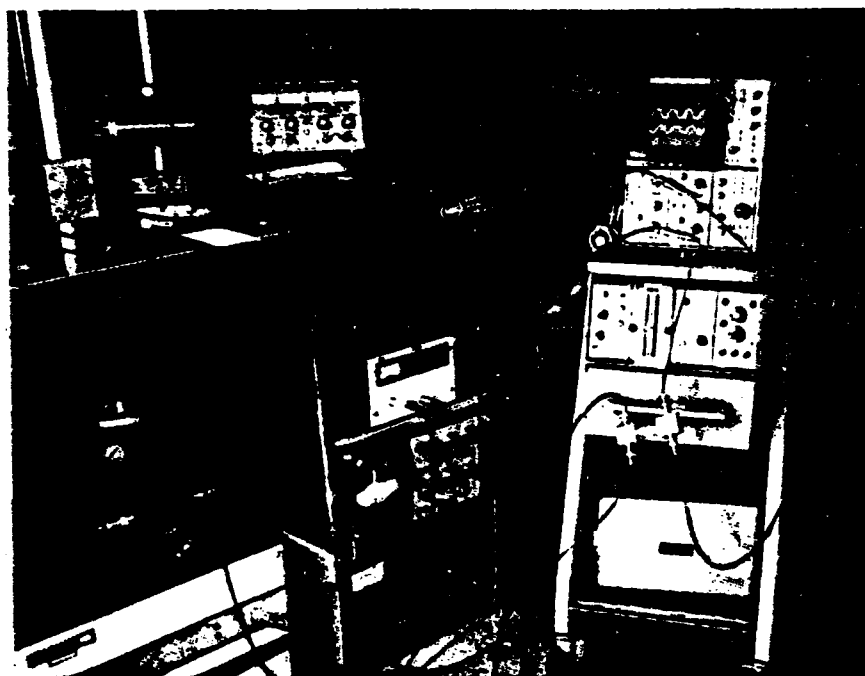


Photo 18. Supporting Equipment for OAFFI(CPI),
Continued from Photo 17.

In Photo 18, starting at the top LHS:

Photomultiplier Tube PMT used as PD in OAFFI(MZI). In OAFFI(CPI), a switch to the APD was made in order to reduce RFI. The APD had little affect on RFI reduction.

Avantek Amplifier provided gain for the optical signal $\hat{x}(t)$.

Power Supply (15 volts) for Avantek Amplifier.

Power Supply (277 volts) for APD.

Bandpass Filter (70 MHZ CF, 20 MHZ BW) reduces noise output in $\hat{x}(t)$. It is the long "pencil-like" device hanging vertically on the LHS of the Spectrum Analyzer.

Spectrum Analyzer provides a display of the error signal $e(t)$ at 70 MHz with a 20 MHz BW.

Power Supply for Argon-ion laser. The Power Supply is water-cooled.

Oscilloscope monitors $x(t)$, the top signal, and $\hat{x}(t)$, the bottom signal.

Variable Attenuator VA3 provides gain adjustment for $\hat{x}(t)$.

Two-Way Splitter TS2 (summer) provides the subtraction of $e(t) = x(t) - \hat{x}(t)$.

Two-Way Splitter TS3 (summer) separates $e(t)$ into two paths: one to the Spectrum Analyzer for monitoring and the other to BC2 for adaptive weighting.

In order to test the optical architecture of OAFFI(CPI) for proper alignment, a 70 MHz RF sinusoidal signal was simultaneously input to BC1 and BC2. This was an open-loop arrangement, no feedback from $\hat{x}(t)$. The optical alignment was adjusted to produce a maximum output (Photos 19 and 20). Note that a bandpass filter (70 MHz CF, 20 MHz BW) was used to

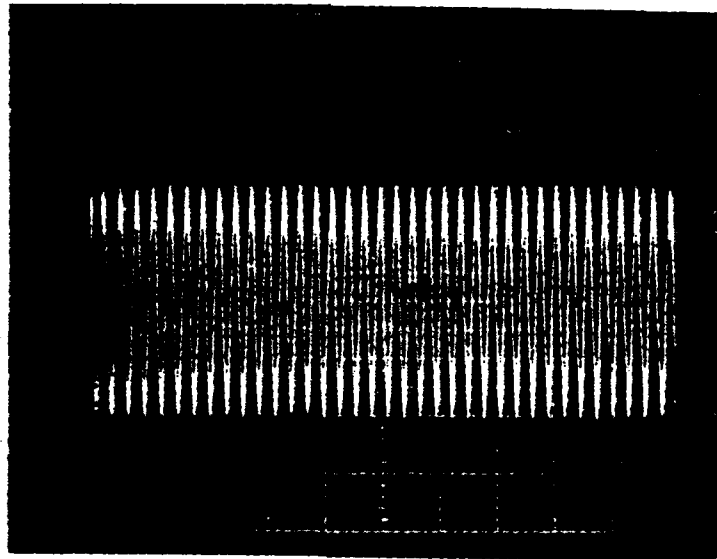


Photo 19. 70 MHz Optical Signal with Filter.
Vert. = 0.1 Volts/Div. (0.46 Volts P-P)
Hor. = .05 μ sec/Div. (1 Div. = 3.5T)

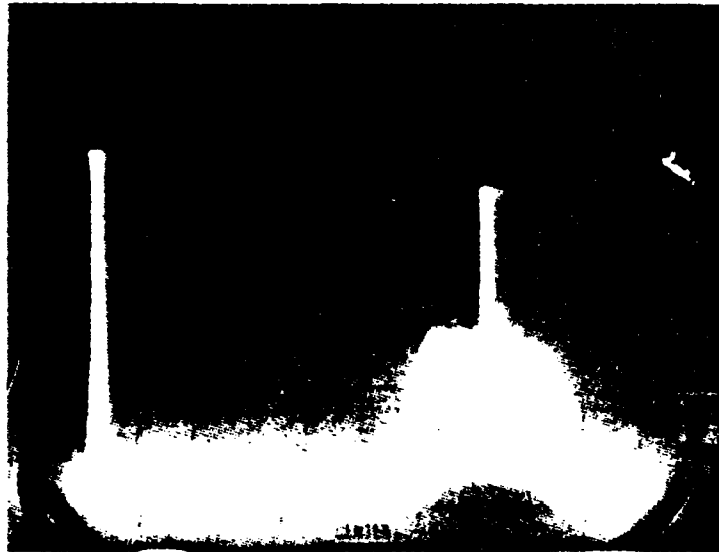


Photo 20. Spectrum of APD Output for Photo 19.
Scan Width = 10 MHz/Div.
DC = 54 dB SNR, 70 MHz = 27 dB SNR
72.5 MHz = 4 - 8 dB SNR
Note the 20 MHz BW of the Filter.

reduce the noise in the output of the APD. To appreciate the noise reduction introduced by the bandpass filter, compare Photos 19 and 20 to Photos 10 and 11, respectively. The noise is especially easy to see in the optical sine wave of Photo 10, whereas the optical sine wave of Photo 19 is much cleaner. It is interesting to note that the intruding 72.5 MHz optical signal is present in both optical architectures; i.e. OAFFI(MZI) and OAFFI(CPI). This suggests that the intruding signal may be characteristic of the optical/electrical equipment used in both architectures as opposed to scattered light.

Since the RFI problem was not solved by using the APD as a PD; different amplifiers were substituted in the branches leading to BC1 and

BC2 for the electrical circuit of Fig. 33. Even after the installation of different amplifiers, the RFI problem was still present. Moreover, the intruding 72.5 MHz signal remained unabated. These results are presented in Photos 21 and 22, respectively.

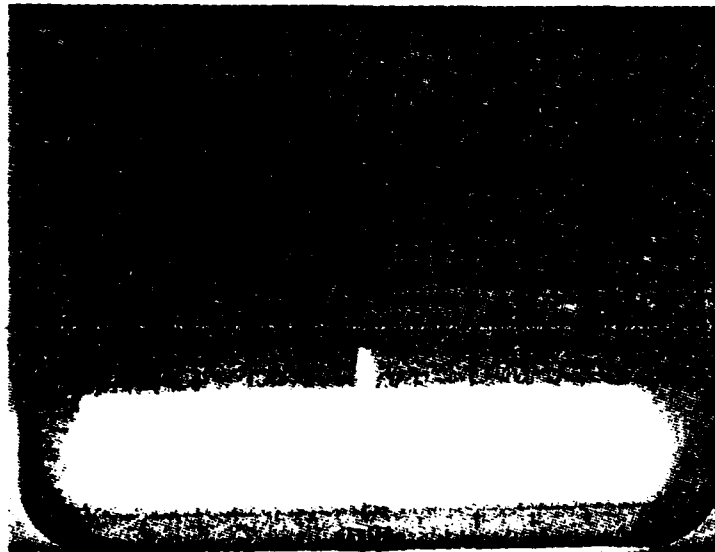


Photo 21. Spectrum of APD Output with Filter and with Optical Signal Blocked from APD.
RF = 10 - 12 dB SNR at 70 MHz with New Amps.

Now that the optical alignment has been optimized and the RFI problem reconsidered; the closed-loop test is next. Before closing the loop, $\hat{x}(t)$ is disconnected from the difference summer (Figs. 33 and 34). A 50 ohm "dummy" load is used to terminate the input, vacated by $\hat{x}(t)$. The RF signal input $x(t)$ is set at some arbitrary reference level. The detected signal $\hat{x}(t)$ is set equal to $x(t)$ by feeding $x(t)$ directly into each Bragg cell. This last step ensures that the processing gain of the feedback system (Fig. 34) is set equal to one; i.e. $AB = 1$. This minimizes the initial closed-loop value for $e(t)$. Hence, the system is now prepared for the closed-loop response.

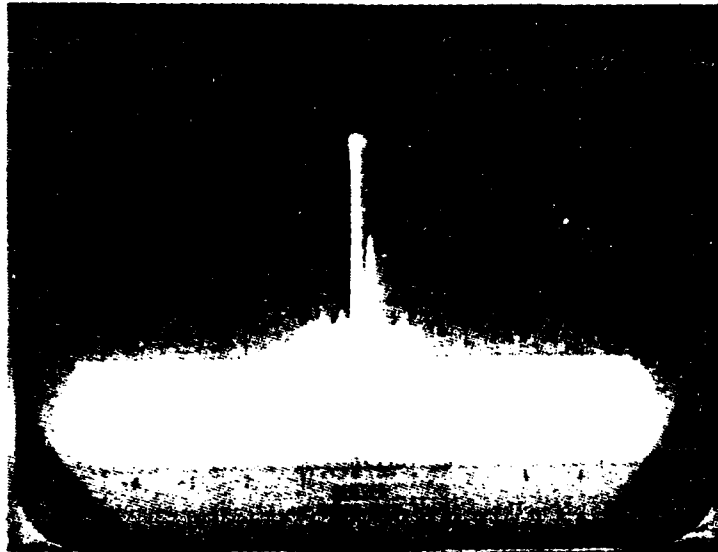


Photo 22. Spectrum of APD Output with Filter and
New Amps. Scan Width = 10 MHz/Div.
70 MHz = 42 dB SNR
72.5 MHz = 23 dB SNR

Of course, this is the ideal method to obtain the closed-loop response. During the open-loop preparations, a suitable gain could not be found for either $\hat{x}(t)$ or $x(t)$ to equate the two signals. In other words, neither the gain B for $\hat{x}(t)$ could be increased enough nor the gain for $x(t)$ decreased enough to make the two signals equal in amplitude.

Nevertheless, the loop was closed and an adaptive process was observed. To verify that the subtraction process of $e(t) = x(t) - \hat{x}(t)$ was operational, a reference level for $e(t)$ had to be established (Photo 23). Note that the reference level for $e(t)$ was established by blocking the optical signal $\hat{x}(t)$ from the APD. Thus, this was also the closed-loop reference level for $x(t)$ since $\hat{x}(t) = 0$.

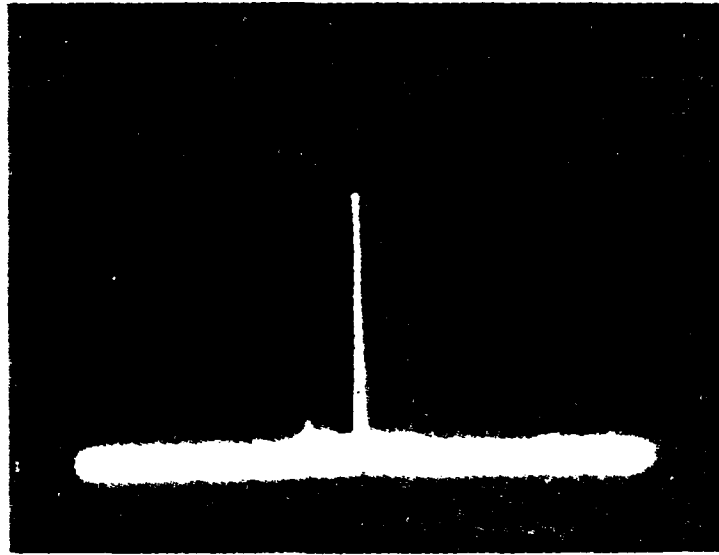


Photo 23. Spectrum of $e(t)$ with Filter for Reference Level: $e(t) = x(t) - 0$.

When the optical signal $\hat{x}(t)$, displayed in Photo 24, was detected by the APD, a subtraction of 5 dB from the reference level was observed in the error signal (Photo 25).

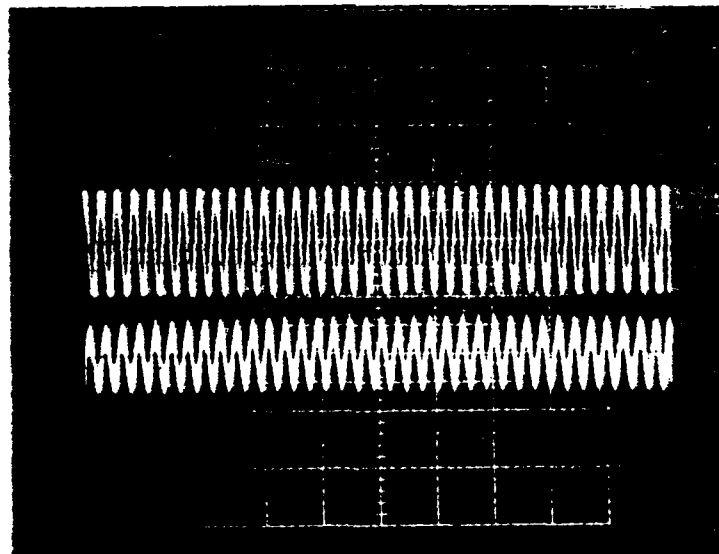


Photo 24. 70 MHz Signals $x(t)$ and $\hat{x}(t)$ for $e(t) = -5$ dB as Seen in Photo 25.
 Vert. = 0.5 Volts/Div. [$x(t) = 20$ mv P-P; $\hat{x}(t) = 17$ mv P-P]
 Hor. = .05 μ sec/Div. (1 Div. = 3.5T)

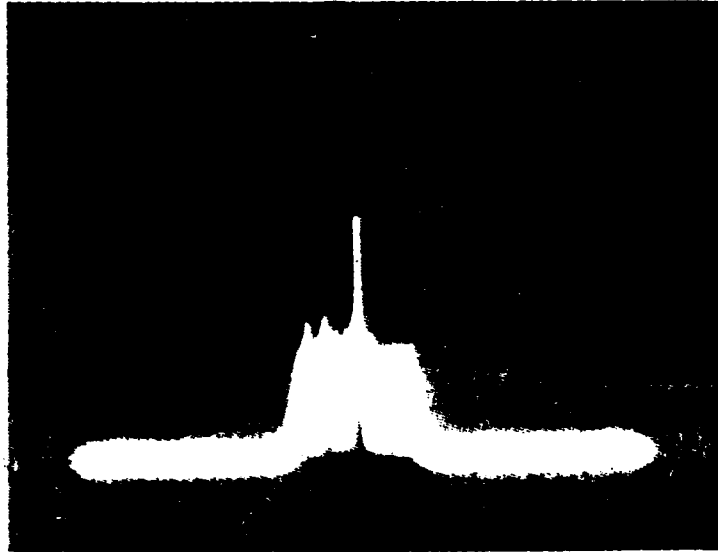


Photo 25. Spectrum of $e(t)$ with Filter and Inputs of Photo 24 for $e(t) = x(t) - \hat{x}(t) = -5$ dB from Reference Level of Photo 23.

To achieve stability in a closed-loop system, negative feedback is required. By increasing the gain of $\hat{x}(t)$, negative feedback can be realized as well as the minimum obtainable value for $e(t)$. However, in OAFFI(CPI) for a constant gain level, some input frequencies for $x(t)$ generated negative feedback in the estimate $\hat{x}(t)$. Positive feedback would cause the system to go into oscillations (Photo 26). In later tests, it was observed that the two signals could never achieve a phase difference of 180 degrees without the system going unstable. Thus, the system exhibited a certain phase margin and gain margin.

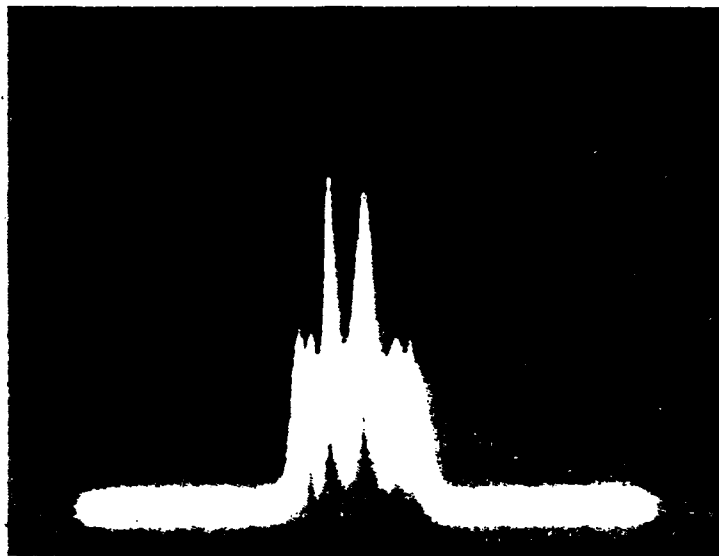


Photo 26. Spectrum of $e(t)$ with Filter and Positive Feedback Causing Oscillations (Unstable Response).

Conclusions

OAFFI(CPI) was a considerable improvement over OAFFI(MZI). The optical signal $\hat{x}(t)$ experienced no phase fluctuations. As a result of this stable phase property, a subtraction of $\hat{x}(t)$ from $x(t)$ was realized in $e(t)$. The theoretical value of 6 dB for $e(t)$ was not obtained because the open-loop requirement of $x(t) = \hat{x}(t)$, which sets $e(t)$ to an initial, closed-loop minimum value, could not be satisfied. The best the system could achieve for $e(t)$ was a subtraction of 5 dB.

Moreover, OAFFI(CPI) displayed certain properties, characteristic of an optical adaptive filter. It was especially interesting to observe the positive and negative feedback that occurred at various frequencies (see Fig. 35). Thus, the closed-loop response demonstrated a stability problem which warrants further study.

Despite the improved performance of OAFFI(CPI) over OAFFI(MZI), RFI and the intruding 72.5 MHz optical signal were still present. These two sources of interference might have affected system performance. However, the extent of the effect will not be known until these interferences are eliminated.

Nevertheless, the performance of OAFFI(CPI), thus far, warrants additional testing to determine all system parameters. These tests will be discussed in Chapter V.

Summary

In this chapter, the evolution of OAFFI was discussed. One of the fundamental building blocks of OAFFI was the Optical Spectrum Analyzer, which accomplishes real-time broadband spectrum analysis. The second building block was the Optical Excisor Version I, which used a horizontal optical beam "line" as a reference signal for heterodyning. Optical Excisor Version I also introduced a Mach-Zehnder interferometer, which enables an optical beam from two different paths to interfere at the output Fourier transform plane. Optical Excisor Version II formed the third building block. In Version II, the excision process was limited to only one frequency by removing the cylindrical lenses from the optical architecture of Version I.

The optical-to-optical transducer LCLV formed the fourth building block of OAFFI. The LCLV produces an output beam whose amplitude is proportional to the input power spectrum squared modulus of a signal ($|X(\omega) e^{j\omega t}|^2$).

As a result of studying the OSP principles behind these four building blocks, the requirements for OAFFI were well understood. The

first attempt at OAFFI implemented a Mach-Zehnder interferometer arrangement. The OAFFI(MZI) experienced phase fluctuations in the optical output $\hat{x}(t)$. Thus, no valuable data was obtained from OAFFI(MZI) other than that demonstrating its unacceptable performance.

The most promising results, to date, came from OAFFI(CPI). The common path interferometer architecture overcame the problem of phase fluctuations in $\hat{x}(t)$. The subtraction of $\hat{x}(t)$ from $x(t)$ resulted in a 5 dB reduction in $e(t)$. The closed-loop response experienced problems with stability; i.e. for a constant gain, some frequencies generated positive feedback while other frequencies generated negative feedback. The stability problem will be fully analyzed in Chapter V. In spite of these promising results, RFI and the intruding 72.5 MHz optical signal still remained.

Nevertheless, encouraging results were obtained from OAFFI(CPI). These results were significant enough to warrant an in-depth analysis of the OAFFI(CPI) architecture. In the next chapter, this analysis will determine the characteristics of OAFFI(CPI).

V. Determining OAFFI(CPI) Characteristics

Introduction

To determine the characteristics of OAFFI(CPI) various tests were performed. In this section, the test data will be analyzed and discussed to define system parameters such as minimum time delay, time aperture, bandwidth range, time-bandwidth product, frequency resolution, cancellation ratio and signal-to-noise ratio effect. Note that the most important parameter, which affects all other parameters, is the minimum time delay. If this minimum time delay, which is related to the signal time delay, can be reduced to zero for the estimated output $\hat{x}(t)$, the error signal $e(t)$ will be minimized by the "total" subtraction of $\hat{x}(t)$ from $x(t)$ in the relation $e(t) = x(t) - \hat{x}(t)$. In other words, the sinusoidal signal estimate $\hat{x}(t)$ can be inverted and added to the sinusoidal input signal $x(t)$ which results in a "total" subtraction if no signal delay exists between $\hat{x}(t)$ and $x(t)$. This is demonstrated by two optical signals in Photos 27 - 30. If a signal delay exists, the resulting output will be somewhere between the extremes of Photos 28 and 30. Therefore, the error signal $e(t)$ will not be minimized.

Since many variables exist in the system, the time delay and error signal were each tested as a function of frequency and as a function of LCLV angle. An additional test included time delay as a function of distance from the Bragg cell transducer since the Bragg cell is a linear delay line. To introduce this section, a test of the error signal as a function of frequency will be discussed.

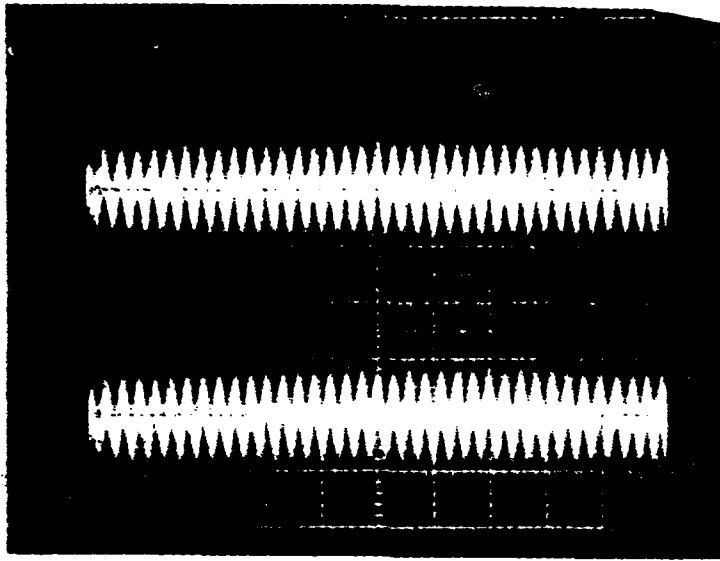


Photo 27. Two 70 MHz Optical Signals to be Added in Phase.
Vert. = 0.5 Volts/Div. (0.9 Volts P-P)
Hor. = .05 μ sec/Div. (1 Div. = 3.5T)

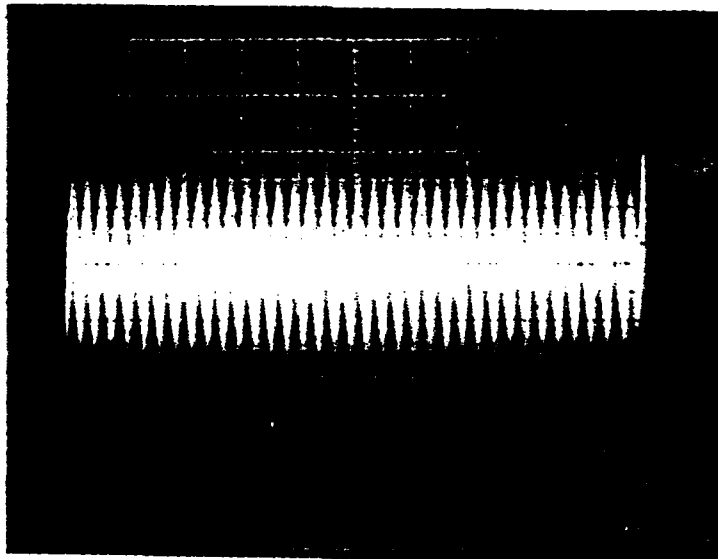


Photo 28. Result of Adding the Two Signals in Photo 27.
Vert. = 0.5 Volts/Div. (1.8 Volts P-P)
Hor. = .05 μ sec/Div. (1 Div. = 3.5T)

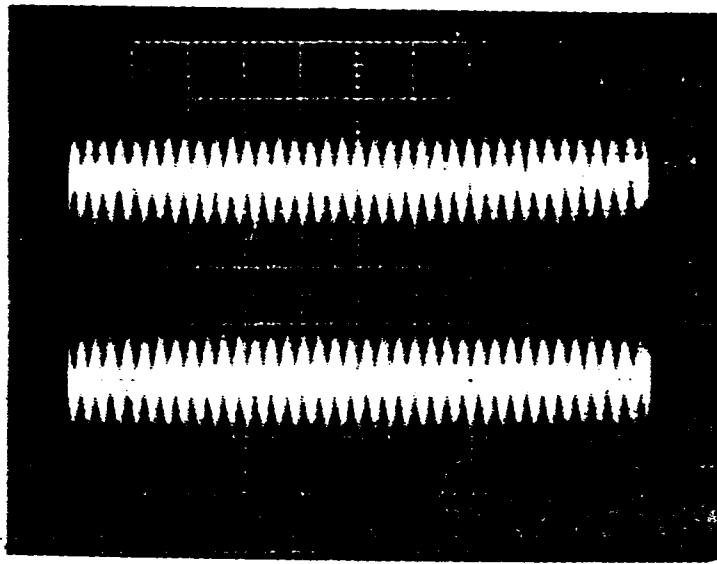


Photo 29. Two 70 MHz Optical Signals to be
Added 180 Degrees Out of Phase.
Vert. = 0.5 Volts/Div. (0.9 Volts P-P)
Hor. = .05 μ sec/Div. (1 Div. = 3.5T)

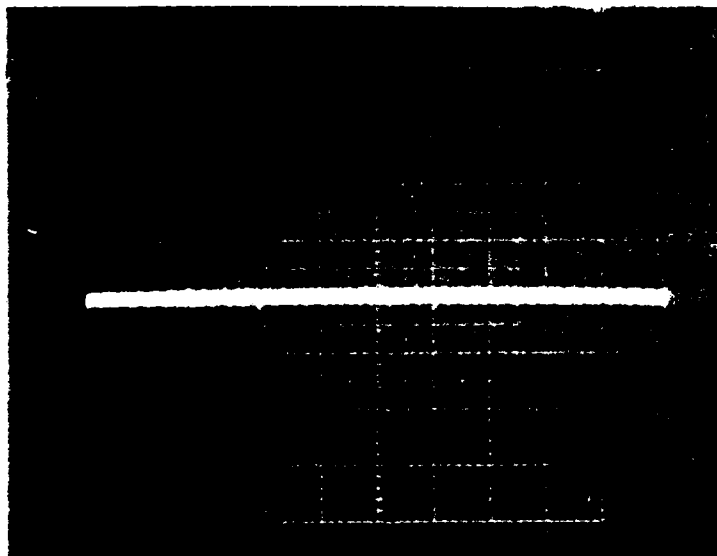


Photo 30. Result of Adding the Two Signals in Photo 29. Note
that a "total" subtraction of the two signals
results, except for some noise.
Vert. = 0.5 Volts/Div. (0.2 Volts P-P)
Hor. = .05 μ sec/Div. (1 Div. = 3.5T)

Error Signal Versus Frequency

This test revealed the relationship of the error signal $e(t)$ with the input frequency $x(t)$. The angle of the incident beam for BC2 (Fig. 32) was controlled by rotating the LCLV. In this test, the LCLV angle was constant. The system configuration was closed-loop (C-L) and included the 70 MHz bandpass filter which has a CF of 70 MHz and a BW of 20 MHz. Therefore, test frequencies were limited to the range of the bandpass filter, i.e. 60 - 80 MHz. Two trials were conducted by setting $e(t) = -5\text{dB}$ at an initial frequency as a standard via twiddling the LCLV angle. The first trial started at 70 MHz and the second at 76 MHz. Tables V and VI show the data generated from trials 1 and 2, respectively. A graph of this data appears in Fig. 35.

One observation made from the graph in Fig. 35 is that the best attainable subtraction for $e(t)$ was -5dB . There was also a problem with stability. For a stable C-L system, negative feedback is essential. However, $e(t)$ experienced positive feedback at some frequencies and negative feedback at other frequencies (Fig. 34). Hence the positive feedback triggered an unstable response in $e(t)$ which resulted in oscillations (Photo 26). To get a better definition of the stability problem, the next test will measure $e(t)$ as a function of LCLV angle.

Error Signal Versus LCLV Angle

This test revealed the relationship of the error signal with the LCLV angle. By rotating the LCLV, the phase of the incident beam for BC2 (Fig. 32) would change and thus produce a time shift in the output. Recall that the reference beam discussed in the Optical Excisor Version I also controlled the time shift of the output. In order to obtain a

Table V

Error Signal Versus Input Frequency for $e(t) = -5\text{dB}$ at 70 MHZ

LCLV Angle (Division)	Frequency (MHZ)	Error Signal (dB)
.326	62	+3
.326	65	-3
.326	70	-5
.326	72	+4
.326	75	-4
.326	78	+2

Note: Division markings for the LCLV angle are not necessarily related to a specific angle in degrees, but later serve the purpose of measuring changes in LCLV rotation which controls the angle of incidence of the optical beam entering the second Bragg cell.

Table VI

Error Signal Versus Input Frequency for $e(t) = -5\text{dB}$ at 76 MHz

LCLV Angle (Division)	Frequency (MHZ)	Error Signal (dB)
.444	62	-3
.444	65	-1
.444	70	-3
.444	72	-1
.444	75	-1
.444	76	-5
.444	78	+5

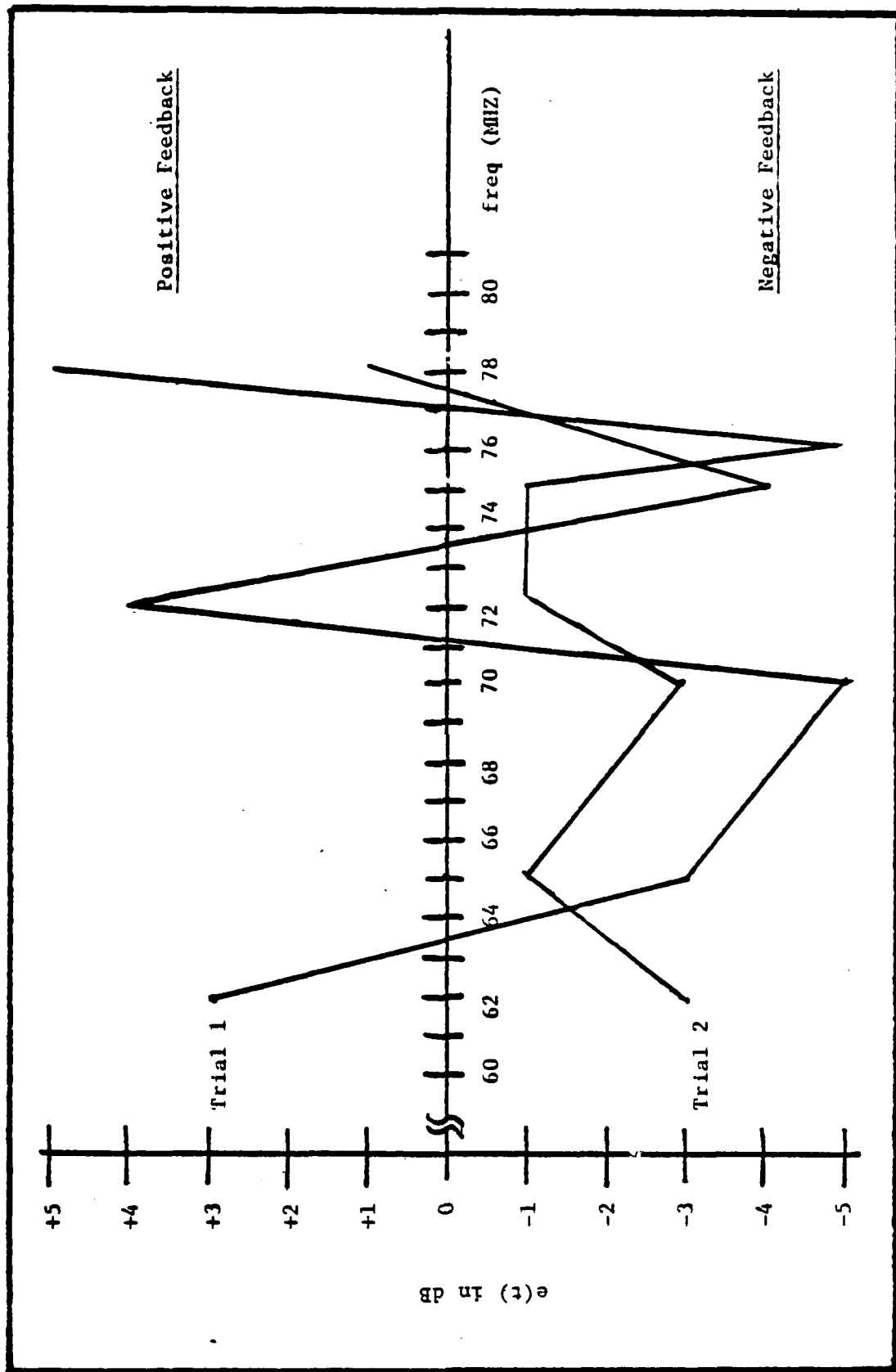


Fig. 35. Graph of Error Signal Versus Input Frequency for Two Separate Trials

wide range of data, this test included three trials at frequencies of 65, 70 and 75 MHz. The system configuration was C-L and included the 70 MHz bandpass filter.

The primary goal of this test was to better define the stability problem of OAFFI(CPI). The gain of the feedback signal $\hat{x}(t)$ was increased to the point where $e(t)$ would go into oscillations. Then, the feedback gain was attenuated by 1dB to remove the oscillations. Hence, $e(t)$ was recorded prior to the system going unstable. This was the minimum attainable value for $e(t)$ at each LCLV angle. As a result of removing all oscillations, no positive values were recorded for $e(t)$. Tables VII, VIII and IX show the data generated from input frequencies 65, 70 and 75 MHz, respectively. To convert the angle of rotation for the LCLV from divisions to degrees, three measurements were made and the following calculations resulted:

38 to 39 degrees = .500 - .420 = .080 divisions
35 to 36 degrees = .732 - .653 = .079 divisions
33 to 34 degrees = .892 - .809 = .083 divisions

Result: .081 \pm .002 divisions = 1 degree of rotation

These tables are summarized in graphical form by Fig. 36.

As a result of the graph in Fig. 36, it appears that the input frequency of 65 MHz gives the best curve of minimum values for $e(t)$. It is not known why 65 MHz yielded the best results. Also, it is not known why 70 MHz yielded the worst curve of minimum values for $e(t)$, especially when it is the center frequency of the Bragg cell.

Since this test investigated the stability problem by causing the system to oscillate and then lowering the feedback gain by 1 dB to stabilize the system, it seems that all three curves should be closer to

Table VII

Error Signal Versus LCLV Angle for Input Frequency of 65 MHZ

LCLV Angle (Division)	Error Signal (dB)	LCLV Angle (Division)	Error Signal (dB)
.587	-2	.523	-4
.584	-3	.520	-4
.582	-3	.517	-3
.581	-3	.515	-4
.580	-3	.512	-4
.578	-3	.511	-4
.575	-3	.508	-2
.571	-4	.507	-4
.570	-4	.505	-3
.569	-5	.502	-4
.568	-5	.499	-2
.566	-5	.495	-1
.565	-4	.491	-2
.563	-5	.487	-2
.562	-5	.483	-2
.559	-4	.480	-1
.554	-3	.475	0
.550	-2	.471	-3
.546	-2	.465	-2
.545	-3	.460	-2
.544	-4	.456	-2
.542	-5	.452	-2
.541	-5	.448	-1
.540	-5	.441	-2
.536	-5	.437	-2
.532	-4	.433	-2
.530	-4	.425	-1
.528	-2	.421	-1
.526	-1		

Note: $.081 \pm .002$ Divisions = 1 degree of rotation

Table VIII

Error Signal Versus LCLV Angle for Input Frequency of 70 MHZ

LCLV Angle (Division)	Error Signal (dB)	LCLV Angle (Division)	Error Signal (dB)
.588	-3.5	.539	-2
.587	-5	.538	-2
.586	-4	.537	-2
.585	-4	.536	-2
.584	-5	.535	-3
.583	-5	.534	-2
.582	-5	.533	-2
.581	-3	.532	-2
.580	-3	.530	-2
.579	-3	.529	-1
.578	-3	.528	0
.576	-3	.522	-1
.574	-2	.520	-1
.572	-1	.518	-1
.571	-1	.517	-1
.570	0	.516	-1
.568	0	.515	0
.566	-0.5	.514	0
.564	0	.513	0
.563	-0.5	.509	0
.562	-1	.508	-1
.559	-2	.507	-1
.558	-2	.506	0
.557	-2	.505	-2
.555	-3	.504	-2
.553	-2	.503	-2
.552	-2	.502	-2
.551	-2	.501	-2
.550	-1	.500	-2
.548	-2	.499	-2
.547	-2	.497	-2
.546	-1	.496	-2
.545	-2	.495	-2
.544	-2	.494	-2
.543	-2	.493	-2
.542	-2	.492	-1
.541	-1	.490	-1
.540	-2	.489	-1

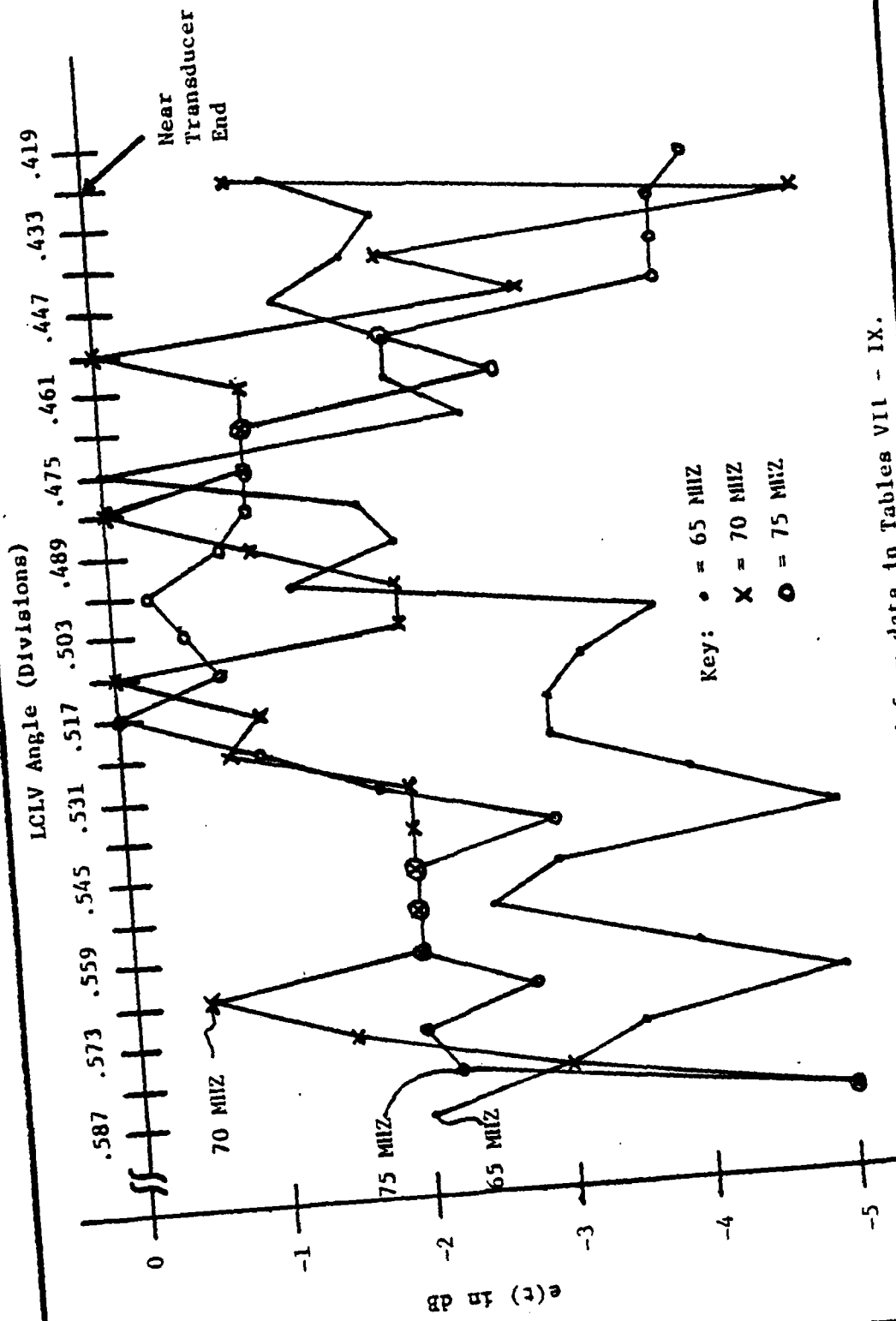
Table VIII (Cont'd)

LCLV Angle (Division)	Error Signal (dB)	LCLV Angle (Division)	Error Signal (dB)
.488	0	.450	-3
.486	-1	.448	-4
.485	-1	.447	-3
.484	0	.446	-1
.482	0	.445	-2
.481	0	.444	-2
.480	-1	.443	-2
.479	-1	.442	-2
.477	-1	.441	-1
.476	-1	.440	-2
.475	-1	.439	-3
.474	-1	.437	-3
.473	-1	.436	-2
.472	-1	.435	-3
.471	-1	.434	-5
.470	-1	.432	-5
.468	-1	.431	-2
.466	-1	.430	-2
.464	0	.428	-1
.461	-1	.426	-1
.460	-1	.425	-2
.459	0	.424	-3
.458	-1	.422	-1
.457	0	.415	0
.456	-2	.413	-1
.455	-2	.411	-1
.454	0	.408	0
.453	2	.404	0
.452	-1		

Table IX

Error Signal Versus LCLV Angle for Input Frequency of 75 MHZ

LCLV Angle (Division)	Error signal (dB)	LCLV Angle (Division)	Error Signal (dB)
.590	-3	.451	-2
.589	-5	.450	-4
.588	-4	.448	-2
.587	-5	.447	-4
.585	-4	.446	-4
.583	-3	.442	-5
.579	-2	.441	-5
.571	-2	.440	-4
.568	-2	.437	-4
.565	-3	.433	-4
.563	-3	.430	-4
.561	-3	.429	-5
.559	-2	.425	-4
.556	-2	.423	-5
.552	-2	.419	-4
.549	-2	.418	-4
.547	-2	.414	0
.544	-2	.411	-1
.541	-3	.410	-2
.539	-3	.406	-2
.535	-3	.402	-3
.532	-2	.398	-3
.525	-1	.393	-3
.520	-1	.391	-4
.517	0	.388	-4
.513	0	.387	-4
.511	-1	.384	-4
.507	0	.379	-4
.505	-1	.375	-3
.501	0	.370	-2
.482	-1	.365	0
.467	-1	.361	-3
.465	-2	.359	-4
.463	-2	.358	-2
.460	-3	.354	-2
.458	-3	.352	-3
.455	-3	.350	-2
.454	-2	.348	-1



Note: Values are interpolated from data in Tables VII - IX.

Fig. 36. Graph of Error Signal Versus LCLV Angle for Three Frequencies.

the 0 dB axis than illustrated by Fig. 36. Now that the error signal has been tested as a function of frequency and LCLV angle, the time delay of OAFFI(CPI) needs to be investigated. In the next test, the time delay τ will be measured as a function of input frequency.

Time Delay Versus Frequency

This test revealed the relationship of the time delay τ with the input frequency for $x(t)$. The C-L time delay τ is defined as the amount that $\hat{x}(t)$ is lagging or leading $x(t)$. In other words, τ is a time expression for the phase difference between $x(t)$ and $\hat{x}(t)$. For the open loop (O-L) case, τ is the time delay between $x(t)$ and $y(t)$ of Fig. 34.

Four trials implemented various system configurations: C-L with 70 MHz filter, C-L without 70 MHz filter, O-L with 70 MHz filter and O-L without 70 MHz filter. Note that one goal of this test is to determine the affect of the 70 MHz filter on τ . After the four trials are discussed, an error analysis on the gathered data will be given. This will then be followed by observations on the four trials.

The first trial measured the phase difference at each frequency between and including 60 - 80 MHz, 21 readings total. This measurement technique is demonstrated in Photo 31. Once the phase difference was measured, a graph was plotted for the 21 readings. Then, the amount of frequency change Δf was measured from the graph and hence, τ was calculated from the inverse of Δf . The system configuration was C-L with the 70 MHz filter. The initial starting point resulted from setting $e(t) = -4\text{dB}$ at 70 MHz by twiddling the LCLV angle. The feedback was continuously adjusted throughout this trial to prevent $e(t)$ from

going unstable. Table X shows the data generated from Trial 1. The information from Table X is also plotted in Fig. 37.

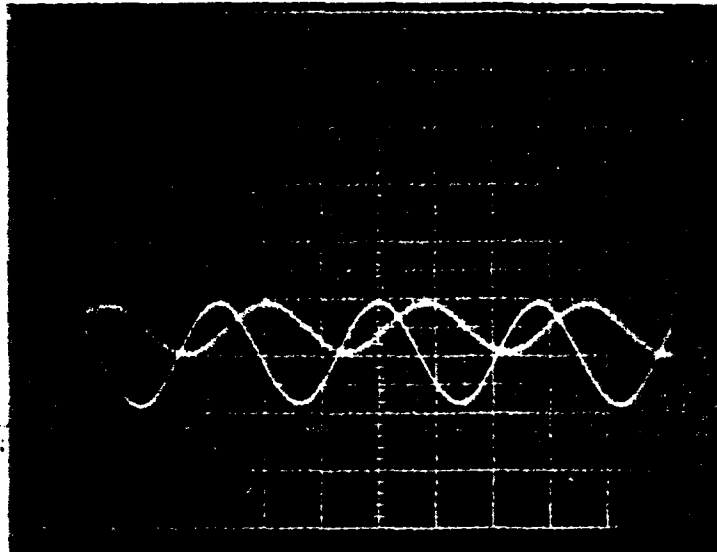


Photo 31. Phase Difference Calculation Between $x(t)$ and $\hat{x}(t)$ to Determine τ , 2.8 Divs. = 360 Degrees

$$\begin{aligned} \text{Phase Difference} &= \frac{0.8 \text{ divs.}}{2.8 \text{ divs.}} \times 360 \text{ degrees} \\ &= 120 \text{ degrees} \end{aligned}$$

$$\text{Vert.} = 10 \text{ mv/Div.}$$

$$\text{Hor.} = 5 \text{ nsecs/Div. (1 Div.} = 3.5T)$$

From the dotted line on Fig. 37, the change in frequency Δf is calculated as follows:

$$\Delta f = \frac{20 \text{ MHZ}}{6.75 \text{ cycles}} = 2.96 \text{ MHZ}$$

and τ is given by

$$\tau = \frac{1}{\Delta f} = 0.338 \text{ } \mu\text{sec}$$

Table X

Phase Difference Versus Frequency for C-L with 70 MHZ Filter

Frequency (MHZ)	Phase Diff. (Degrees)		Frequency (MHZ)	Phase Diff. (Degrees)
60	272.73		71	170.18
61	56.25		72	13.33
62	180.00		73	67.92
63	58.06		74	124.62
64	174.19		75	221.54
65	313.55		76	28.24
66	60.00		77	169.41
67	144.00		78	345.60
68	260.69		79	88.16
69	37.24		80	191.02
70	102.86			

Note: Phase differences were calculated by method discussed in Photo 31.

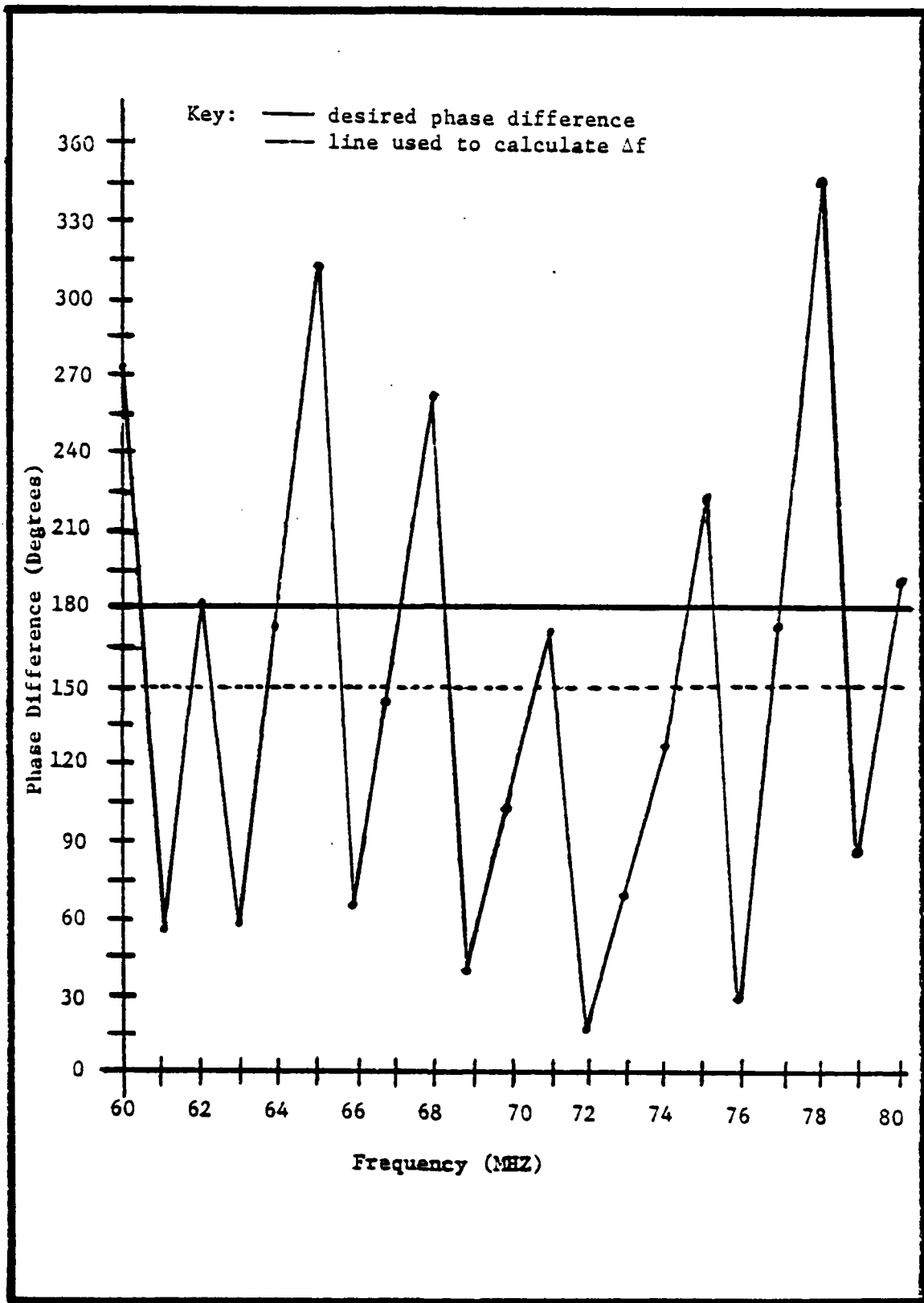


Fig. 37. Phase Difference Versus Frequency for C-L with 70 MHz Filter

Now τ represents the time delay that is characteristic of the optical beam's location along the "delay line" where it passes through the Bragg cell. According to the manufacturer's specifications, the time aperture of this particular Bragg cell is 10 μ secs. (Appendix A). Since the optical beam was passing through the approximate center of the Bragg cell, the time delay should be near 5 μ secs. Therefore, the time delay value 0.338 μ sec seems unreasonably small. Due to the nature of the curve and the small value for τ , it was determined that the phase difference was undersampled.

The second trial was meant to generate similar data as the first trial. The configuration was changed to C-L without the 70 MHz filter. However, this trial could not be accomplished due to the presence of wideband noise in the feedback. Compare the noise of $\hat{x}(t)$ in Photo 32 with that of Photo 24. More noise is present in Photo 32. This

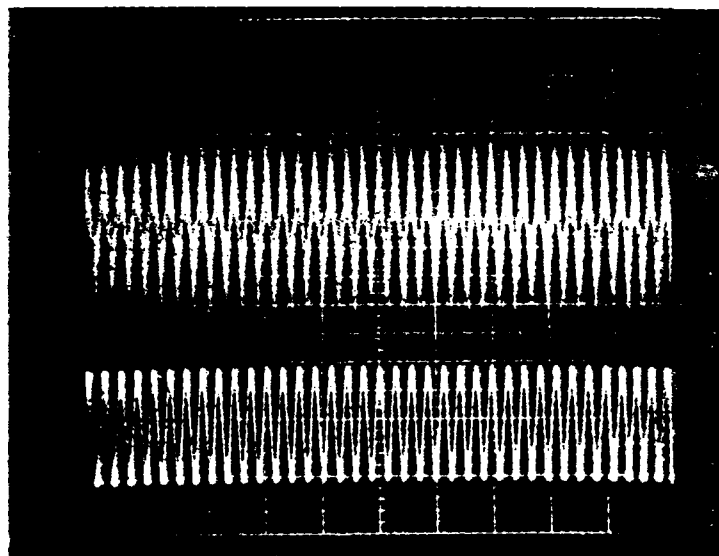


Photo 32. 70 MHz Signals $\hat{x}(t)$ and $x(t)$ for C-L w/o 70 MHz Filter
Vert. = 10 mv/Div. ($\hat{x}(t)$ = 33 mv and $x(t)$ = 21 mv)
Hor. = .05 μ sec/Div. (1 Div. = 3.5T)

wideband noise generated positive feedback which, in turn, caused $e(t)$ to go into oscillations. Compare Photo 33 with Photo 26. Of course, the oscillations in Photo 26 were constrained to the frequency range 60 - 80 MHz and those in Photo 33 had no BW constraints.

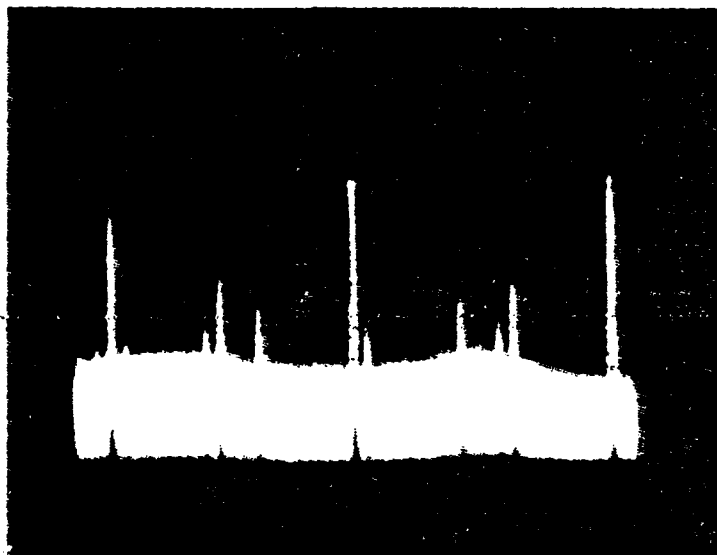


Photo 33. Spectrum of $e(t)$ w/o Filter and Positive Feedback Causing Oscillations (Unstable Response).

The third trial used an O-L configuration with 70 MHz filter. The phase difference of $x(t)$ and $y(t)$, O-L output of the APD, was set at zero degrees for 70 MHz as an initial starting point. This adjustment was made by twiddling the LCLV angle.

Due to the graph of Fig. 37 depicting undersampled data, a new method was devised for measuring τ . By using a vernier on the frequency synthesizer, changes in frequency Δf could be calculated much faster from observing a 360 degree phase change on the oscilloscope than from calculating Δf from graphs. Of course, the phase change was actually the phase difference between $x(t)$ and $y(t)$.

Once the sampled frequency was selected, the vernier would be turned until the phase difference was zero degrees. This frequency would then be recorded prior to turning the vernier to the next frequency where the phase difference was again zero degrees. Hence, this provided information on Δf for a 360 degree phase change. Thus, τ could be calculated from Δf . The results of this trial are given in Table XI.

From the results in Table XI, the time delay τ seems to be relatively constant for the 20 MHz BW. However, an average and a standard deviation for τ could more accurately define its statistical nature. Thus, Eq. (52) was used to define standard deviation.

$$SD = \text{SQRT} \left\{ \sum_{i=1}^N (\bar{x} - x_i)^2 / (N - 1) \right\} \quad (52)$$

where

N = number of entries

\bar{x} = average of N entries

x_i = entries from 1 to N

Since many more measurements were to be made for τ , the AVSD computer program of Fig. 38 was used to calculate the average and standard deviation given by Eq. (52).

By using the AVSD computer program on the data in Table XI, the following average time delay and standard deviation were computed:

$$\tau_{\text{ave}} = 8.565 \pm .177 \text{ } \mu\text{secs.}$$

Table XI

Time Delay Versus Frequency for O-L with 70 MHZ Filter

Sampled Freq. (MHZ)	Δf (MHZ)	$\tau = 1/\Delta f$ (secs.)
60	60.166 - 60.046 = .120	8.33
62	62.168 - 62.045 = .123	8.13
64	64.165 - 64.050 = .115	8.70
66	66.151 - 66.035 = .116	8.62
68	68.135 - 68.019 = .116	8.62
70	70.117 - 70.000 = .117	8.55
72	72.215 - 72.100 = .115	8.70
74	74.198 - 74.082 = .116	8.62
76	76.181 - 76.065 = .116	8.62
78	78.160 - 78.044 = .116	8.62
80	80.128 - 80.013 = .115	8.70

$\tau_{ave} = 8.565 \pm .177$ usecs.

```

                                AVSD
10  DIM A (20)
20  N = 0
50  PRINT "first number"
100 INPUT B
110 N = N + 1
120 A(N) = B
121 PRINT N; " "; B
125 PRINT "if another input value"
130 INPUT B
135 IF B = 0 THEN GO TO 145
140 GO TO 110
145 SUM = 0
150 FOR J = 1 TO N
160 SUM = SUM + A(J)
170 NEXT J
172 AV = SUM/N
175 SUM = 0
180 FOR J = 1 TO N
185 SUM = SUM + (ABS (A(J) - AV))**2
190 NEXT J
410 PRINT AV; " "; SQR(SUM/(N-1))

```

Fig. 38. Computer Program in BASIC Language to Compute Average and Standard Deviation of N Numbers.

Thus, τ_{ave} reveals that the optical beam is closer to the sound dampening end of the Bragg cell. If it were closer to the transducer end of the Bragg cell, the time delay would be in the range 0 - 5 usecs.

The "vernier" procedure for measuring the phase difference between the input and the output was much more accurate than plotting a graph. Therefore, this method of data collection will be used throughout the remainder of this analysis.

The fourth trial used an O-L configuration without 70 MHZ filter. This trial would help to determine the 70 MHZ filter's affect, if any, on the time delay τ . Again, the initial starting point was zero degrees phase difference at 70 MHZ. The results are displayed in Table XII.

From the results in Table XII, the average time delay τ is very close to the τ_{ave} calculated for Table XI. Hence, this lends support to the accuracy of this measurement procedure. Also, since the method for calculating Δf has been clearly described in the text and demonstrated in the tables, future tables will include only the values for Δf .

Next, an error analysis of the method used in collecting data for Δf will be discussed, which will then be followed by the observations.

Error Analysis

Since the procedure for calculating the phase difference included visual estimations from the oscilloscope, it is appropriate to calculate the margin for error. A full cycle of 360 degrees, for a 70 MHZ signal with 5 nsecs. per horizontal division, spanned 2.8 divisions on the oscilloscope. This fact alone reveals a reading error, since

$$\frac{5 \text{ nsecs.}}{\text{div.}} \times 2.8 \text{ Divs.} = 14 \text{ nsecs.}$$

Table XII

Time Delay Versus Frequency for O-L w/o 70 MHZ Filter

Sampled Freq. (MHZ)	Δf (MHZ)	$\lambda = 1/\Delta f$ (secs.)
60	too noisy to read	—
62	62.231 - 62.112 = .119	8.40
64	64.224 - 64.107 = .117	8.55
66	66.232 - 66.118 = .114	8.77
68	68.235 - 68.117 = .118	8.47
70	70.120 - 70.000 = .120	8.33
72	72.120 - 72.001 = .119	8.40
74	74.120 - 74.003 = .117	8.55
76	76.126 - 76.007 = .119	8.40
78	78.124 - 78.012 = .112	8.93
80	80.136 - 80.016 = .120	8.33
$\tau_{ave} = 8.513 \pm .197 \mu\text{secs.}$		

and

$$\frac{1}{14} \text{ nsecs.} = 71.429 \text{ MHZ}$$

Working backwards, a 70 MHZ signal should span 2.86 divisions. However, visual accuracy is limited to the nearest 0.1 divisions.

For example, the 70 MHZ signal in Table XII yields the following estimation for each division:

$$\frac{\Delta f}{T} = \frac{.120 \text{ MHZ}}{2.8 \text{ Divs.}} = \frac{42.857 \text{ KHZ}}{\text{Div.}}$$

There are 5 subdivisions per division or a total of 14 subdivisions for 2.8 divisions. Thus, each subdivision yields an estimation of

$$\frac{42.875 \text{ KHZ}}{\text{Div.}} \times \frac{1 \text{ Div.}}{14 \text{ Subdiv.}} = \frac{8.571 \text{ KHZ}}{\text{Subdiv.}}$$

But visual accuracy for estimating these subdivisions (Photo 26) is limited to approximately one-half of its range or a value of

$$\frac{8.571 \text{ KHZ}}{\text{Subdiv.}} \times \frac{1 \text{ Subdiv.}}{2 \text{ Halves}} = \frac{4.286 \text{ KHZ}}{\text{Half}}$$

Therefore, for a phase difference corresponding to a change in frequency of 120 KHZ, a frequency reading error of +4.286 KHZ yields a time delay error of -0.287 μ sec. and -4.268 KHZ yields a time delay error of +0.309 μ sec. This is a frequency reading error of 3.57% and a corresponding time delay error of 3.44 and 3.71%. Nonetheless, this amount of error should be tolerable since .0287 μ sec. and 0.309 μ sec.

are reasonably close to the standard deviations for τ_{ave} given in Tables XI (0.177 μ sec.) and XII (0.197 μ sec.).

Furthermore, two estimates are made for each reading; i.e., one for each sine wave peak being compared for phase difference. Between these two estimates, the reading errors will hopefully cancel each other.

Next, the data generated from the four previous trials for time delay versus frequency will be evaluated.

Observations

In later tests, the distance d along the Bragg cell's horizontal axis and the LCLV angle will be varied individually as parameters. For this past test, they were kept constant except for twiddling the LCLV angle to obtain zero phase difference at 70 MHZ as a starting point. This introduced a small variable in experimental conditions from trial to trial but the standard of zero degrees phase difference at 70 MHZ was established as the constant condition.

As a consequence of the poor results of the first trial, the method for measuring phase difference was improved by changing to the vernier frequency-adjustment method. Also, the 70 MHZ filter appeared to eliminate enough wideband noise from the feedback in the first trial to squelch oscillations which later occurred in the second trial when the filter was removed.

Nevertheless, the C-L problems of stability were still present, not only without the 70 MHZ filter, but also with the filter. For example, in the first trial, the feedback was attenuated to prevent $e(t)$ from going unstable at various frequencies. However, this attenuation was not sufficient to squelch the oscillations in the second trial when the

filter was removed. Therefore, all remaining tests will include only the O-L configuration with filter to determine OAFFI(CPI) characteristics.

Since the third and fourth trials tested an O-L configuration with and without the 70 MHz filter, respectively, an evaluation of the filter's affect on τ is in order. By comparing τ_{ave} from Tables XI and XII, an observation can be made that the 70 MHz BP filter does not significantly affect the time delay τ of the system. Their statistical averages differ by only 0.052 nsec. and their standard deviations differ by only 0.020 μ sec. Furthermore, these trials verified that τ was fairly constant over the frequency range of 60 - 80 MHz.

In summary, this test yielded the following results:

- 1) A vernier frequency - adjustment method was established as an accurate procedure to measure phase difference.
- 2) The 70 MHz BP filter has no significant affect on the time delay τ .
- 3) The time delay τ is practically constant for the 60 - 80 MHz frequency range.

The next test will investigate the relationship of τ and the LCLV angle which governs the angle of incidence for the optical beam entering the second Bragg cell.

Time Delay Versus LCLV Angle

This test revealed the affect of the LCLV angle on τ . The system configuration was O-L with the 70 MHz filter. The distance d along the Bragg cell's horizontal axis was kept constant. In order to obtain a good set of data, this test included three measurements at 65, 70 and 75 MHz for each selected LCLV angle. The results appear in Table XIII.

Table XIII

Time Delay Versus LCLV Angle for O-L with 70 MHZ Filter

LCLV Angle (Division)	Freq. (MHZ)	Δf (MHZ)	τ (μ secs.)	τ_{ave} (μ secs.)
*.359	65	.133	7.52	7.39 \pm .14
	70	.138	7.25	
	75	.135	7.41	
.371	65	.132	7.58	7.68 \pm .28
	70	.134	7.46	
	75	.125	8.00	
.383	65	.127	7.87	7.96 \pm .15
	70	.127	7.87	
	75	.123	8.13	
.395	65	.123	8.13	8.17 \pm .14
	70	.124	8.06	
	75	.120	8.33	
.407	65	.120	8.33	8.38 \pm .04
	70	.119	8.40	
	75	.119	8.40	
.419	65	.111	9.01	8.80 \pm .18
	70	.115	8.70	
	75	.115	8.70	
.431	65	.110	9.09	8.85 \pm .21
	70	.115	8.70	
	75	.114	8.77	
.443	65	.110	9.09	9.12 \pm .13
	70	.108	9.26	
	75	.111	9.01	

Table XIII (Cont'd)

LCLV Angle (Division)	Freq. (MHZ)	Δf (MHZ)	τ (μ secs.)	τ_{ave} (μ secs.)
.455	65	.106	9.43	9.46 \pm .05
	70	.105	9.52	
	75	.106	9.43	
.467	65	.101	9.90	9.87 \pm .06
	70	.102	9.80	
	75	.101	9.90	
.479	65	.100	10.00	10.10 \pm .10
	70	.098	10.20	
	75	.099	10.10	
.491	65	.095	10.53	10.21 \pm .28
	70	.099	10.10	
	75	.100	10.00	
.503	65	.092	10.87	10.72 \pm .13
	70	.094	10.64	
	75	.094	10.64	
.515	65	.093	10.75	10.71 \pm .06
	70	.094	10.64	
	75	.093	10.75	
.527	65	.090	11.11	11.11 \pm 0
	70	.090	11.11	
	75	.090	11.11	
.539	65	.086	11.63	11.26 \pm .64
	70	.086	11.63	
	75	.095	10.53	

Table XIII (Cont'd)

LCLV Angle (Division)	Freq. (MHZ)	Δf (MHZ)	τ (μ secs.)	τ_{ave} (μ secs.)
.551	65	.085	11.76	11.91 \pm .38
	70	.081	12.35	
	75	.086	11.63	
.563	65	.084	11.90	11.86 \pm .21
	70	.086	11.63	
	75	.083	12.05	
.575	65	.086	11.63	11.86 \pm .30
	70	.082	12.21	
	75	.085	11.76	

Note: For LCLV Angle, 1 degree of rotation equals $.081 \pm .002$ Divs. Also, division markings are not necessarily related to a specific angle in degrees, but serve the purpose of measuring changes in LCLV rotation.

*For LCLV angle .359, the optical beam enters near the edge of the window of BC2 at the transducer end.

The graph of this data in Fig. 39 verifies that the Bragg cell is a linear delay device.

Recall that rotating the LCLV produced a phase change in the incident beam for BC2 (Fig. 32). In this test, a time shift of τ was produced in the output $\hat{x}(t - \tau)$. Unfortunately, the minimum value obtained for τ in this test was $7.39 \pm .14$ μ secs. If the minimum value for τ could be reduced to zero, the two signals $x(t)$ and $\hat{x}(t)$ could be subtracted easily. The error signal would reach a minimum value and the system would be a successful optical adaptive filter. However, the minimum value was obtained as close to the transducer as the Bragg cell aperture would permit. So, additional testing is required to determine if τ can be reduced to zero.

From the graph in Fig. 39, the LCLV angle for $\tau_{ave} = 0$ can be extrapolated as follows:

$$Y = mx + b$$

$$\tau_{ave} = 21.91 (\text{LCLV Angle} - .359) + 7.39$$

where

subtraction of 0.359 is required for normalization

$$0 = 21.91(\text{LCLV Angle} - .359) + 7.39$$

$$\frac{-7.39}{21.91} = \text{LCLV Angle} - .359$$

$$\text{LCLV Angle} = 0.022 \text{ (Division)}$$

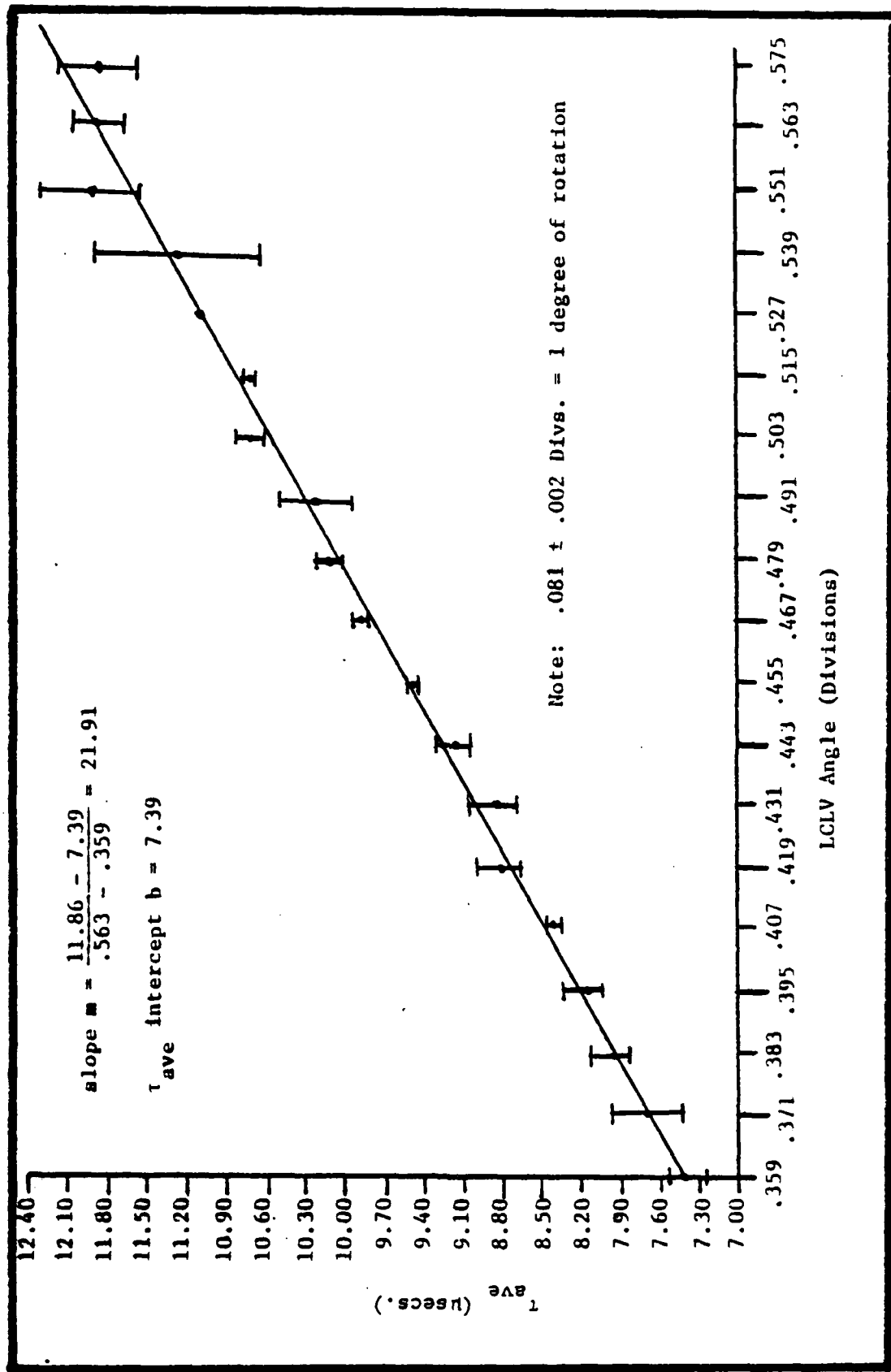


FIG. 39. Graph of τ_{ave} Versus LCLV Angle, 0-L with 70 MHz Filter

Thus, for τ_{ave} to be reduced to zero according to Fig. 39, the required LCLV angle is at Division 0.022. However, this would cause the optical beam to completely miss the Bragg cell.

Next, the relationship of τ and BC2 transducer distance d will be discussed as a possible explanation for the time delay problem.

Time Delay Versus Transducer Distance

This test measured the affect of the horizontal distance d from the transducer of BC2, on time delay τ . Since the Bragg cell is a linear delay line, the results should be linear. The system configuration was O-L and included the 70 MHZ filter.

The LCLV angle 0.451 was selected for optimum Bragg diffraction and then the angle remained constant throughout this test. Again, to obtain a good set of data, this test included three measurements at 65, 70 and 75 MHZ for each selected distance d . The results of this test appear in Table XIV and are plotted in Fig. 40

Judging from the graph in Fig. 40, the Bragg cell demonstrates its linearity well. The distance from the transducer is directly proportional to the time delay τ . The transducer distance d for $\tau_{ave} = 0$ can be extrapolated from Fig. 40 as follows:

$$Y = mx + b$$

$$\tau_{ave} = 0.644(19.50 - d) + 0.55$$

where

19.50 = a normalizing minuend

$$0 = 0.644(19.50 - d) + 0.55$$

Table XIV

Time Delay Versus Transducer Distance d for O-L with 70 MHZ Filter

d (Division)	Freq. (MHZ)	Δf (MHZ)	τ (μ secs.)	τ_{ave} (μ secs.)
*19.50	65 70 75	1.844 1.804 1.804	0.54 0.54 0.54	$0.55 \pm .01$
18.65	65 70 75	0.911 0.912 0.913	1.10 1.10 1.10	1.10 ± 0
17.80	65 70 75	0.593 0.611 0.611	1.69 1.64 1.64	$1.65 \pm .03$
16.95	65 70 75	0.450 0.455 0.455	2.22 2.20 2.20	$2.21 \pm .01$
16.10	65 70 75	0.363 0.365 0.363	2.76 2.74 2.76	$2.75 \pm .01$
15.25	65 70 75	0.303 0.305 0.304	3.30 3.28 3.29	$3.29 \pm .01$
14.40	65 70 75	0.259 0.259 0.260	3.86 3.86 3.85	$3.86 \pm .01$
13.55	65 70 75	0.227 0.228 0.227	4.41 4.39 4.41	$4.40 \pm .01$

Table XIV (Cont'd)

d (Division)	Freq. (MHZ)	Δf (MHZ)	τ (μ secs.)	τ_{ave} (μ secs.)
12.70	65	0.202	4.95	4.93 \pm .01
	70	0.203	4.93	
	75	0.203	4.93	
11.85	65	0.181	5.53	5.51 \pm .02
	70	0.182	5.50	
	75	0.182	5.50	
11.00	65	0.166	6.02	6.05 \pm .02
	70	0.165	6.06	
	75	0.165	6.06	
10.15	65	0.151	6.62	6.62 \pm .0
	70	0.151	6.62	
	75	0.151	6.62	
9.30	65	0.140	7.14	7.16 \pm .03
	70	0.140	7.14	
	75	0.139	7.19	
8.45	65	0.129	7.75	7.73 \pm .04
	70	0.130	7.69	
	75	0.129	7.75	
7.60	65	0.121	8.26	8.26 \pm 0
	70	0.121	8.26	
	75	0.121	8.26	
6.75	65	0.113	8.85	8.80 \pm .05
	70	0.114	8.77	
	75	0.114	8.77	
5.90	65	0.107	9.35	9.50 \pm .35
	70	0.101	9.90	
	75	0.108	9.26	

Table XIV (Cont'd)

d (Division)	Freq. (MHZ)	Δf (MHZ)	τ (μ secs.)	τ_{ave} (μ secs.)
5.05	65	0.101	9.90	9.90 \pm 0
	70	0.101	9.90	
	75	0.101	9.90	
4.20	65	0.096	10.42	10.38 \pm .06
	70	0.096	10.42	
	75	0.097	10.31	
3.35	65	0.090	11.11	10.99 \pm .12
	70	0.092	10.87	
	75	0.091	10.99	
2.50	65	0.087	11.49	11.49 \pm 0
	70	0.087	11.49	
	75	0.087	11.49	

Notes: For transducer distance d, 4.0 divisions equals 1 centimeter.
 *Distance d = 19.50 is the starting mark near the edge of the window of BC2 at the transducer end. It is an arbitrary starting point and not necessarily the true distance from the transducer.

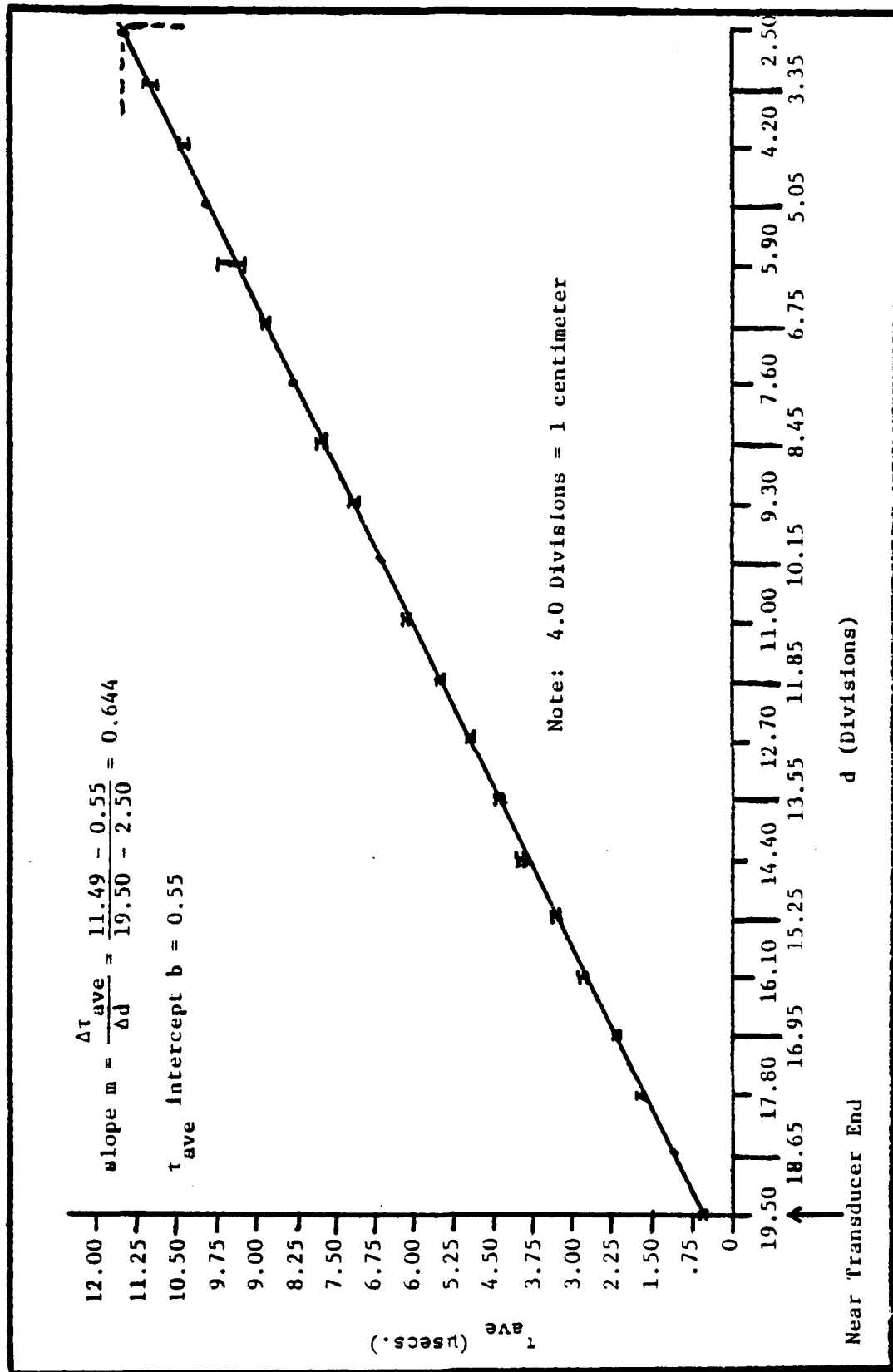


Fig. 40. Graph of τ_{ave} Versus Transducer Distance d , O-L with 70 MHz Filter

$$\frac{0 - 0.55}{0.644} = (19.50 - d)$$

$$d = 20.35 \text{ (Division)}$$

Thus, for τ_{ave} to be reduced to zero according to Fig. 40, the required transducer distance d is at division 20.35. Unlike the extrapolated result (page 141) for the LCLV angle at $\tau_{ave} = 0$, this particular value of $d = 20.35$ would keep the optical beam on the Bragg cell but not within the constraints of the aperture (Appendix A). Perhaps a Bragg cell with a larger aperture is necessary.

Nevertheless, a measured value of 0.55 μ secs. for τ_{ave} is promising and warrants additional testing. Also, Table XIV reveals the total time aperture γ of the Bragg cell: $11.49 - .55 = 10.94$ μ secs.

In the next test, the primary goal will be to find the minimum attainable value for τ_{ave} .

Minimum Time Delay Observed

Thus far, the LCLV angle and the transducer distance d have each been evaluated for their affect on τ_{ave} . Although the LCLV angle of division 0.359 yielded a "high" minimum value of 7.39 μ secs. for τ_{ave} , the linearity of the Bragg cell was still demonstrated. In addition, the time delay decreased as the optical beam was directed closer to the transducer end of the Bragg cell. Furthermore, the transducer distance d of division 19.50 yielded a minimum value of 0.55 μ sec. for τ_{ave} . This latter value for τ_{ave} was encouraging and sparked the idea that perhaps a still lower minimum value is attainable.

Therefore, the primary purpose of this test is to minimize τ by trying different combinations of LCLV angles and transducer distances d .

Of course, the minimum value for τ_{ave} will occur at the transducer end of the Bragg cell. So, the only value actually selected for the transducer distance d was 19.89. This, in conjunction with the selected LCLV angles, permitted the optical beam to enter the BC2 aperture as close to the transducer as possible. The system configuration was O-L and included the 70 MHz filter. The results of this test are given in Table XV.

Thus, according to Table XV, the minimum attainable value for τ_{ave} is 0.29 μ sec. Furthermore, this was the minimum time delay observed in the entire OAFFI(CPI) venture.

Next, a detailed analysis on the RFI problem will be given. Since RFI was ever present throughout OAFFI testing, its affect on system performance is unknown.

Radio Frequency Interference

RFI was detected as early as the Optical Excisor Version II experiment and it was always present throughout the remaining experiments. RFI was discovered by blocking the optical signal from the optical detector. The detector output was monitored by a spectrum analyzer which still displayed an output power spectral density for 70 MHz with no optical input to the detector. Although each optical detector had a slightly different RFI response, all of the detectors which include the excisor detector chip, the PMT and the APD demonstrated RFI responses in the range of 6-34 dB above the noise floor of the spectrum analyzer.

The most baffling problem with the RFI was that it varied, depending on the placement of coaxial cables, location of the

Table XV

Minimum Value Test for τ_{ave} with O-L and 70 MHZ Filter

LCLV Angle (Division)	Freq. (MHZ)	Δf (MHZ)	τ (μ sec.)	τ_{ave} (μ sec.)
.451	65	3.366	0.30	0.29 \pm .01
	70	3.376	0.30	
	75	3.641	0.28	
.456	65	2.993	0.33	0.33 \pm .01
	70	2.968	0.34	
	75	3.166	0.32	

Note: Transducer distance d was kept constant at division 19.89.

experimenter and other undetermined phenomenon. The RFI source was the RF signal generator (Fig. 33).

Several modifications were attempted to reduce the RFI, but these produced no significant improvement. These modifications included the following:

- 1) Shielding all amplifiers with aluminum foil
- 2) Shielding the excisor detector chip with aluminum foil
- 3) Shielding cable connections with aluminum foil
- 4) Installed DC coupling capacitors across the outputs of the optical detectors
- 5) Tried different lengths of coaxial cable
- 6) Moved the RF signal generator as far from the optical detector as feasible (3-5 meters)
- 7) Tried different amplifiers

Since, the RFI could not be eliminated, the only remaining thing to do was to measure its performance. The system configuration was O-L and included the 70 MHZ filter. After blocking the optical beam input to the APD, RFI was measured in the output spectrum as a function of frequency. These results appear in Table XVI and Fig. 41. It is interesting to note in Fig. 41 that the minimum RFI occurred at 72 MHZ, whereas the intruding optical signal of previous experiments appeared at 72.5 MHZ (Photo 22).

Another item of concern was the transmission losses to Bragg cells BC1 and BC2. In Ref. 30, transmission losses are defined in terms of reflection coefficient (Γ_L) and voltage standing wave ratio (VSWR). The VSWR is given by

Table XVI

RFI Measured as a Function of Frequency, O-L with 70 MHZ Filter

Frequency (MHZ)	RFI SNR (dB)		Frequency (MHZ)	RFI SNR (dB)
60	33		71	16
61	32		72	8
62	26		73	14
63	22		74	18
64	15		75	17
65	14		76	17
66	14		77	14
67	16		78	13
68	19		79	13
69	20		80	13
70	20			

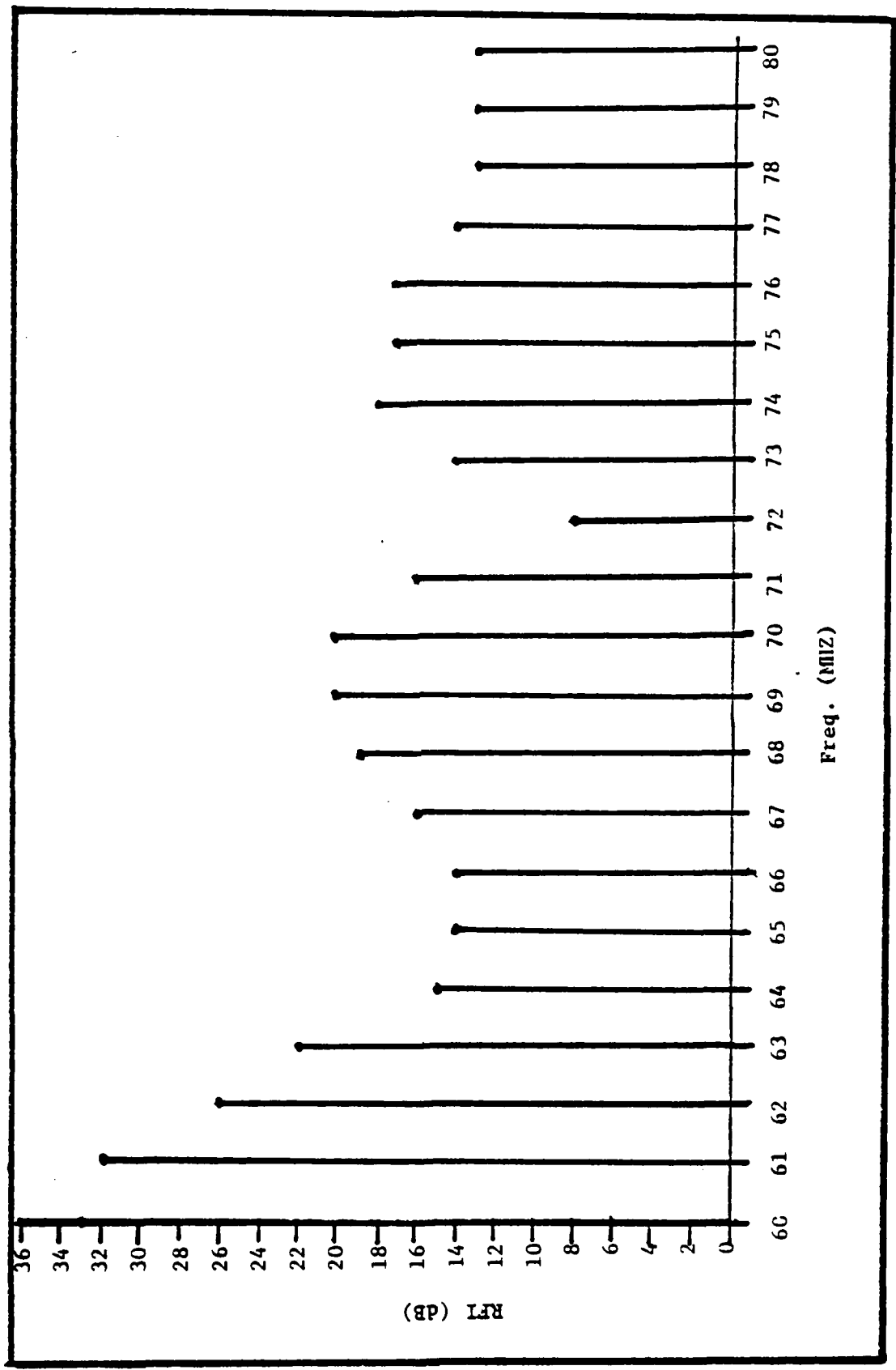


Fig. 41. RFI Versus Frequency, 0-1. with 70 MHz Filter

$$VSWR = \frac{1 + |\Gamma_L|}{1 - |\Gamma_L|}$$

where

$$\Gamma_L = \frac{\text{reflected voltage}}{\text{incident voltage}}$$

|| = magnitude of a complex quantity

The reflected power of BC1 and BC2 was measured to be 0.08 and 0.05 watts, respectively. The incident power to each Bragg cell was 0.5 watts. Since ratios are involved and power was measured instead of voltages, the magnitudes of the reflection coefficients are calculated as follows:

$$|\Gamma_L (BC1)| = \text{SQRT} (.08/0.5) = 0.40$$

$$|\Gamma_L (BC2)| = \text{SQRT} (.05/0.5) = 0.32$$

The resulting VSWR for BC1 and BC2 are given by

$$VSWR (BC1) = \frac{1 + .4}{1 - .4} = 2.33$$

$$VSWR (BC2) = \frac{1 + .32}{1 - .32} = 1.92$$

From the chart in Fig. 42, it is shown that BC1 reflects 16% of its incident power and BC2 reflects 10% of its incident power. These percentages correspond to a return loss of 8 and 10 dB for BC1 and BC2, respectively.

In addition to measuring transmission losses, SNRs from the

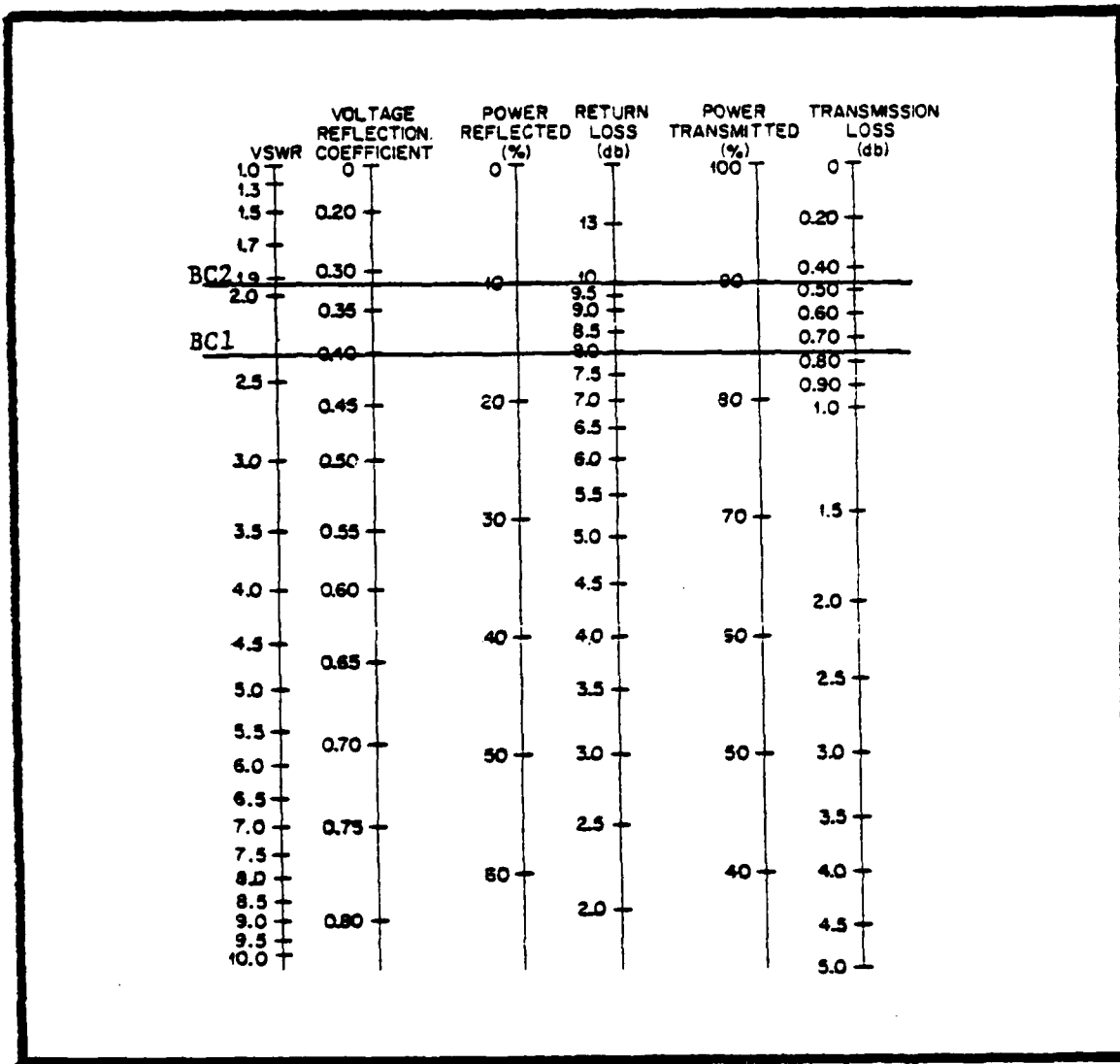


Fig. 42. VSWR Nomograph.
 Read equivalent values
 on the horizontal lines
 (Ref. 23:8-6).

spectrum analyzer were also considered. For the preceding VSWR test, the normal Bragg cell load of 50 ohms was unchanged. Thus, the resulting SNRs are found in Table XVII.

To reduce the amount of reflected power or return loss, an additional load of 50 ohms was added in series to each Bragg cell. The reflected power of each Bragg cell, for an incident power of 0.5 watts, was measured at 0 watts. The resulting SNRs are found in Table XVIII.

As a result of comparing the SNRs in XVII and XVIII, the additional 50 ohm load was removed from each Bragg cell. It was decided that the additional 3 dB of SNR for the 70 MHz optical signal in Table XVII was more significant for overall system performance than the return losses of 8 and 10 dB. In addition, the RFI was reduced by 4 dB.

In the next section, the collected data for OAFFI(CPI) will be analyzed to determine its characteristics. The following characteristics will be discussed: minimum time delay, time aperture, BW range, time-BW product, frequency resolution, cancellation ratio and SNR effect.

Data Analysis

In this section, the basic characteristics of OAFFI(CPI) will be calculated from the previous data. Definitions of the various terms will be briefly stated and then the corresponding OAFFI(CPI) data will be incorporated into the definition.

Minimum Time Delay

The minimum time delay τ was obtained by a trial and error method of selecting various combinations of the LCLV angle and transducer

Table XVII

SNRs Measured for Normal Bragg Cell 50 Ohm Load

Signal	SNR (dB)
70 MHZ Optical	41
70 MHZ RFI	11
72.5 MHZ Optical	25

Table XVIII

SNRs Measured for Additional 50 Ohms Added in Series to Each Bragg Cell

Signal	SRN (dB)
70 MHZ Optical	38
70 MHZ RFI	15
72.5 MHZ Optical	20

distance d for the OAFFI(CPI) architecture. The minimum time delay observed for τ was 0.29 μ secs. By reducing this minimum time delay to zero, it is conjectured that the feedback stability problem may be eliminated.

Time Aperture

The time aperture γ for OAFFI(CPI) will be defined as the time aperture of BC2. This represents the required time for a new input frequency to be processed along the entire delay line. For OAFFI(CPI), the time aperture γ was 10.94 μ secs.

Bandwidth Range

Although the BW range of the Bragg cells used in OAFFI(CPI) was 40 MHZ, the bandpass filter constrained the BW range to 20 MHZ. With state-of-the-art Bragg cells, the BW range could reach 1 GHZ.

Time-Bandwidth Product

The time-bandwidth product is the product of the time aperture γ and the BW range. In OAFFI(CPI), the time-bandwidth product was:

$$10.94 \mu\text{secs} \times 20 \text{ MHZ} = 218.8$$

It could be 437.6 with a 40 MHZ BW. The time-bandwidth product is also the number of resolvable spots, spatial frequencies, in the FT plane. Furthermore, this also corresponds to the total number of possible tap weights.

Frequency Resolution

In most optical systems, the frequency resolution is the reciprocal of the time aperture. This would translate to a frequency resolution of 91.41 KHZ for OAFFI(CPI). However, the optics were not aligned ideally to achieve this. Therefore, in OAFFI(CPI), an alternate method for calculating frequency resolution is required. The frequency resolution can be derived from αf which represents the angle of projected light to the lens, where $\alpha = \lambda/s$ and $f =$ focal length of the Fourier transforming lens. The wavelength of the optical source is represented by λ and the spot size of the FT is represented by s . The minimum resolvable spot size for the LCLV is 50μ and λ for Arg-ion is 514.5 nanometers. The focal length of the FT lens was 19.05 cm. (Table IV). Therefore,

$$\alpha f = \frac{\lambda f}{s} = \frac{.5145 \mu}{50 \mu} (19.05 \text{ cm}) = 0.196 \text{ cm}$$

The sound travels the length of the Bragg cell (3.8 cm.) in 10.94 μ secs. Thus, the distance traveled in 1 μ sec. is 0.347 cm. Therefore, for a light distribution of 0.196 cm., the required time for interaction with the sound is

$$\frac{0.196 \text{ cm}}{0.347 \text{ cm}/\mu\text{secs.}} = 0.564 \mu\text{secs.}$$

The reciprocal of this results in a frequency resolution of 1.77 MHZ.

Cancellation Ratio

The cancellation ratio is the amount of reduction or subtraction accomplished in the SNR of the error signal $e(t)$. The best cancellation

that OAFFI(CPI) could achieve was 5 dB. Note that cancellation ratio was called signal rejection in the OAF.

Signal-to-Noise Ratio Effect

The SNR effect measures the largest SNR possible for the output $\hat{x}(t)$. In OAFFI(CPI), the optical output of $\hat{x}(t)$ achieved a SNR of 42 dB. Table XIX summarizes the characteristics of OAFFI(CPI) that resulted from this thesis endeavor.

Table XIX

OAFFI(CPI) Characteristics

Item	Value
Center Frequency	70 MHZ
Minimum Time Delay	0.29 μ secs.
Time Aperture	10.94 μ secs.
Bandwidth Range	20 MHZ
Time-Bandwidth Product	218.8
Frequency Resolution	1.77 MHZ
Cancellation Ratio	5 dB
SNR Effect	42 dB

VI. Summary, Conclusions and Recommendations

Summary

This thesis has investigated the feasibility of implementing an optical adaptive linear predictor in the frequency domain. The OAF, time domain equivalent of OAFFI, was limited to about 100 MHz BW. Although OAFFI may yield the full potential BW of 1 GHz available in state-of-the-art Bragg cells, it was limited to 20 MHz in this thesis by the bandpass filter which was used to eliminate wideband noise.

The theory of OAFFI was developed from a combination of adaptive linear prediction with correlation cancellation loops and optical signal processing techniques which included Fourier optics and acousto-optics. Several optical architectures, namely, the Optical Spectrum Analyzer, the Optical Excisor Versions I and II and the Liquid Crystal Light Valve Architecture, were discussed as fundamental building blocks for OAFFI. As the thesis progressed, each new architecture contributed an additional OSP application that was later used in OAFFI, which itself was implemented in two versions.

The first version of OAFFI implemented the Mach-Zehnder interferometer. However, OAFFI(MZI) experienced severe problems with phase stability in the output $\hat{x}(t)$. These phase stability problems resulted from external sources, air currents and vibrations, affecting the two optical paths differently. Therefore, no valuable data was obtained from OAFFI(MZI) other than that demonstrating its unacceptable performance.

Since the phase stability problem of OAFFI(MZI) was essentially the result of using two separate paths with almost uncontrollable external sources of modulation, a common path interferometer was sought and was achieved. Although OAFFI(CPI) eliminated the phase stability problem of $\hat{x}(t)$, the error signal $e(t)$ experienced stability problems caused by positive feedback.

The stability problem could be manually corrected by attenuating $\hat{x}(t)$. However, this would increase the error signal $e(t)$ since $e(t) = x(t) - \hat{x}(t)$. This characteristic seems to be due to an inherently insufficient gain margin of the system. In addition, a 180 degrees phase difference between $x(t)$ and $\hat{x}(t)$ for subtraction purposes was never realized for some frequencies. This also seems to be due to an inherently insufficient phase margin of the system.

In spite of these inherent problems, OAFFI(CPI) demonstrated a subtraction of 5 dB which was characteristic of an adaptive linear predictor. Therefore, various tests were conducted to determine additional characteristics of OAFFI(CPI). These results will be discussed in the next section.

Conclusions

By analyzing the data collected from the various tests, the following characteristics of OAFFI(CPI) were revealed:

- 1) The error signal $e(t)$ exhibited stability problems at various frequencies. At some frequencies, positive feedback triggered oscillations in $e(t)$ and at other frequencies, negative feedback accomplished signal cancellation, with a maximum cancellation of 5 dB observed. Also, the system exhibited an inherently insufficient gain margin and phase margin. While attempting to reduce the error signal, $e(t) = x(t) - \hat{x}(t)$, to zero; oscillations would start not only when the gain on $\hat{x}(t)$ was increased beyond an undetermined threshold to produce

negative feedback, but also when the phase difference of the two signals would approach some undetermined threshold prior to being 180 degrees out of phase.

- 2) The time delay τ is practically constant over the frequency range of 60 - 80 MHZ.
- 3) The 70 MHZ bandpass filter does not significantly affect the time delay τ and also helps to filter out wideband noise.
- 4) The Bragg cell is a linear delay line and hence, the minimum delay available is at the transducer end. The minimum time delay observed was 0.29 μ secs. If the minimum time delay can be reduced to zero; a total subtraction of the two signals will result.
- 5) The affect of the RFI and the 72.5 MHZ intruding optical signal on the system performance of OAFFI(CPI) is unknown.

The characteristics mentioned above are well documented by tables and graphs in Chapter V.

As was the case with the OAF, equipment availability and inherent architectural shortcomings prohibited the full potential of OAFFI(CPI) from being realized. Specifically, a wider bandpass filter than 20 MHZ was not available and the system exhibited a feedback stability problem that severely constrained the signal cancellation ability of the system.

Nevertheless, if the stability problem of OAFFI(CPI) is solvable, an optical adaptive filter implemented in the frequency domain seems feasible. Moreover, until the full potentials of both the time domain version, OAF, and the frequency domain version, OAFFI, are realized; a decision on which is the best performing optical adaptive filter cannot be made. Furthermore, the decision will possibly be driven by the particular application. Therefore, a frequency domain version aptly compliments a time domain version and OAFFI could still be

a profitable accomplishment; if not for greater bandwidth than the OAF, then at least as a viable frequency domain alternative to the OAF.

Finally, this thesis has tested the feasibility of an optical adaptive filter implemented in the frequency domain. The performance of OAFFI(CPI) has demonstrated some positive results that should stimulate further investigations.

Recommendations

In this section, recommendations for future research on the OAFFI will include two separate suggestions. The first suggestion will incorporate the same OAFFI(CPI) architecture used in the thesis. The second suggestion entails a totally new CPI architecture to be tested for feasibility.

Since the OAFFI(CPI) characteristics were determined in Chapter V, it seems appropriate for the first recommendation to include an examination of this same architecture in a different manner. Note that this thesis was approached strictly from an optical signal processing viewpoint. Therefore, since the OAFFI(CPI) exhibited stability problems in the error signal $e(t)$, a control theoretical analysis should be the next area of research emphasis. The control theoretical approach should include efforts to develop explicit mathematical models with block diagrams and transfer functions. The closed-loop and open-loop systems then should be studied for proper compensation designs for not only stability, but also for desired transient response of the resulting filters.

Regardless of what modification is made to the system; the total processing time of the optics should not be increased or else the benefits of OSP in near real-time will be forfeited.

The second recommendation includes an alternative OAFFI(CPI) architecture which will be named OAFFI(CPIA). The OAFFI(Common Path Interferometer Alternative) of Fig. 43 produces the same mathematical result as OAFFI(CPI). The fundamental difference of OAFFI(CPIA) is that a cross-correlation of the error signal and the input signal will be imaged onto the time-integrating LCLV as opposed to Fourier transforming the input signal onto the LCLV, as was the case in OAFFI(CPI). To understand the full implication of the above architecture, the reader is referred to Appendix C.

Note: Not all essential optical hardware is displayed.

PM = Point Modulator LCLV = Liquid Crystal Light Valve BC2 = Bragg Cell 2
 BC1 = Bragg Cell 1 SL2, SL3 = Imaging Lens Pair SL4 = Fourier Transforming Lens
 SL1 = Imaging Lens PD = Photo-Detector

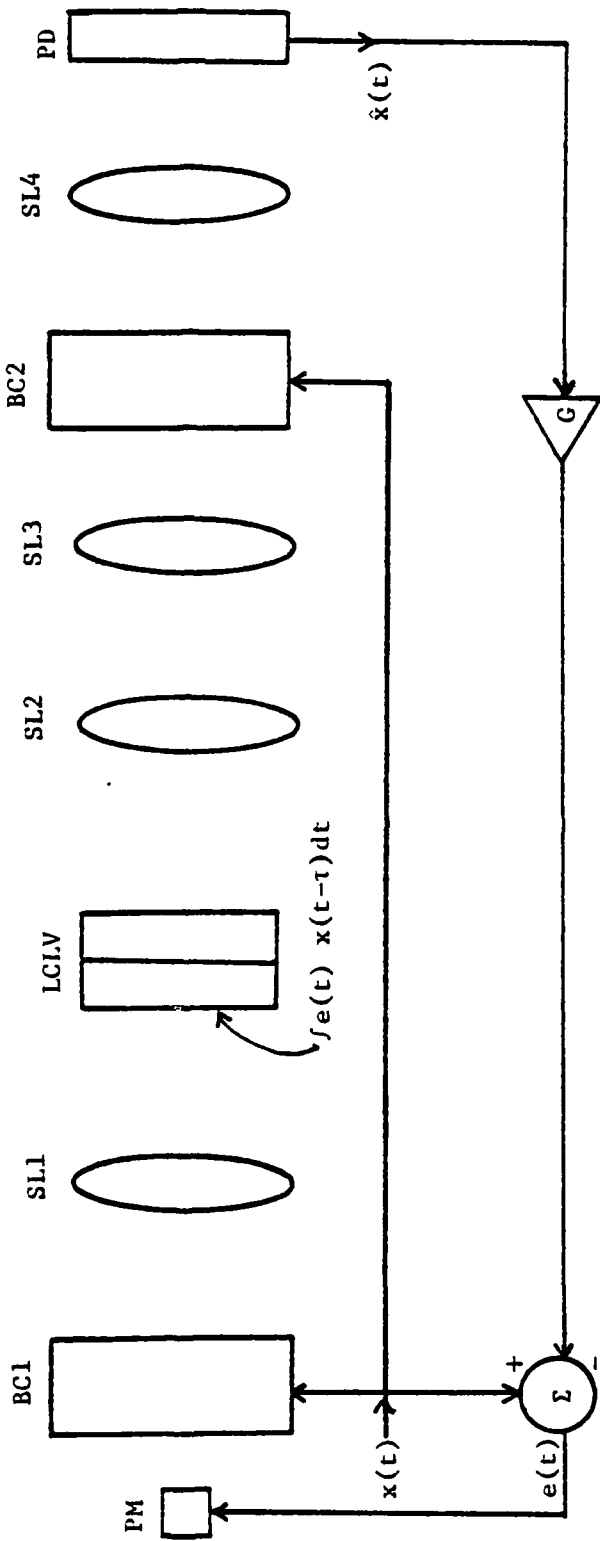


Fig. 43. Conceptual Architecture for OAFFI (CPIA)

Bibliography

1. Anderson, Dean B. "Integrated Optical Spectrum Analyzer: An Imminent 'Chip'," IEEE Spectrum, 22-29 (December, 1978).
2. Bleha, W. P. et. al. "Application of The Liquid Crystal Light Valve to Real-Time Data Processing," Optical Engineering, Vol. 17, No. 4: 371-384, (July - August, 1978).
3. Born, Max and Wolf, Emil. Principles of Optics (Electromagnetic Theory of Propagation, Interference and Diffraction of Light). Elmsford, New York: Pergamon Press, Fifth Edition, 1975.
4. Candler, C. Modern Interferometers. Glasgow, Great Britain: Hilger and Watts LTD., Hilger Division, 1951.
5. Cappellini, V., Constantindes, A. G. and Emiliani, P. Digital Filters And Their Applications. London: Academic Press Inc. LTD. 1978.
6. Cassasent, David. et al. Evaluation of the Hybrid Field-Effect Liquid Crystal as a Coherent Optical Transducer. Huntsville, Alabama: Ballistic Missile Defense Advanced Technology Center, 1 March 1978.
7. Erickson, Jerry L. "Linear acousto-optic filters for programmable and adaptive filtering," SPIE, 341 Real Time Signal Processing V: 173-180 (1982).
8. Gaskill, J. D. Linear Systems, Fourier Transforms and Optics. New York: John Wiley and Sons, 1978.
9. Goodman, J. W. Introduction to Fourier Optics. New York: McGraw-Hill Book Company, 1968.
10. Hamming, Richard W. Digital Filters. Englewood Cliffs, New Jersey: Prentice-Hall, Inc., 1977.
11. Hecht, D. L. "Spectrum Analysis Using Acousto-Optic Devices," SPIE, 90 Acousto-Optics: 148-157 (1976).
12. Kao, K. Optical Fiber Systems: Technology, Design and Applications. New York: McGraw-Hill Book Company, 1982.
13. Korpel, Adrianus. "Acousto-Optics---A Review of Fundamentals," Proc IEEE, 69: 48-53 (January, 1981).

14. Lipson, S. G. and Lipson, H. Optical Physics. New York, New York: Cambridge University Press, 1969.
15. "Liquid Crystal Light Valve for Real Time Optical Processing," Product Information. Carlsbad, California: Hughes Aircraft Company, Industrial Products Division, 26 June 78.
16. McCool, John M. and Widrow, Bernard. "Principles and Applications of Adaptive Filters: A Tutorial Review," Proceedings International Symposium Circuits Systems, 1980, pp. 1143-1157.
17. "Model AOD-70 Acousto-Optic Light Deflector," Instruction Manual. Bellwood, Illinois: IntraAction Corp., 11 October 1976.
18. Morgan, D. R. and Craig, S. E. "Real Time Adaptive Linear Prediction Using The Least Mean Square Gradient Algorithm," IEEE Transactions on Acoustics, Speech, and Signal Processing, ASSP-24, No. 6: 494-507, (December 1976).
19. Oppenheim, Allan V. and Schaffer, Ronald W. Digital Signal Processing. Englewood Cliffs, New Jersey: Prentice-Hall, Inc., 1975.
20. Peebles, Peyton Z. Jr. Communication System Principles, Don Mills, Ontario: Addison-Wesley Publishing Company, 1976.
21. Penn, W. A. et. al. Acousto-Optic Adaptive Processor (AOAP). F30602-81-C-0264. Griffiss AFB, New York: Rome Air Development Center, February 1983.
22. Rhodes, J. R. and Brown, D. E. "Adaptive filtering with correlation cancellation loops," SPIE, 341 Real Time Signal Processing V: 140-147 (1982).
23. Skolnik, Merrill I. Radar Handbook, New York: McGraw-Hill Book Company, 1970.
24. Syed, Vaqar. Adaptive Antenna Arrays," EE 6.73 Class Notes. Wright-Patterson AFB, Ohio: Air Force Institute of Technology, October, 1983.
25. Turpin, Terry M. "Spectrum Analysis Using Optical Processing," Proceedings of the IEEE, Vol 69, No. 1: 79-92, (January 1981).
26. Vander Lugt, A. "Adaptive Optical Processor," Applied Optics, Vol 21, No. 22: 4005-4011 (15 November 1982).
27. Widrow, B. and McCool, J. M. "A Comparison of Adaptive Algorithms Based on the Methods of Steepest Descent and Random Search," IEEE Transactions on Antennas and Propagation, AP-24: 615-637 (September 1976).

28. Yarborough, John. "Communications Applications of Acousto-Optic Bragg Cell Receiver/Processors," (unpublished).
29. Yariv, Amnon. Introduction to Optical Electronics (Second Edition). New York: Holt Rinehart Winston, 1976.
30. Zahn, Markus. Electromagnetic Field Theory: a problem solving approach. New York: John Wiley and Sons, 1979.

Appendix A

IntraAction AOD-70 Bragg Cell

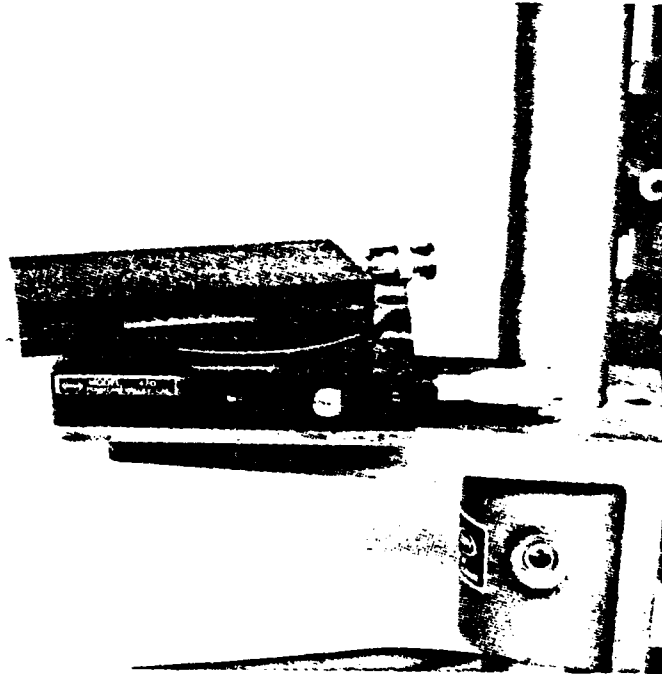


Photo A-1. IntraAction AOD-70 Bragg Cell.

Photo A-1 displays one of the Bragg cells (manufactured by IntraAction Corporation) which was used throughout this thesis. The transducer is on the RHS and the acoustic termination end is on the LHS of Photo A-1. The glass window on the front of the Bragg cell is the optical aperture. The Bragg cell operates at a center frequency of 70 MHZ with a 40 MHZ bandwidth and a maximum input power of 4 watts. Currently, the AOD-70 (Acousto-Optic Light Deflector-Model 70) is selling for about \$1,300.

Most of the general operating principles of the Bragg cell were

covered in the text under Acousto-Optics. In this appendix, some of the Bragg cell's specific characteristics will be defined.

The IntraAction Bragg cell uses high quality flint glass, having an index of refraction $n = 1.92$, as the interaction medium. The acoustic waves are generated by piezoelectric transducers made from Indium bonded Lithium Niobate. It operates in the optical wavelength range of 420 to 700 nanometers and has a design optical wavelength of 633 nanometers.

The number of resolvable spots or light distributions N is identified by the time-bandwidth product. According to the manufacturer (Ref. 17), the AOD-70 Bragg cell can achieve 400 spots of resolution from a 40 MHz bandwidth and a time aperture of 10 μ secs.

The BC2 used in Fig. 32 had a modified or extended aperture. The length of the aperture can be derived from:

$$N = BW \left(\frac{D}{v_s} \right) = BW \gamma$$

where

N = number of resolvable spots

BW = bandwidth of the Bragg cell

D = aperture length

v_s = velocity of sound in the medium

γ = time aperture of the Bragg cell

In OAFFI(CPI), the time aperture $\gamma = 10.94 \mu$ secs. Therefore,

$$\gamma = \frac{D}{v_s} = 10.94 \mu\text{secs.}$$

$$v_s = 3800 \text{ m/sec}$$

$$\begin{aligned} D &= (10.94 \text{ usecs.}) (3800 \text{ m/sec}) \\ &= 41.57 \text{ mm} \end{aligned}$$

So, the modified Bragg cell has an optical aperture of 41.57 mm. Note that this was not verified by directly measuring the aperture.

Diffraction efficiency is a good measure of AO performance. However, acoustic power in the Bragg cell was not measured in this thesis. Therefore, Eq. (35) could not be used to determine the diffraction efficiency achieved by OAFFI(CPI). However, Table A-I shows data obtained from a similar Bragg cell.

The optical quality of Bragg cell BC2 used in OAFFI(CPI) is demonstrated by the interferogram in Photo A-2. Since the interference

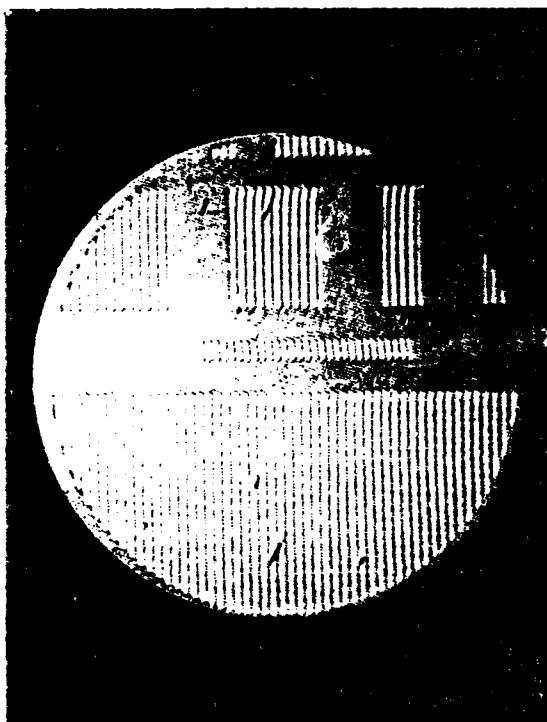


Photo A-2. Interferogram of Bragg Cell BC2 Used in OAFFI(CPI). Note that BC2 is the isolated rectangle in the center of the photo.

Table A-I

Characteristics of a Model AOD-70 Bragg Cell

Item	Value
Input Frequency	70 MHZ
Diffraction Efficiency	84%
Incident RF Power	5.3 Watts
Reflected RF Power	0.9 Watts
Reflection Coefficient (Γ_L)	0.41
VSWR	2.40

AD-A141 090 OPTICAL ADAPTIVE FILTER FREQUENCY DOMAIN IMPLEMENTATION 3/3

(U) AIR FORCE INST OF TECH WRIGHT-PATTERSON AFB OH
SCHOOL OF ENGINEERING J L NEWMAN DEC 83

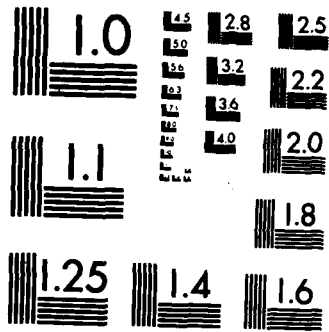
UNCLASSIFIED

AFIT/GE/EE/83D-51

F/G 20/6

NL





MICROCOPY RESOLUTION TEST CHART
NATIONAL BUREAU OF STANDARDS-1963-A

fringes are all parallel, the Bragg cell has complete uniformity and thus, a high optical quality. In a poor optical quality device, the interference fringes would converge sporadically. Further details can be found in Ref. 17.

Appendix B

Hughes Liquid Crystal Light Valve

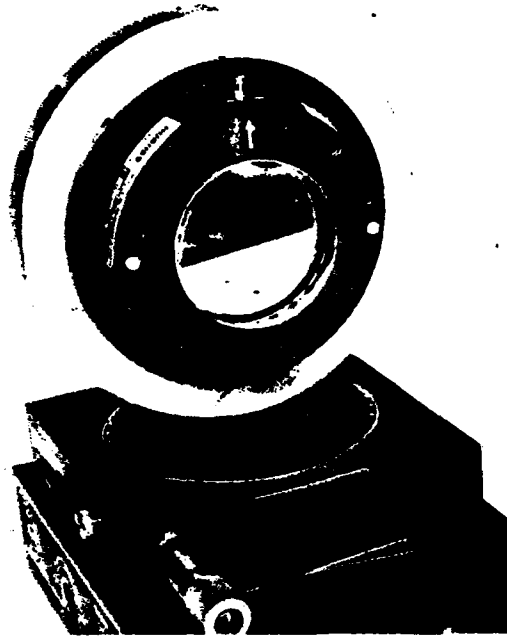


Photo B-1. Hughes Liquid Crystal Light Valve.

Photo B-1 displays the LCLV (manufactured by Hughes Aircraft) which was used throughout this thesis. It requires 13.7 VAC at a frequency of 10KHZ for efficient operation. Currently, the LCLV is selling for about \$25,000.

The LCLV is basically an optical-to-optical image transducer which can receive a low intensity, white or green input light image and convert it, in real time, to an output image with light from another source or the same source. The input and output optical beams are completely separated and noninteracting.

In Fig. B-1, the writing light enters from the RHS and impinges

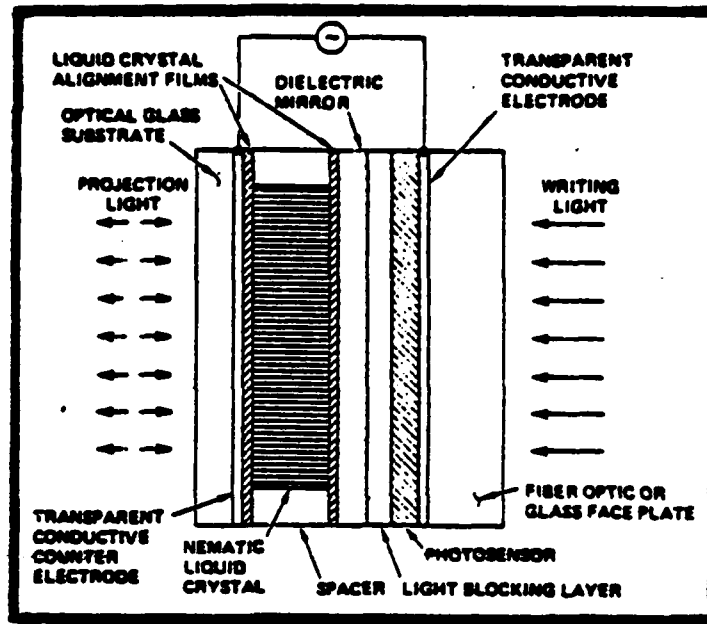


Fig. B-1. Cross-Sectional Schematic of the Liquid Crystal Light Valve (Ref. 2:372)

upon a Cadmium Sulfide (CdS) photoconductive layer. The CdS layer interacts with a biasing A.C. voltage and produces an electric field across the nematic liquid crystal on the LHS of the LCLV (Ref. 21:81-83). This electric field, which appears on the read side, is an image of the written pattern. Thus, the LCLV has two sides: an input or write side and an output or read side.

The LCLV has an inherent polarization rotation angle α which is characteristic of its dark state. When an input intensity impinges upon the write side, the final output intensity has a polarization rotation angle $\alpha + \delta$. Therefore, a polarizer, oriented perpendicular to angle α , is required to obtain only the information from the input intensity.

The electric field, on the read side, causes the polarization of the coherent read beam to be oriented at the angle $\alpha + \delta$. Thus, the read beam is reflected into and out of the liquid crystal layer with the

output being a modulated beam at a polarization angle $\alpha + \delta$, which is proportional to the input intensity on the write side.

This effect is what Hughes calls a "hybrid field effect mode" (Fig. B-2). This mode involves both the twisted nematic effect in the liquid crystal and a birefringent effect. Further details can be found in Ref. 2.

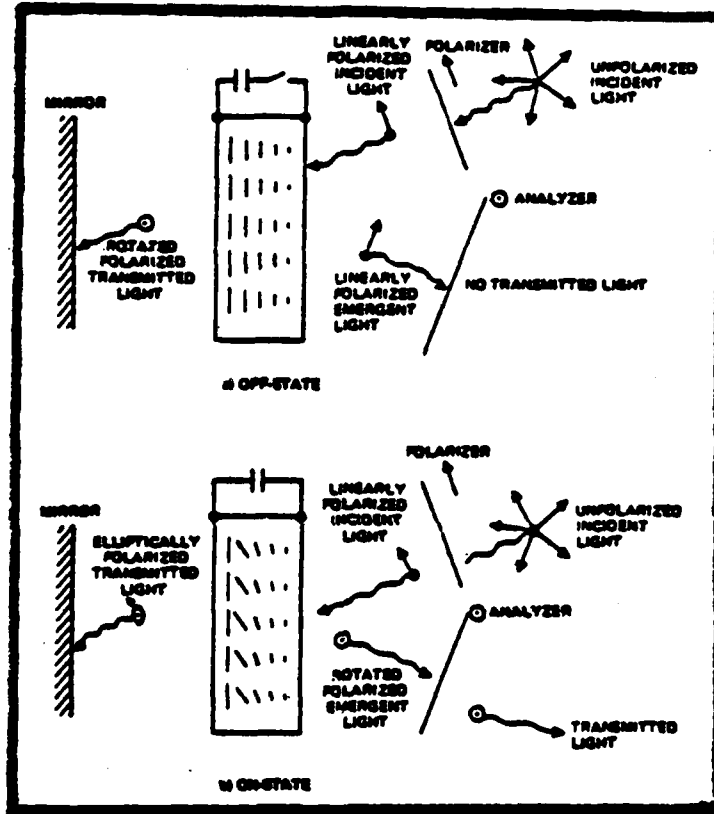


Fig. B-2. Operation of the Hybrid Field Effect Mode Light Valve: (a) the off-state, (b) the on-state (Ref. 2:373)

Appendix C

OAFFI(CPIA) Analysis

This Appendix derives the mathematical basis for the Optical Adaptive Filter: Frequency Domain Implementation (Common Path Interferometer Alternative).

Recall in Eq. (51) of the original OAFFI theory, the desired result for $\hat{x}(t)$ was given by

$$\hat{x}(t) = \int E(\omega) |X(\omega)|^2 e^{j\omega t} d\omega$$

To produce this result, the point modulator of Fig. 43 is driven by the error signal $e(t)$. Bragg cell BC1 is driven by the input signal $x(t)$. Spherical lens SL1 images the product of the error signal and a delayed version of the input signal onto the LCLV, which is a time-integrating optical detector. The following cross-correlation is formed at the LCLV:

$$\int_T e(t) x(t - \tau) dt$$

The output side of the LCLV will display the cross-correlation, in the form of diffracted spatial frequencies, on a DC bias. Both the cross-correlation and the DC bias are imaged onto BC2 via the lens pair SL2 and SL3. Bragg cell BC2 is also driven by $x(t)$. Spherical lens SL4 Fourier transforms both the cross-correlation and the BC2 input signal $x(t)$ for integration by the detector as follows:

$$\int |E(\omega) X^*(\omega) + X^*(\omega) e^{-j\tilde{\omega}t}|^2 d\omega$$

where

$E(\omega) X^*(\omega)$ is the FT of the cross-correlation

$X^*(\omega) e^{-j\tilde{\omega}t}$ is the negative Doppler-shifted first-order light distribution of $x(t)$

As a result of the following derivation, the desired result for $\hat{x}(t)$ is produced.

$$\begin{aligned} & \int |E(\omega) X^*(\omega) + X^*(\omega) e^{-j\tilde{\omega}t}|^2 d\omega \\ &= \int (E(\omega) X^*(\omega) + X^*(\omega) e^{-j\tilde{\omega}t}) (E^*(\omega) X(\omega) - X(\omega) e^{j\tilde{\omega}t}) d\omega \\ &= \int \{E(\omega) X^*(\omega) E^*(\omega) X(\omega) - X^*(\omega) X(\omega) + X^*(\omega) E^*(\omega) X(\omega) e^{-j\tilde{\omega}t} \\ &\quad - E(\omega) X^*(\omega) X(\omega) e^{j\tilde{\omega}t}\} d\omega \\ &= \int \{ |E(\omega)|^2 |X(\omega)|^2 - |X(\omega)|^2 + E^*(\omega) |X(\omega)|^2 e^{-j\tilde{\omega}t} \\ &\quad - E(\omega) |X(\omega)|^2 e^{j\tilde{\omega}t} \} d\omega \end{aligned}$$

where

$|E(\omega)|^2 |X(\omega)|^2$ and $-|X(\omega)|^2$ are biasing terms, which will be dropped for convenience

and

$$E(\omega) |X(\omega)|^2 e^{j\tilde{\omega}t} = (E^*(\omega) |X(\omega)|^2 e^{-j\tilde{\omega}t})^*$$

Thus, the result for $\hat{x}(t)$ is given by:

$$\hat{x}(t) = 2 \int E(\omega) |X(\omega)|^2 e^{j\tilde{\omega}t}$$

This is the same result as produced by OAFFI(CPI).

Moreover, the problem with the time delay τ encountered in OAFFI(CPI) may be avoided since the cross-correlation is performed before the Fourier transformation process. In other words, in OAFFI(CPIA), the inherent time delay due to reconstruction from the frequency plane is not reinjected into BC2 (Fig. 43) to give still more time delay in the subsequent reconstruction, which results in still more time delay, etc., etc. as may be the case in the OAFFI(CPI) of Fig. 32.

Furthermore, any minor time delay in the correlation process can be compensated for by rotating the LCLV, which controls the position of the LCLV image in BC2. Thus, the time delay is governed by the spatial positioning of the incident light distribution in the Bragg cell.

Vita

Jeffrey Lee Newman was born 13 June 1955 in Hanover, Pennsylvania. He graduated from high school in Biglerville, Pennsylvania in 1973. Upon selection for the Airman's Education and Commissioning Program, he attended the University of New Hampshire from which he received the degree of Bachelor of Science in Electrical Engineering in December 1979. He received his commission in the U.S. Air Force through Officer Training School in April 1980. He graduated from the Communications-Electronics Engineer Course at Keesler AFB, Mississippi in October 1980. He served as a Space and Warning Command, Control and Communications Engineer with Headquarters, Strategic Communications Division at Offutt AFB, Nebraska until entering the School of Engineering, Air Force Institute of Technology, in June 1982. Upon graduation from AFIT in December 1983, he is scheduled for assignment to the Computer Systems Network Branch (R620) at the Defense Communications Engineering Center, 1860 Wiehle Avenue, Reston, Virginia 22091.

Permanent Address: Box 188

Arendtsville, PA 17303

REPORT DOCUMENTATION PAGE

1a. REPORT SECURITY CLASSIFICATION UNCLASSIFIED			1b. RESTRICTIVE MARKINGS			
2a. DECLASSIFICATION/DOWNGRADING SCHEDULE			3. DISTRIBUTION/AVAILABILITY OF REPORT Approved for public release; distribution unlimited.			
4. PERFORMING ORGANIZATION REPORT NUMBER(S) AFIT/GE/EE/83D-51			5. MONITORING ORGANIZATION REPORT NUMBER(S)			
6a. NAME OF PERFORMING ORGANIZATION School of Engineering		6b. OFFICE SYMBOL (If applicable) AFIT/ENG		7a. NAME OF MONITORING ORGANIZATION		
6c. ADDRESS (City, State and ZIP Code) Air Force Institute of Technology Wright-Patterson, AFB, Ohio 45433			7b. ADDRESS (City, State and ZIP Code)			
8a. NAME OF FUNDING/SPONSORING ORGANIZATION		8b. OFFICE SYMBOL (If applicable)		9. PROCUREMENT INSTRUMENT IDENTIFICATION NUMBER		
8c. ADDRESS (City, State and ZIP Code)			10. SOURCE OF FUNDING NOS.			
			PROGRAM ELEMENT NO.	PROJECT NO.	TASK NO.	WORK UNIT NO.
11. TITLE (Include Security Classification) See Box 19						
12. PERSONAL AUTHOR(S) Jeffrey L. Newman, B.S.E.E., 1st Lt, USAF						
13a. TYPE OF REPORT MS Thesis		13b. TIME COVERED FROM _____ TO _____		14. DATE OF REPORT (Yr., Mo., Day) 1983 December		15. PAGE COUNT 199
16. SUPPLEMENTARY NOTATION						
17. COSATI CODES			18. SUBJECT TERMS (Continue on reverse if necessary and identify by block number)			
FIELD	GROUP	SUB. GR.				
17	08		Acoustooptics, Adaptive Filters, Bragg Angle,			
20	06		Correlators, Optical Filters, Optical Interferometers, Optical Processing, Optical Correlators			
19. ABSTRACT (Continue on reverse if necessary and identify by block number)						
Title: OPTICAL ADAPTIVE FILTER: FREQUENCY DOMAIN IMPLEMENTATION			Approved for public release: IAW AFB 190-17. <i>[Signature]</i> LYNN E. WOLFAVER Dean for Research and Professional Development, Air Force Institute of Technology (ATC) Wright-Patterson AFB OH 45433			
Thesis Chairman: Dr. Vaqar H. Syed						
20. DISTRIBUTION/AVAILABILITY OF ABSTRACT CLASSIFIED/UNLIMITED <input checked="" type="checkbox"/> SAME AS RPT. <input type="checkbox"/> DTIC USERS <input type="checkbox"/>			21. ABSTRACT SECURITY CLASSIFICATION UNCLASSIFIED			
22a. NAME OF RESPONSIBLE INDIVIDUAL Dr. Vaqar H. Syed			22b. TELEPHONE NUMBER (Include Area Code) 513-255-3576		22c. OFFICE SYMBOL AFIT/ENG	

19.

This report presents the results of a feasibility test on an optical adaptive filter, implemented in the frequency domain. The OAFFI is the follow-on to the optical adaptive filter (OAF), which was implemented in the time domain. The theory of OAFFI is based on adaptive linear prediction using correlation cancellation loops and optical signal processing (OSP) using Fourier optics (lenses) and acousto-optics (Bragg cells).

A few optical architectures, which form the fundamental building blocks of OAFFI, were built and examined prior to the OAFFI architectures. These fundamental architectures included an Optical Spectrum Analyzer, Optical Excisor (two versions) and a Liquid Crystal Light Valve. The Optical Excisor used heterodyning principles which in an OSP sense usually involves an interferometric architecture.

The OAFFI was implemented in two-versions: Mach-Zehnder interferometer (MZI) and common path interferometer (CPI). OAFFI(MZI) exhibited phase stability problems in the optical output. To overcome these phase stability problems, the common path interferometer version of OAFFI was built. OAFFI(CPI) overcame the phase stability problems of OAFFI(MZI). However, stability problems resulting from positive feedback at various frequencies were observed in OAFFI(CPI). Nevertheless, OAFFI(CPI) also demonstrated some positive results that should stimulate further investigations.

END

FILMED